

ABSTRACT

SMITH , FOUCHÉ. A High Order Compact Scheme for Interior/Exterior 3D Wave Equation by the Method of Difference Potentials . (Under the direction of Dr. Semyon Tsynkov).

In this work we develop several high order compact schemes for solving the three dimensional acoustic wave equation with variable speed of sound. We consider when the domain is an open and connected subset with finite measure, all of \mathbb{R}^3 , or the complement of some open and connected subset of finite measure. Each initial boundary value problem (IBVP) will be solved with the method of difference potentials (MDP). The later two problems will be truncated with a finite computational domain with a high order artificial boundary condition imposed on its surface to absorb any outgoing waves.

First, we discretize the wave equation in time using the θ -scheme. This produces a one parameter family of elliptic PDEs on the upper time level whose RHS term is composed of known quantities from the previous two time levels and boundary condition is inherited from the wave equation on the upper time level. The parameter θ is chosen to produce fourth order accuracy in time.

Advancing the time marching scheme amounts to solving an elliptic boundary value problem at every time step via the MDP. The MDP has the ability to use finite difference (FD) schemes while using a spectral representation of the boundary condition to handle the curvilinear geometry of BVP. The MDP embeds the domain of the BVP into a cubic domain auxiliary domain where a FD scheme can flourish. The solution to the elliptic PDE on the original domain is constructed with a difference potential, which is the discrete counterpart to Calderón-Seeley potentials which reduces an elliptic PDE on its domain to an equivalent expression on its boundary. This difference potential is constructed from the solution operator to the discrete elliptic PDE on the cubic auxiliary domain.

The most computationally intensive portion of the scheme involves the solution operator needed to construct the difference potential. So we want to compute it efficiently. We discretize the elliptic PDE on the cubic auxiliary domain with fourth order accuracy in space using a compact finite difference scheme. We use an equation based approach to obtain scheme which only uses 19 points on a $3 \times 3 \times 3$ stencil. The

high order accuracy acts as a hedge against numerical dispersion, the compact stencil produces a sparse linear system, and the elliptic PDE can be solved in $\mathcal{O}(N \log N)$ operations with geometric multigrid.

Keywords: Unsteady acoustic waves, High order accuracy, compact finite difference scheme, Cartesian grid, Non-conforming geometry, Multigrid, High order artificial boundary conditions, unbounded domains, scattering problem, method of difference potentials

© Copyright 2022 by Fouché Smith

All Rights Reserved

A High Order Compact Scheme for Interior/Exterior 3D
Wave Equation by the Method of Difference Potentials

by
Fouché Smith

A dissertation submitted to the Graduate Faculty of
North Carolina State University
in partial fulfillment of the
requirements for the Degree of
Doctor of Philosophy

Applied Mathematics

Raleigh, North Carolina
2022

APPROVED BY:

Dr. Alina Chertock

Dr. Zhilin Li

Dr. Ralph Smith

Dr. Eli Turkel
External Member

Dr. Semyon Tsynkov
Chair of Advisory Committee

BIOGRAPHY

Fouché Smith grew up in Tucson, Arizona. He initially attended the University of Arizona to pursue a Bachelor of Science in Chemical Engineering in the fall of 2007. In his first semester attending the University of Arizona, Dr. William Yslas Velez of the mathematics department convinced Fouché to obtain a Bachelor of Science in Applied Mathematics as well. He completed both degrees in 2011 and 2012 respectively. Following the completion of his bachelors degrees he made is way to Lexington, Kentucky to where he obtained his Master of Arts in Mathematics at the University of Kentucky in the Spring of 2015. Desiring to pursue applied mathematics in numerical partial differential equations, he made his way to Raleigh, North Carolina to obtain his Doctorate in Applied Mathematics at North Carolina State University in the fall of 2022. In his next role he be a Research Geophysicist at CGG, a global technology and HPC leader in earth science, data science, sensing, and monitoring. He will work in the Research and Development team developing new, innovative solutions to problems plaguing the seismic industry.

ACKNOWLEDGEMENTS

Thanks you to Dr. William Yslas Velez for convincing me to double major in applied mathematics, Dr. Peter Perry for taking a risk on me at the University of Kentucky, Dr. Semyon Tsynkov for giving me an opportunity in numerical PDEs and being patient through my struggles, Dr. Eli Turkel for his insight and collaboration, the committee for their service, my family for their love and support, and everybody in Laundry 108 for all the laughs.

TABLE OF CONTENTS

LIST OF TABLES	vi
LIST OF FIGURES	viii
Chapter 1 INTRODUCTION	1
1.1 Motivation and Objectives	1
1.1.1 Interior Problem	3
1.1.2 Radiation of Waves by a Known Source	3
1.1.3 Exterior Scattering Problem	4
1.2 Main Components of the Method	5
1.2.1 Compact Finite Difference Scheme	5
1.2.2 Artificial Boundary Condition (ABC)	7
1.2.3 Sponge Layer	11
1.2.4 Method of Difference Potentials	11
1.2.5 Multigrid Methods	16
1.3 Potential Applications	22
1.3.1 Electrical Impedance Tomography (EIT)	23
1.3.2 Photoacoustic Tomography (PAT)	24
1.3.3 Full Waveform Inversion (FWI)	25
1.3.4 Reverse Time Migration	26
1.3.5 Time Reversal	27
1.3.6 Hybrid Solver for Seismic Wave Motion	28
1.4 Outline of the Thesis	29
1.5 Mathematical Contributions	30
Chapter 2 COMPACT FOURTH ORDER ACCURATE SCHEME	32
2.1 Semi-Discrete Approximation in Time	33
2.2 Discrete Modified Helmholtz Equation	35
2.3 Stability Criteria	43
2.4 Full Time Marching Scheme	46
2.5 Multigrid Convergence Rate	46
2.5.1 Empirically Derived Convergence Rates	48
2.5.2 Local Fourier Analysis	48
2.5.3 Validating Multigrid Convergence Rates	50
2.6 Numerical Simulations	51
Chapter 3 INTERIOR PROBLEM	55
3.1 Semi-Discrete Approximation in Time	55
3.2 Method of Difference Potentials (MDP)	56
3.2.1 Auxiliary Problem (AP)	57

3.2.2	Grid Sets on the Auxiliary Domain	58
3.2.3	Discrete Generalized Calderón-Seely Projection	60
3.2.4	Extension Operator on a Sphere	63
3.2.5	Solving the Interior Problem	72
3.3	Numerical Simulations of the Interior Problem	75
Chapter 4	RADIATION OF WAVES BY A KNOWN SOURCE	80
4.1	Sponge Layer	81
4.1.1	High Order Discretization of the Damped Wave Equation	82
4.1.2	Stability Criteria	84
4.1.3	Damping Profile	87
4.1.4	Numerical Simulations with the Sponge Layer	89
4.2	High Order Non-Reflective Boundary Condition	92
4.2.1	Semi Discrete Approximation in Time	93
4.2.2	Advancing the time marching scheme with MDP	93
4.2.3	Numerical Simulations with NRBC	99
Chapter 5	EXTERIOR SCATTERING PROBLEM	106
5.1	Semi Discrete Approximation in Time	107
5.2	Solution on the upper time level by MDP	108
5.2.1	Extension Operator	109
5.2.2	Inhomogeneous Boundary Equation with Projection	113
5.3	Numerical Tests for the Scattering Problem	116
Chapter 6	CONCLUSIONS	119
	REFERENCES	122
	APPENDICES	132
Appendix A	Generating Test Problems	133
Appendix B	Spherical Harmonics	136
B.1	Properties Spherical Harmonics	136
B.2	Generating the Spherical Harmonics	137
B.3	Fast Spherical Harmonics Transform	138
Appendix C	Initiate Scheme	139

LIST OF TABLES

Table 1.1	Given the cube $D = [x_l, x_r]^3$, we use the following settings for MGCYC.	23
Table 2.1	Comparison of empirically derived convergence factors versus the smoothing factor predicted by LFA and the empirically derived convergence factor using (2.35) as a test problem. We employ $V(\nu_1, \nu_2)$ cycles with a step size of $h = \frac{\pi}{256}$	51
Table 2.2	Grid refinement analysis for the test problem (2.37) when the time step τ is 95% of the maximum CFL shown in (2.32).	53
Table 2.3	Grid refinement analysis for the test problem (2.38) when the time step τ is 95% of the maximum CFL shown in (2.32).	54
Table 2.4	Grid refinement analysis for the test problem (2.39) when the time step τ is 95% of the maximum CFL shown in (2.32).	54
Table 2.5	Grid refinement analysis for the test problem (2.40) when the time step τ is 95% of the maximum CFL shown in (2.32).	54
Table 3.1	Contains the coefficients of the one sided difference schemes backwards in time for several derivatives using a uniform time step τ . Rescale the coefficients of the p^{th} order derivative by a factor of $1/\tau^p$	66
Table 3.2	Grid refinement analysis for the test problem (3.32) where the auxiliary domain $\Omega_0 = [-1.5, 1.5]^3$ and the terminal time $T = 5$. Here the speed is $c(x, y, z) = 1$, the uniform time step τ is 90% of the maximum CFL shown in (2.32), and the order of the spectral representation $L = 20$. See Table 1.1 for the specific settings for our multigrid method.	78
Table 3.3	Grid refinement analysis for the test problem (3.32) where $R = 0.90$ and the auxiliary domain $\Omega_0 = [-1.5, 1.5]^3$. Here the speed is $c(x, y, z) = \frac{1}{2} + \frac{1}{4} \sin \sqrt{x^2 + y^2 + z^2}$. The order of the spectral representation $L = 20$. The uniform time step τ is 90% of the maximum CFL shown in (2.32). See Table 1.1 for the specific settings for our multigrid method.	78
Table 3.4	Grid refinement analysis for the test problem (3.32) where $R = 0.90$ and the auxiliary domain $[-1.5, 1.5]^3$. Here the speed is $c(x, y, z) = e^{(y+z)/10}$. The uniform time step τ is 90% of the maximum CFL shown in (2.32). The order of the spectral representation $L = 20$. The maximum speed was taken on the smallest ball which contains the grid set \mathbb{N}^+ on the coarsest grid used in our simulations. See Table 1.1 for the specific settings for our multigrid method.	78

Table 3.5	Grid refinement analysis for the test problem (3.33) the auxiliary domain $[-2.0, 2.0]^3$, and the order of the spectral representation $L = 20$. Here the speed is $c(x, y, z) = 1$. The uniform time step τ is 98% of the maximum CFL shown in (2.32). See Table 1.1 for the specific settings for our multigrid method.	79
Table 3.6	Grid refinement analysis for the test problem (3.33) where $R = 1.5$, the auxiliary domain $[-2.0, 2.0]^3$, and the order of the spectral representation $L = 20$. Here the speed is $c(x, y, z) = \frac{1}{2} + \frac{1}{4} \sin \sqrt{x^2 + y^2 + z^2}$. The uniform time step τ is 98% of the maximum CFL shown in (2.32). See Table 1.1 for the specific settings for our multigrid method.	79
Table 3.7	Grid refinement analysis for the test problem (3.33) where $R = 1.5$, the auxiliary domain $[-2.0, 2.0]^3$, and the order of the spectral representation $L = 20$. Here the speed is $c(x, y, z) = e^{(y+z)/10}$. The uniform time step τ is 98% of the maximum CFL shown in (2.32). The maximum speed was taken on the smallest ball which contains the grid set \mathbb{N}^+ on the coarsest grid used in our simulations. See Table 1.1 for the specific settings for our multigrid method.	79
Table 4.1	Error of Test Solution 1 (page 90) where $D_{\text{vac}} = [-2, 2]^3$, the sponge thickness $\ell = \frac{19}{2}$, and the terminal time $T = 35$	92
Table 4.2	Error of Test Solution 2 (page 90) where $D_{\text{vac}} = [-2, 2]^3$, the sponge thickness $\ell = \frac{17}{2}$, and the terminal time $t = 35$	92
Table 4.3	Error of Test Solutions 1 – 4 when using NRBC(8). The uniform time step τ is 98% of the maximum CFL shown in (2.32) and the terminal time is $T = 10.0$. The order of the spherical harmonics expansion is $L = 25$. The setting of the multigrid method is summarized in Table 1.1.	105

LIST OF FIGURES

Figure 1.1	Schematic of three common MGCYC. The symbols (\bullet) denote pre-smoothing steps, (\circ) — post-smoothing steps, (\blacksquare) — direct solver, (\searrow) — restriction, and (\nearrow) — prolongation + coarse grid correction.	22
Figure 2.1	The nodes adjacent to the center of the stencil (x_i, y_j, z_k) denoted by (\circ) . The symbols are the side-side nodes (\blacksquare) , side-corner nodes (\bullet) , and corner-corner nodes (\blacklozenge)	37
Figure 2.2	A four coloring of the grid set D_h^0 . The left/right grids indicate when the z-plane is oddly/evenly indexed.	42
Figure 3.1	Subset of the discrete boundary γ when Ω is a ball of radius 1.65 centered at the origin.	59
Figure 3.2	Example of the grid sets γ^-, γ^+ , and γ_{proj} which straddle the continuous boundary Γ . The discrete boundary $\gamma = \gamma_+ \cup \gamma_-$. . .	61
Figure 4.1	Plots of the shape function (4.15) for several values of α	88
Figure 4.2	Plots of the univariate damping profile (4.16) assuming $\bar{x}_l = -5.0$, $\bar{x}_r = 5.0$, $\ell = 5.0$, and $\sigma_{\text{max}} = 1.0$ for several values of α . The interval between the two vertical blue lines represents the vacuum region. The interval between the vertical blue line and vertical red line is the damping region.	89
Figure 4.3	Plots of the error history for Test Solution 1 (page 90) when $D_{\text{vac}} = [-2.0, 2.0]^3$ and the sponge thickness $\ell = 5.0$	91
Figure 4.4	Error History for Test Solution 3 assuming $L = 25$ for several different NRBCs.	104
Figure 5.1	Error history for (5.31) where the computational domain is the spherical shell $\Omega = \{\mathbf{x} \mid 1.0 \leq \ \mathbf{x}\ _2 \leq 1.5\}$, the auxiliary domain $\Omega^0 = [-2.0, 2.0]^3$, the order of the spherical harmonics expansions $L_0 = L_1 = 18$, and the terminal time $T = \frac{15}{2}$. The overall error from the coarsest to the finest grid is 2.865e-01, 4.691e-03, 2.674e-04, and 1.703e-05.	118

Chapter 1

INTRODUCTION

1.1 Motivation and Objectives

The acoustic wave equation presents a simplified yet relevant model for a broad variety of problems in electrodynamics, acoustics, solid mechanics, fluid mechanics, geophysics, oceanography, meteorology, and other areas. We are interested in solving both interior and exterior initial boundary value problems (IBVP) for the 3D inhomogeneous variable speed acoustic wave equation:

$$\frac{\partial^2 u}{\partial t^2} - c^2(\mathbf{x})\Delta u = F(\mathbf{x}, t). \quad (1.1)$$

We will solve equation (1.1) with fourth order accuracy in space and time by means of a compact implicit finite difference scheme that employs only three consecutive time levels (Section 1.2.1). Advancing one time step of this scheme requires solving an elliptic partial differential equation (EPDE) on the upper time level. This is done by multigrid iterations, which converge rapidly (Section 1.2.5). In fact, multigrid is the only solver comparable in complexity to the fast Fourier transform (FFT) but not limited to constant coefficients.

An important advantage of compact schemes is that they employ narrow stencils and thus require no additional boundary (or initial) conditions beyond those needed for the differential equation that they approximate. The scheme that we are using is constructed on a uniform Cartesian grid in space. Hence, it offers a most straightforward and economical venue toward high order accuracy, which is of central importance for reducing the numerical pollution. However, it requires a special

treatment for non-conforming (curvilinear) boundaries.

The non-conforming boundaries will be handled using the method of difference potentials (MDP, Section 1.2.4). This method can be thought of as a discrete counterpart to the method of Calderon's operators for PDEs. It has the capacity of treating the general shape boundaries on regular structured grids with no deterioration of accuracy and no adverse implications for either well-posedness or stability. The original development of the MDP targeted the steady-state and time-harmonic problems. To use this method for time-dependent problems, such as those based on equation (1.1), one can adopt one of the two approaches. The first approach is to apply the MDP directly to the time-dependent formulation in (3+1)D space-time. It has proven very efficient, especially when combined with the (strong) Huygens' principle. In particular, it offers a sub-linear complexity and automatically accounts for the radiation of waves toward infinity. However, it cannot be adapted easily to the scenarios that involve the variable speed of wave propagation.

The second approach is to apply the MDP to the EPDE on the upper time level of an implicit discretization scheme in 3D (as opposed to (3+1)D). This strategy lacks certain benefits that come with the one that employs the Huygens' principle. For example, one needs an artificial boundary condition (ABC, Section 1.2.2) or an absorbing layer (Section 1.2.3) to enable the reflectionless propagation of outgoing waves through the outer boundary. However, this approach can easily account for the variation of c : $c = c(\mathbf{x})$, see equation (1.1), which is a major advantage.

Therefore, our overall objective is to develop and implement a methodology for computing the solutions to equation (1.1) that would combine an implicit compact high order accurate scheme with the MDP on the upper time level and allow one to solve several different types of unsteady IBVPs with variable speed of propagation and non-conforming geometry, as indicated in Sections 1.1.1, 1.1.2, and 1.1.3.

1.1.1 Interior Problem

Let $\Omega \subset \mathbb{R}^3$ be a bounded simply-connected domain. Consider the following interior IBVP:

$$\begin{aligned} \frac{\partial^2 u}{\partial t^2} - c^2(\mathbf{x})\Delta u &= F(\mathbf{x}, t), \quad (\mathbf{x}, t) \in \Omega \times (0, T], \\ u(\mathbf{x}, 0) &= \varphi_0(\mathbf{x}), \quad \mathbf{x} \in \Omega, \\ \frac{\partial u}{\partial t}(\mathbf{x}, 0) &= \varphi_1(\mathbf{x}), \quad \mathbf{x} \in \Omega, \\ \mathfrak{l}_\Gamma(u) &= \varphi_\Gamma(\mathbf{x}, t), \quad \mathbf{x} \in \Gamma = \partial\Omega, \end{aligned} \tag{1.2}$$

where the operator \mathfrak{l}_Γ that defines the boundary condition is given by

$$\mathfrak{l}_\Gamma(u) = \left(au + b \frac{\partial u}{\partial \mathbf{n}} \right) \Big|_\Gamma, \tag{1.3}$$

and may correspond to a Dirichlet ($(a, b) = (1, 0)$), Neumann ($(a, b) = (0, 1)$), or Robin ($(a, b) \neq (0, 0)$) boundary condition. The interior problem (1.2) is discussed in Chapter 3. Specifically, in Section 3.1 we show the semi-discrete approximation in time of the interior problem (1.2). This results in a one parameter family of elliptic PDEs which needs to be solved at every time step. In Section 3.2, we detail how the method of difference potentials as applied to the elliptic PDE mentioned above. In Section 3.3, we present the solution to several test problems where Ω is a ball and demonstrate that the scheme is fourth order accurate.

1.1.2 Radiation of Waves by a Known Source

Consider

$$\begin{aligned} \frac{\partial^2 u}{\partial t^2} - c^2(\mathbf{x})\Delta u &= F(\mathbf{x}, t), \quad (\mathbf{x}, t) \in \mathbb{R}^3 \times (0, T], \\ u(\mathbf{x}, 0) &= 0, \quad \mathbf{x} \in \mathbb{R}^3, \\ \frac{\partial u}{\partial t}(\mathbf{x}, 0) &= 0, \quad \mathbf{x} \in \mathbb{R}^3, \end{aligned} \tag{1.4}$$

where the source term F is compactly supported in space. In addition, assume that the propagation speed c is constant on the complement of some ball. To truncate the

wave radiation problem (1.4), we can use either a high order artificial (non-reflecting) boundary condition (Section 1.2.2) or a sponge layer (Section 1.2.3). The sponge layer truncates the domain to a rectangular prism and adds an additional damping term to the wave equation. This damping term is positive inside the sponge layer to attenuate any waves which enter the sponge layer and is zero otherwise to coincide with the wave equation. A high order non-reflecting boundary condition (NRBC) truncates the problem to a ball. On the spherical outer boundary Γ , we impose a p^{th} order artificial boundary condition to absorb the outgoing waves. To represent the trace of the solution $\boldsymbol{\xi}_\Gamma = (u, \frac{\partial u}{\partial r})|_\Gamma$, we use the spherical harmonics, which allows us to greatly simplify the tangential derivatives contained in the ABC.

Solution of the wave radiation problem (1.4) is presented in Chapter 4. Section 4.1 discusses the methodology with the sponge layer, while Section 4.2 introduces the version with the high order NRBC. Both Section 4.1 and Section 4.2 contain the results of the corresponding numerical simulations.

1.1.3 Exterior Scattering Problem

Let $\Omega \subset \mathbb{R}^3$ be a bounded simply-connected domain. Consider the following exterior IBVP:

$$\begin{aligned} \frac{\partial^2 u}{\partial t^2} - c^2(\mathbf{x})\Delta u &= 0, & \mathbf{x} \in \mathbb{R}^3 \setminus \Omega \times (0, T], \\ u(\mathbf{x}, 0) &= \varphi_0(\mathbf{x}), & \mathbf{x} \in \mathbb{R}^3 \setminus \Omega, \\ \frac{\partial u}{\partial t}(\mathbf{x}, 0) &= \varphi_1(\mathbf{x}), & \mathbf{x} \in \mathbb{R}^3 \setminus \Omega, \\ \mathbf{l}_\Gamma(u) &= \varphi_\Gamma(\mathbf{x}, t), & \mathbf{x} \in \Gamma = \partial\Omega, \end{aligned} \tag{1.5}$$

where the operator \mathbf{l}_Γ that defines the boundary condition is given by

$$\mathbf{l}_\Gamma(u) = \left(au + b \frac{\partial u}{\partial \mathbf{n}} \right) \Big|_\Gamma,$$

and may correspond to a Dirichlet $((a, b) = (1, 0))$, Neumann $((a, b) = (0, 1))$, or Robin $(a, b) \neq (0, 0)$ boundary condition. We will assume that the initial data and source term are compactly supported on $\mathbb{R}^3 \setminus \Omega$. In addition, we assume that there exists a bounded region $Y \supseteq \bar{\Omega}$ such that $c(\mathbf{x}) = c_\infty$ whenever $\mathbf{x} \notin Y$.

Numerical solution of the scattering problem (1.5) is described in Chapter 5. We truncate the exterior problem (1.5) using a spherical artificial outer boundary. The sphere is chosen sufficiently large to fully enclose Y , so that the propagation speed beyond the outer boundary can be considered constant. The computational domain thus becomes a spherical shell. At the outer boundary, we set a high order artificial boundary condition (Section 1.2.2). The inner boundary of the spherical shell coincides with the surface of the scatterer Ω . Section 4.2.1 describes the semi-discrete approximation of the truncated problem in time. This process produces an elliptic PDE on the upper time level which needs to be solved in order to advance the time marching scheme. Section 5.2 describes how to solve the aforementioned elliptic PDE on the spherical shell using the method of difference potentials. Finally, Section 5.3 shows numerical simulations of the scattering problem (1.5).

1.2 Main Components of the Method

1.2.1 Compact Finite Difference Scheme

A compact finite difference scheme achieves high order accuracy while utilizing the minimum width stencil. A number of approaches to building such schemes have been proposed in the literature, including those based on the Padé approximation and Hermite polynomials [1, 27, 64]. Examples of compact schemes applied in practice include those for the Poisson equation [55, 76, 104], Maxwell's equations [59, 94, 110, 117], Navier-Stokes equations [33, 34, 66, 77, 112], and Schrödinger equation [30, 35, 41, 69].

Our goal is to approximate the problems described in Sections 1.1.1, 1.1.2, and 1.1.3 with high order accuracy so as to reduce the adverse effect of numerical dispersion, known as the pollution effect [8]. To discretize the acoustic wave equation (1.1), we first apply the θ -scheme in time [23, 68]. This produces a discretization on three consecutive time levels. On the upper time level, the θ -scheme yields a one parameter family of elliptic partial differential equations (modified Helmholtz equations):

$$\Delta u - \kappa^2 u = f, \tag{1.6}$$

where $\kappa = \kappa(\theta)$ and the RHS f is composed of known quantities on the middle and

lower time levels. The parameter θ is chosen so as to guarantee fourth order accuracy in time. Time marching with the θ -scheme amounts to solving the modified Helmholtz equation (1.6) at every time step where the RHS term depends on the previous two time levels.

To solve the modified Helmholtz equation (1.6) on each time level, we discretize it in space using an equation based fourth order compact scheme (EBFOCS) on a uniform in all directions Cartesian grid. Equation based compact schemes have previously been developed for the original Helmholtz equation [16, 40, 102]. Their advantages include no need for additional boundary conditions beyond those required for the underlying PDE itself and narrow-band matrices of the resulting linear systems. An equation based fourth order compact scheme for equation (1.6) is derived in the following manner:

- ◇ Discretize (1.6) with second order accuracy using central differences.
- ◇ Identify the leading terms of the error expansion using Taylor's formula.
- ◇ Differentiate equation (1.6) to replace the fourth order unmixed derivatives in the leading terms of the error with mixed partial derivatives of maximum order two with respect to any one variable.
- ◇ Approximate the mixed derivatives using their respective central difference formulae. Since the leading error term is $O(h^2)$, the resulting scheme will be fourth order accurate overall.

The development of the scheme and its numerical verification are discussed in Chapter 2. In Section 2.1, we show how to approximate equation (1.1) in time using the θ -scheme [23, 68]. In Section 2.2, we show how to discretize the resulting modified Helmholtz equation (1.6) on the upper time level in space using an equation based fourth order compact scheme that employs a $3 \times 3 \times 3$ stencil. In Section 2.3, we show how to compute the CFL number using the energy based argument due to [18]. In Section 2.4 we describe the full time marching. This includes how to initialize the scheme and produce a high order initial guess for the multigrid solver on the upper time level. In Section 2.5, we argue that the multigrid iterations converge with optimal rate. Finally, in Section 2.6 we implement and test the resulting fourth order accurate compact scheme by solving a simple interior problem with a homogeneous Dirichlet

boundary condition:

$$\begin{aligned}
\frac{\partial^2 u}{\partial t^2} - c^2(\mathbf{x})\Delta u &= F(\mathbf{x}, t), \quad (\mathbf{x}, t) \in D \times (0, \infty), \\
u(\mathbf{x}, 0) &= \varphi_0(\mathbf{x}), \quad \mathbf{x} \in D, \\
\frac{\partial u}{\partial t}(\mathbf{x}, 0) &= \varphi_1(\mathbf{x}), \quad \mathbf{x} \in D, \\
u &= 0, \quad \mathbf{x} \in \partial D,
\end{aligned} \tag{1.7}$$

where D is a Cartesian cube in \mathbb{R}^3 . Besides providing a framework for testing the scheme, the Dirichlet problem (1.7) serves another important role. It leads to a zero Dirichlet boundary value problem (BVP) for the elliptic equation (1.6) on the upper time level. This elliptic BVP provides a key building block for the method of difference potentials, known as the auxiliary problem, see Section 1.2.4 (and also Section 3.2).

1.2.2 Artificial Boundary Condition (ABC)

Both the radiation problem of Section 1.1.2 and scattering problem of Section 1.1.3 are formulated on unbounded domains. To solve these problems numerically, we need to truncate the original unbounded region and introduce a finite computational domain Ω bounded with a smooth surface S which encloses the support of the initial data and source term of the given exterior problem. On the surface S , we will impose an ABC that should account for the proper behavior of the solution outside S .

Work [45] summarizes why designing ABCs is difficult in practice. On the continuous level, the truncated problem on Ω with the ABC imposed on S should be well-posed and the spurious reflections generated by the ABC should be small. On the discrete level, the ABC should be numerically stable and (easily) compatible with the interior solver on Ω . These are the minimum requirements of an ABC. Other desirable properties include:

- ◇ Preserving the sparsity pattern of linear systems.
- ◇ Not adding substantial cost to that of the interior solver on Ω .
- ◇ Accommodating a broad range of geometries, angles of incidence, and types of waves (high/low frequency, propagating/evanescent, etc.)

- ◇ Allowing for approximation with high order accuracy.
- ◇ Allowing for parallel implementation.

The survey paper [43] outlines the trade-offs between exact ABCs and approximate ABCs. An exact ABC (on the continuous level) produces a solution, for all $t > 0$, which coincides with the solution to the original exterior problem restricted to Ω . An approximate ABC is often derived in an ad-hoc manner taking into account the underlying physics in the exterior domain $\mathbb{R}^3 \setminus \Omega$. One way to construct an ABC is to consider the far-field behavior of the solution, i.e., the behavior as $\|\mathbf{x}\| \rightarrow \infty$. An approximate ABC can also be derived by approximating an exact ABC on the surface S that is too complicated to be used in practice. Generally speaking, exact ABCs are more robust than approximate ABC. However, exact ABC are typically limited to simple surfaces due to being derived with integral transforms or separation of variables along the boundary. Achieving accurate results with an exact ABC is simple once the implementation is available. One only needs to refine the grid because the only source of error is the discretization. Approximate ABCs depend on the diameter of the computational domain. For example, when using a far-field condition as an approximate ABC, increasing $\text{diam}(\Omega)$ improves its accuracy. However, as the diameter of Ω increases, the interior solver becomes more expensive. Since we wish to solve a three dimensional PDE in space, we want to avoid this route entirely. Instead we will fix the domain Ω and increase the accuracy of the ABC, i.e., its order, which is the number of leading terms in the far-field expansion of the solution that the boundary condition cancels. Increasing the order of the ABC helps decrease the spurious reflections from the artificial outer boundary. Yet higher order ABCs are more difficult to implement than lower order ABCs.

The survey paper [101] provides an extensive overview of the methods for constructing the ABCs. It outlines the trade-offs between nonlocal ABCs where all the nodes on the surface are coupled, and local ABCs where nodes on the surface are only coupled to adjacent nodes. Exact ABCs are typically nonlocal. Generally speaking, nonlocal ABCs are more robust and accurate but also are more computationally expensive and sometimes limited to simple geometry. Local ABCs are easy to implement, numerically cheap, and geometrically universal, but not nearly as accurate. It is also shown in [101] that, for steady-state problems one can use the DPM to set global highly accurate ABCs on an artificial boundary of an arbitrary shape. This reduces the size

of the computational domain and speeds up the convergence of multigrid iterations, which helps offset the additional cost associated with nonlocal ABCs. However, the governing PDEs outside the computational domain must be homogeneous, which is, in fact, a universal requirement for most ABCs.

For the modified Helmholtz equation (1.6), this requirement won't hold though, because the RHS f depends on the solution at the previous time levels. This will be the case even if the original wave equation (1.1) is homogeneous outside the computational domain, i.e., if the physical source term F is zero there. Therefore, the ABC for the wave equation (1.1) is more convenient to formulate in the full time-dependent framework rather than using the elliptic equation (1.6).

In the time dependent case, an exact ABC is normally expected to be nonlocal in both time and space. Nonlocality in time would require the entire time history of the scheme, which clearly becomes demanding on memory for long-time runs, especially for a three-dimensional problem. The required temporal history of the solution can be restricted to a finite and non-increasing level with the help of the Huygens' principle [81, 79]. In this work, however, our intention is to build a numerical methodology that would be fully local in time (up to the extent of the finite difference stencil). Therefore, for our subsequent development we chose to use local non-reflecting boundary conditions for the wave equation (1.1).

According to [44], the two important requirements for high order NRBC are:

- ◇ The accuracy of the NRBC must increase its order increases.
- ◇ The NRBC needs to be *practically* implementable for an arbitrarily high order.

Ideally, one should be able to adjust the order of the NRBC to meet the specific accuracy needs. If, for example, a p^{th} order NRBC provides insufficient absorption of outgoing waves, it should be possible to increase the order to overcome this deficiency. Likewise, by increasing the order of the ABC one should be able to compute the solution on a smaller domain. However, the practical implementation of local high order ABCs may encounter difficulties. To illustrate that, consider the family of NRBCs due to Bayliss and Turkel [10]:

$$B_p u = \left[\prod_{j=1}^p \left(\frac{1}{c} \frac{\partial}{\partial t} + \frac{\partial}{\partial r} + \frac{2j-1}{R} \right) \right] u = 0, \quad (1.8)$$

where the outer boundary S is a sphere of a given radius R . We will refer to (1.8) as the Baylis-Turkel ABC of order p (BT p) which are derived by writing the far-field expansion of a solution to the wave equation, then producing a family of differential operators which annihilate more terms of the expansion as the order of the ABC increases. In other words, BT p applied to the far field expansion yields the residual $B_p u|_{r=R} = \mathcal{O}(\frac{1}{R^{2p+1}})$. For a fixed value of R , $\limsup_{p \rightarrow \infty} B_p u|_{r=R} = 0$. Ideally, we would like to choose p sufficiently large for a fixed R so that the residual is much smaller than the discretization error from approximating the interior of the computational domain. We see, however, that as the order p increases, the boundary operator B_p in (1.8) contains both radial and temporal derivatives of increasingly high order. This is what makes the practical implementation of the BT p ABCs difficult for orders $p > 2$.

The Higdon NRBC (on the planar artificial boundary $x = a$)

$$B_p u = \left[\prod_{j=1}^p \left(\cos(\theta_j) \frac{\partial}{\partial t} + c \frac{\partial}{\partial x} \right) \right] u|_{x=a} = 0, \quad (1.9)$$

suffers from a similar problem. The Higdon NRBC (1.9) is designed to annihilate all plane waves that propagate with the given angles of incidence $\pm\theta_1, \dots, \pm\theta_p$ to the planar boundary. Similar to (1.8), the Higdon NRBC (1.9) produces high order time derivatives and high order normal derivatives on the hyperplane $x = a$ as its order p increases. Those derivatives are difficult to implement for large values of p .

Hagstrom and Hariharin [49] introduced a family of NRBCs which completely avoid the high order derivatives in time and space by incorporating several auxiliary variables. These boundary conditions are defined as follows:

$$\left(\frac{1}{c} \frac{\partial}{\partial t} + \frac{\partial}{\partial r} + \frac{1}{R} \right) u = v_1, \quad (1.10a)$$

$$\left(\frac{1}{c} \frac{\partial}{\partial t} + \frac{j}{R} \right) v_j = \frac{1}{4R^2} \left(j(j-1) + \Delta_{\theta, \varphi} \right) v_{j-1} + v_{j+1}, \quad (1.10b)$$

where $j = 1, 2, \dots, p$, $v_0 = 2u$, and $v_{p+1} = 0$. One can show that (1.10a)–(1.10b) are equivalent to the Bayliss-Turkel ABC of order $p + 1$. The implementation of (1.10a)–(1.10b) does not encounter the same difficulties as (1.8) or (1.9). Assuming that the artificial outer boundary S , which is a sphere of radius R , is sufficiently far away from the sources and initial data, the finite speed of propagation guarantees that

the auxiliary variables will be identically zero when initializing the scheme. The time derivatives can be handled with an implicit multistep method which is at least fourth order accurate. The tangential derivatives can be handled using a spectral representation of the auxiliary variables and the trace $(u|_{r=R}, \frac{\partial u}{\partial r}|_{r=R})$ on the sphere S via spherical harmonics. Since the spherical harmonics are eigenfunctions of the Laplace-Beltrami operator $\Delta_{\theta, \varphi}$, the tangential derivatives are converted to algebraic expressions. (See Appendix B for more detail on spherical harmonics.) As an added benefit, the spectral form of NRBCs will make it easy to incorporate the boundary conditions with the MDP (see Section 4.2.2 for details). This NRBC is further developed in [56].

1.2.3 Sponge Layer

The sponge layer is an alternative to ABCs for damping the outgoing waves. The earliest sponge layer was developed in [22] directly at the discrete level. It could significantly damp the outgoing waves regardless of the angle they penetrate the layer. Our development of a sponge layer has roots in work [97] that we generalize [58]. We add the first order time derivative to the wave equation (1.1), which introduces damping into the model:

$$\frac{\partial^2 u}{\partial t^2} + \sigma(x, y, z) \frac{\partial u}{\partial t} = c^2(x) \Delta u + F(x, t). \quad (1.11)$$

Equation (1.11) is considered on a cubic computational domain $D = [-(M + \ell), M + \ell]^3$ in \mathbb{R}^3 . In doing so, the central part $[-M, M]^3$ represents the vacuum region where the true physical phenomena take place, while the rest, $D \setminus [-M, M]^3$, is the damping layer of thickness ℓ . The damping term σ , see equation (1.11), is positive in the layer to attenuate the waves and zero on $[-M, M]^3$. In Section 4.1, we present the development of a compact fourth order accurate finite difference scheme for the dissipative wave equation (1.11) discuss the application of the sponge layer for the truncation of the wave radiation problem.

1.2.4 Method of Difference Potentials

The key strength of finite difference methods (FD) is that they provide inexpensive and efficient algorithms for computing the smooth solutions to differential equations

on regular domains/grids. Their primary disadvantage is in dealing with more complicated geometries and solutions with low regularity. The issue of geometry is partially alleviated by the immersed boundary [78] and related methods [65, 113, 67, 115]. In our work, we shall employ the method of difference potentials by Ryaben'kii [88] to handle the non-conforming curvilinear geometries while still using uniformly spaced Cartesian grids.

Prior to describing the MDP [88], let us briefly review other existing methods. The finite element method (FEM) [98, 28, 13] and its extensions (see, e.g., [36, 37]), as well as the discontinuous Galerkin (DG) methods [51], are well established and powerful. Their strength is in dealing with complex geometries and low regularity of the solutions.

In practical problems of wave propagation, especially in 3D, both FD and FEM have serious limitations because of their relatively high “points-per-wavelength” requirement, as well as numerical pollution, see [9, 8] and [57, Section 4.6.1]. The numerical phase velocity of the wave in these methods depends on the wavenumber k , so a propagating packet of waves with different frequencies gets distorted in the simulation. Furthermore, the numerical error depends very strongly on k , particularly via the stability constant [57].

This drawback can be (partially) overcome by high order accurate schemes. They do not introduce additional unknowns per grid node and thus remain inexpensive. Moreover, compact schemes, such as those outlined in Section 1.2.1, reduce pollution while keeping the treatment of the boundary conditions simple. However, geometry still remains a hurdle. In FEM, on the other hand, a high order approximation can be built for arbitrary boundaries, but only in fairly sophisticated and costly algorithms with isoparametric elements. In DG, discontinuous enrichment methods, and GFEM, high order accuracy also requires additional degrees of freedom.

In traditional boundary integral methods (BEM), linear boundary value problems are reduced to integral equations with respect to equivalent boundary sources. These methods impose no limitations on the shape of the boundary and automatically account for the correct far-field behavior of the solution. However, the matrices that appear in the context of BEM are full, as opposed to the sparse FD/FEM matrices. Significant progress in fast multipole methods (FMM) [47, 26, 70, 111, 39] has helped alleviate this issue. The treatment of the boundary conditions in BEM requires care in the choice of the boundary sources. For example, to maintain well-posedness of the

boundary representation, i.e., to obtain a Fredholm integral equation of the second kind, a double layer potential should be used for the Dirichlet boundary condition, and a single layer potential should be used for the Neumann boundary condition. The evaluation of singular integrals presents problems in practice, especially in the vicinity of the boundary. The most serious shortcoming of BEM though is that these methods require explicit knowledge of the fundamental solution and hence are limited to constant coefficients, i.e., to homogeneous media.

Our goal is to construct a high order accurate method that offers geometric flexibility equivalent to that of BEM, yet is not limited to constant coefficients and does not involve any singular integrals. We also wish to avoid the extensive redundancy inherent in high order FEM and discontinuous enrichment methods (e.g., additional unknowns such as Lagrange multipliers enforcing weak continuity). In the regions of smoothness, it is therefore natural to approximate the solution using high order finite differences on regular grids, see Section 1.2.1. To accommodate general boundaries not aligned with the grid, we use the MDP [87, 88], see also [71, 15, 72] for subsequent developments. This very general approach can be viewed as a discrete analog of Calderon's potentials and Calderon's boundary equations with projections [20, 93].

The method of difference potentials provides the same geometric flexibility as BEM does, yet involves no singular kernels and handles variable coefficients. The computational procedure changes drastically compared to BEM. The differential problem is first discretized and then converted to a boundary problem. Finally, the resulting boundary equations are solved as a system. The key advantages of the MDP are as follows:

- ◇ Maximum generality of handling the boundary conditions. The entire class of functions satisfying the underlying differential equation is characterized by an equivalent boundary equation (Calderon's boundary equation with projection). Only later are specific boundary conditions imposed. Any type of boundary conditions can be handled with equal ease, see [15], including mixed, nonlocal, discontinuous, etc.
- ◇ The problem can be discretized on a regular structured grid, yet the boundary can have an arbitrary shape and need not necessarily conform to the grid. This causes no loss of accuracy and there are no adverse effects due to staircasing [21, 53].

- ◇ Boundary representations inherit the accuracy of the core discretization. Hence, high order approximations for problems with non-conforming boundaries can be easily obtained.
- ◇ Variable coefficients of the governing equation(s), or equivalently, heterogeneous media, can be handled as easily as constant coefficients. Constructs of Calderon's operators stay unchanged, except that convolutions with the fundamental solution, which essentially represent application of the inverse operator, are replaced by alternative inverse operators.
- ◇ The methodology does not require numerical approximation of singular integrals. For both constant and variable coefficients, inverse operators can be used that do not involve singularities and allow fast numerical computation.
- ◇ Well-posedness of the boundary formulation is guaranteed automatically.

Consider a time-independent second order linear PDE $Lu = f$ on the domain Ω with the boundary $\Gamma = \partial\Omega$. In our subsequent analysis, L will be the modified Helmholtz operator specified on the left-hand side of (1.6). We will reduce $Lu = f$ to an equivalent operator equation on the boundary Γ only. To do so, consider a larger region $\Omega_0 \supset \Omega$ and assume that for any g there is a unique solution of $Lv = g$ on Ω_0 that satisfies a given boundary condition at $\partial\Omega_0$. Denote the resulting inverse operator for L by G so that $v = Gg$.

A generalized potential of Calderon's type [87, 88] with vector density $\boldsymbol{\zeta}_\Gamma = (\xi_0, \xi_1)|_\Gamma$ is defined as follows. For a given $\boldsymbol{\zeta}_\Gamma$, take an arbitrary smooth function $w(x)$ that satisfies $\mathbf{Tr}w = \boldsymbol{\zeta}_\Gamma$, where $\mathbf{Tr}w \stackrel{\text{def}}{=} \left(w, \frac{\partial w}{\partial n} \right)|_\Gamma$. Let $g = \begin{cases} Lw, & x \in \Omega, \\ 0, & x \notin \Omega. \end{cases}$. Then, the potential is given by

$$P_\Omega \boldsymbol{\zeta}_\Gamma = w - Gg \equiv w - G \left(Lw|_\Omega \right), \quad x \in \Omega. \quad (1.12)$$

The Calderon projection P_Γ is the trace on Γ of the potential P_Ω of (1.12):

$$P_\Gamma \boldsymbol{\zeta}_\Gamma = \mathbf{Tr} P_\Omega \boldsymbol{\zeta}_\Gamma. \quad (1.13)$$

One can show that $P_\Gamma^2 = P_\Gamma$. The key property of the operator P_Γ of (1.13) is the following [87, 88]. *Those and only those $\boldsymbol{\zeta}_\Gamma$ that satisfy the boundary equation with projection*

(BEP):

$$P_\Gamma \xi_\Gamma + \text{Tr} G f = \xi_\Gamma, \quad (1.14)$$

are traces of the solution u to the equation $Lu = f$ on Ω : $\xi_\Gamma = \text{Tr} u$. If, in particular, the original equation is homogeneous, $Lu = 0$ on Ω , then a given density ξ_Γ belongs to the range of the projection, $\xi_\Gamma \in \text{Im} P_\Gamma$, iff it is the trace of a solution u to $Lu = 0$.

The problem of solving equation $Lv = g$ on Ω_0 subject to the chosen boundary condition at $\partial\Omega_0$ is referred to as the *auxiliary problem* (AP). In our implementation, the AP will be formulated on the cubic domain of the Dirichlet test problem (1.7): $\Omega_0 = D$. In general, however, the projection P_Γ can be constructed using different APs. Therefore, if the AP changes so does the operator G , and hence P_Γ , but the range $\text{Im} P_\Gamma$ remains unaffected. This is similar to changing the projection angle onto the same subspace [88]. The flexibility in choosing the AP allows one to pick a formulation that is convenient and easy to solve. For example, for constant coefficients one may use the FFT. If L has constant coefficients and G is given by convolution with the fundamental solution of L , then (1.12) reduces to the classical Green's formula. In our case, the coefficients are not constant, because κ^2 in (1.6) depends on c . Therefore, we will be solving the AP by multigrid iterations, see Section 1.2.5.

Once the BEP (1.14) holds, the corresponding solution u is given by $u = P_\Omega \xi_\Gamma + Gf$. If u is to satisfy some boundary condition on Γ : $l_\Gamma u = \phi$, then this boundary condition is recast as

$$l_\Gamma (P_\Omega \xi_\Gamma + Gf) = \phi, \quad (1.15)$$

and the system of equations (1.14), (1.15) is solved with respect to ξ_Γ . In doing so, the boundary condition $l_\Gamma u = \phi$ can be very general (e.g., mixed, discontinuous, etc.) yet the system (1.14), (1.15) on Γ is still equivalent to the original boundary value problem on Ω , including variable coefficients.

Assume that the original problem is uniquely solvable and well-posed. Then, the equivalent boundary problem (1.14), (1.15) is also well-posed. For example, consider the homogeneous case: $Lu = 0$ on Ω and $l_\Gamma u = \phi$ on Γ , for which the equivalent boundary formulation is $P_\Gamma \xi_\Gamma - \xi_\Gamma = 0$ and $l_\Gamma (P_\Omega \xi_\Gamma) = \phi$. If the original problem is well-posed, then $\|u\| \leq c \|\phi\|$. Consequently, $\|\xi_\Gamma\| \leq c_1 \|\phi\|$, because $\xi_\Gamma = \text{Tr} u$. Let ψ_Γ be a perturbation, so that instead of the true unperturbed boundary problem we are solving $P_\Gamma \xi_\Gamma - \xi_\Gamma = \psi_\Gamma$ and $l_\Gamma (P_\Omega \xi_\Gamma) = \phi$. Then, we have $\|\xi_\Gamma\| \leq C(\|\phi\| + \|\psi_\Gamma\|)$, where the constant C depends on $\|P_\Omega\|$ and $\|P_\Gamma\|$, but does not depend on ϕ or ψ_Γ , see [88,

Part II, Chapter 1].

The actual discrete implementation of the MDP is discussed in Section 3.2.

1.2.5 Multigrid Methods

Multigrid methods are a family of fast iterative methods for solving systems of linear algebraic equations derived from discretizations of elliptic PDEs. Multigrid methods are extremely flexible in their application. They can be used for problems with constant or variable coefficients, problems that are linear or nonlinear, problems with simple or complicated geometry, scalar problems or systems of equations or any combination of the above. Unlike Krylov subspace methods, multigrid methods theoretically achieve rates of convergence that are independent of the condition number. In other words, the rate at which the error improves is constant regardless of grid size. As a consequence the computational complexity of multigrid methods scales similarly to that of FFT i.e. $\mathcal{O}(N \ln N)$ floating point arithmetic operations. The leading constants that characterize multigrid floating point operators methods are usually larger than those for FFT, but multigrid methods apply to a much broader class of formulations including, in particular, equations with variable coefficients.

For a concrete example, consider Poisson's equation $\Delta u = f$ on the cubic domain D with Dirichlet boundary conditions discretized uniformly in space using second order central differences. Since the resulting linear system is symmetric positive definite, there exists an orthonormal basis of eigenvectors. Therefore we can write our error as a linear combination of these orthonormal eigenvectors. Multigrid methods rely on the smoothing principle and the coarse grid principle. A smoother is an operator which rapidly damps the high frequency components of the error. Once the high frequency components of the error are small, the error is said to be smooth since a linear combination of low frequency components can be visually represented by a smooth graph. Note that a smooth error isn't necessarily small, just that the high frequency components of the error are small. For the coarse grid principle, suppose we have two nested grids uniformly discretized by h and $2h$ respectively and a smooth error on the fine grid. The coarse grid property states that a smooth error on the fine grid is well approximated on the coarse grid. Note that the coarse grid has roughly one-eighth as many nodes as the fine grid. The coarse grid principle will be used to create a divide and conquer approach to eliminate the smooth error from the fine grid.

Next we will consider the given EPDE

$$\begin{aligned} \mathbf{L}u &= f \text{ on } \Omega \subset \mathbb{R}^3, \\ \mathbf{l}_\Gamma(u) &= g \text{ on } \Gamma = \partial\Omega, \end{aligned}$$

whose discrete counterpart is

$$\begin{aligned} \mathbf{L}_h u_h &= f_h \text{ on } \Omega_h, \\ \mathbf{l}_{\Gamma_h}(u_h) &= g_h \text{ on } \Gamma_h = \partial\Omega_h \cap \Gamma, \end{aligned}$$

using a uniform grid size of h . Let $\mathcal{G}(\Omega_h)$ denote the space of all grid functions defined on Ω_h . Then a standard multigrid method consists of the following components:

- ◇ Coarse Grids: Multigrid methods require nested grids in order to work. The simplest choice to obtain a nested grid is to double the grid length along each axis. As a consequence the nested grid $|\Omega_{2h}| \approx \frac{1}{8}|\Omega_h|$ where $\Omega \subset \mathbb{R}^3$.
- ◇ Smoother: $\text{smooth}^v(\mathbf{L}_h, v_h, f_h) : \mathcal{G}(\Omega_h) \rightarrow \mathcal{G}(\Omega_h)$ applies v applications of an iterative solver given the linear system \mathbf{L}_h , initial guess v_h , and RHS term f_h . A smoother must have the smoothing property, meaning that the error becomes smooth (not necessarily small) after a few iterations. In other words the smoother damps the high frequency components of the error, leaving the low frequency components intact. Jacobi iterations, Gauss-Seidel iterations, or successive over relaxations are commonly used as smoothers.
- ◇ Restriction operator: $\mathcal{R}_h^H : \mathcal{G}(\Omega_h) \rightarrow \mathcal{G}(\Omega_H)$ Transfers a grid function from the fine grid to the coarse grid. Given a grid point on the coarse grid, the restriction operator computes a weighted average of neighboring nodes of the fine grid. Injection and full weighting operators are commonly used as restriction operators.
- ◇ Prolongation operator: $\mathcal{P}_H^h : \mathcal{G}(\Omega_H) \rightarrow \mathcal{G}(\Omega_h)$ transfers a grid function on the coarse grid to the fine grid. For any node belonging to $\Omega_h \setminus \Omega_H$ the prolongation operator uses polynomial interpolation from the neighboring nodes of the coarse grid to define the grid function at this node on the fine grid. If the node belongs to $\Omega_H \cap \Omega_h$, then the value of the grid function is unmodified. Linear interpolation

along each axis (tri-linear interpolation) or cubic interpolation along each axis (tri-cubic interpolation) are commonly used for polynomial interpolation which define the prolongation operator.

- ◇ Coarse grid operator: $L_H : \mathcal{G}(\Omega_H) \rightarrow \mathcal{G}(\Omega_H)$ is the discrete EPDE utilizing a stepsize of H . Since we are using FDM over a cube this is sufficient. In the context of unstructured grids we may want to use the coarse grid operator defined by the Galerkin condition $L_H = \mathcal{P}_H^h L_h \mathcal{R}_h^H$ where $\mathcal{R}_h^H = a(\mathcal{P}_H^h)^T$ for some real number a .

Algorithm 1 One iteration TGC for solving $L_h u_h = f_h$.

- | | |
|--|---|
| 1: $v_h \leftarrow \text{smooth}^{\nu_1}(L_h, u_h^{(j)}, f_h)$ | ▷ Apply smoother ν_1 times to initial guess. |
| 2: $r_h = f_h - L_h v_h$ | ▷ Compute the residual. |
| 3: $r_{2h} = \mathcal{R}_h^{2h} r_h$ | ▷ Restrict the residual to the coarse grid. |
| 4: $e_{2h} = L_{2h}^{-1} r_{2h}$ | ▷ Solve the coarse grid system directly. |
| 5: $v_h \leftarrow v_h + \mathcal{P}_{2h}^h e_{2h}$ | ▷ Coarse grid correction. |
| 6: $v_h \leftarrow \text{smooth}^{\nu_2}(L_h, v_h, f_h)$ | ▷ Apply smoother ν_2 times. |
| 7: $u_h^{(j+1)} \leftarrow v_h$ | ▷ Obtain the next approximate solution to $L_h u_h = f_h$. |
-

To see how the above components are used, consider one iteration of the simplest multigrid method, the two grid cycle (TGC). The two grid cycle is depicted in Algorithm 1. First, a smoother is applied ν_1 times on the fine grid to damp the high frequency components of the error. The remainder of the algorithm is spent removing the smooth error (remaining low frequency components of the error). If the error satisfies $e_h = u_h - v_h$, then discrete EPDE satisfies the residual problem

$$\begin{aligned} L_h e_h &= r_h = f_h - L_h v_h, \text{ on } \Omega_h, \\ \mathbf{l}_{\Gamma_h}(e_h) &= \tilde{g}_h = g_h - \mathbf{l}_{\Gamma_h}(u_h) \text{ on } \Gamma_h = \partial\Omega_h \cap \Gamma. \end{aligned}$$

We will use the coarse grid property to solve the residual system for the error on the coarse grid where the solver will be less expensive to compute. To accomplish this end, we compute the fine grid residual, r_h , then transfer it to the coarse grid using the restriction operator. In other words the coarse grid residual $r_{2h} = \mathcal{R}_h^{2h} r_h$. Assuming

the high frequency components of the error are small, the coarse grid principle states that $r_h \approx r_{2h}$ on the coarse grid. Similarly the residual system on the coarse grid

$$\begin{aligned} \mathbf{L}_h e_{2h} &= r_{2h}, \text{ on } \Omega_{2h}, \\ \mathbf{l}_{\Gamma_h}(e_{2h}) &= \tilde{g}_h = g_{2h} - \mathbf{l}_{\Gamma_h}(u_{2h}) \text{ on } \Gamma_{2h} = \partial\Omega_{2h} \cap \Gamma. \end{aligned}$$

Note that $|\Omega_{2h}| \approx \frac{1}{8}|\Omega_h|$ if we neglect the boundary. Its less expensive to solve the residual problem on the coarse grid and transfer the coarse error to the fine grid with the prolongation operator than solve the residual system on the fine grid. We eliminate the smooth error on the fine grid using coarse grid correction. In other words $u_h = v_h + e_h \approx v_h + \mathcal{P}_{2h}^h e_{2h}$. Finally, we apply the smoother ν_2 more times to damp any remaining errors.

The TGC gives an incisive view of how the smoothing principle and coarse grid principles are used to solve the discrete EPDE and how the components interact. However, the TGC is impractical for problems with very fine grids. If $|\Omega_h|$ is very large, then solving for the coarse grid error on Ω_{2h} will be expensive despite the coarse grid Ω_{2h} having about an eighth of the nodes in the fine grid Ω_h . However, we can use the TGC recursively to construct an efficient multigrid method. Note that residual system on the coarse grid $\mathbf{L}_{2h} e_{2h} = r_{2h}$ can be solved with the TGC as well if we treat r_{2h} as a given RHS. This begets another residual system on an even coarser grid. Preceding in this fashion produces an additional grid with roughly an eighth of nodes from the previous grid fine grid. This method can be used to construct a family of fast multigrid methods. Suppose we predetermine the ℓ nested grids $\Omega_{2^{i-1}h}$ for $i = 1, 2, \dots, \ell$ where $|\Omega_{2^{\ell-1}h}| \ll |\Omega_h|$. We will refer to any recursive application of the TGC which visits each nested grid at least once as a multigrid cycle (MGCYC). Multigrid cycles are used in practice over the TGC because we can solve for the smooth error directly on the coarsest grid ($\Omega_{2^{\ell-1}h}$) where computational costs are small relative to the fine grid (Ω_h), then use coarse grid correction to remove the smooth errors as we work our way back to the finest grid. While there are an infinite number of MGCYC we could employ, we only consider the V , F , and W cycles. The V -cycle is derived by applying the TGC on each level once and only once per cycle. The W -cycle is similar to the V -cycle except that the TGC is applied recursively twice on each level. The F -cycle is a mixture between between the V and W cycles. Algorithm 2 and 3 depict the $V(\nu_1, \nu_2)$ cycle and the $F(\nu_1, \nu_2)$ cycles respectively using

for loops.

Algorithm 2 The $V(\nu_1, \nu_2)$ cycle for solving $\mathbf{L}_h u_h = f_h$ when using ℓ nested grids given the approximate solution $u_h^{(j)}$.

- 1: Let $b_h = f_h$, $v_h = u_h^{(j)}$, and $v_{2^{i-1}h} = 0 = b_{2^{i-1}h}$ for $i = 2, 3, \dots, \ell$ \triangleright Initialize on each level.
 - 2: **for** $i = 1$ to $\ell - 1$ **do**
 - 3: $v_{2^{i-1}h} \leftarrow \text{smooth}^{\nu_1}(\mathbf{L}_{2^{i-1}h}, v_{2^{i-1}h}, b_{2^{i-1}h})$ \triangleright Apply smoother ν_1 times.
 - 4: $b_{2^i h} \leftarrow \mathcal{R}_{2^{i-1}h}^{2^i h}(b_{2^{i-1}h} - \mathbf{L}_{2^{i-1}h} v_{2^{i-1}h})$ \triangleright Restrict residual to the next grid.
 - 5: **for** $i = \ell$ **downto** 1 **do**
 - 6: **if** $i = \ell$ **then**
 - 7: $\mathbf{L}_{2^{\ell-1}h} v_{2^{\ell-1}h} = b_{2^{\ell-1}h}$ \triangleright Direct solve or fast iterative solver on the ℓ^{th} grid.
 - 8: $v_{2^{\ell-2}h} \leftarrow v_{2^{\ell-2}h} + \mathcal{P}_{2^{\ell-2}h}^{2^{\ell-1}h} v_{2^{\ell-1}h}$ \triangleright Correct the iterate on $(\ell - 1)^{\text{th}}$ grid.
 - 9: **else if** $\ell < i < 1$ **then**
 - 10: $v_{2^{i-1}h} \leftarrow \text{smooth}^{\nu_2}(\mathbf{L}_{2^{i-1}h}, v_{2^{i-1}h}, b_{2^{i-1}h})$ \triangleright Apply smoother ν_2 times.
 - 11: $v_{2^{i-2}h} \leftarrow v_{2^{i-2}h} + \mathcal{P}_{2^{i-2}h}^{2^{i-1}h} v_{2^{i-1}h}$ \triangleright Correct the iterate on $(i - 1)^{\text{th}}$ grid.
 - 12: **else if** $i == 1$ **then**
 - 13: $v_h \leftarrow \text{smooth}^{\nu_2}(\mathbf{L}_h, v_h, b_h)$ \triangleright Apply smoother ν_2 times on the finest grid.
 - 14: $u_h^{(j+1)} \leftarrow v_h$ \triangleright Obtain the improved solution to $\mathbf{L}_h u_h = f_h$.
-

In Figure 1.1 we depict diagrams of the V , F , and W cycles respectively when using a total of $\ell = 4$ nested grids. The southeast arrow indicates that the smoother has been applied, the residual has been computed on the fine grid, the restriction operator has been applied to residual from the fine grid, and the restricted residual is recorded as the RHS of the coarse grid. The northeast arrow indicates that the error from the coarse has been interpolated to the fine grid and coarse grid correction has been applied on the fine grid. Ranking the MGCYC on convergence rates from best to worst is W , F , and V cycles respectively. However, W cycles do incur the most floating point operations per cycle since it spends more time on the coarse grids.

Algorithm 4 depicts our termination criteria when calling the MGCYC. Table 1.1 lists our settings for MGCYC. All of our simulations will use these settings. For introductions to multigrid methods see [14, 89]. For a more advanced treatment of multigrid methods see [100].

Algorithm 3 The $F(v_1, v_2)$ cycle for solving $\mathbf{L}_h u_h = f_h$ when using ℓ nested grids given the approximate solution $u_h^{(j)}$.

- 1: Let $b_h = f_h$, $v_h = u_h^{(j)}$, and $v_{2^{i-1}h} = 0 = b_{2^{i-1}h}$ for $i = 2, 3, \dots, \ell$ ▷ Initialize on each level.
 - 2: **for** $i = 1$ to $\ell - 1$ **do**
 - 3: $v_{2^{i-1}h} \leftarrow \text{smooth}^{v_1}(\mathbf{L}_{2^{i-1}h}, v_{2^{i-1}h}, b_{2^{i-1}h})$ ▷ Apply smoother v_1 times.
 - 4: $b_{2^i h} \leftarrow \mathcal{R}_{2^{i-1}h}^{2^i h}(b_{2^{i-1}h} - \mathbf{L}_{2^{i-1}h} v_{2^{i-1}h})$ ▷ Restrict residual to the next grid.
 - 5: $\mathbf{L}_{2^{\ell-1}h} v_{2^{\ell-1}h} = b_{2^{\ell-1}h}$ ▷ Direct solve or fast iterative solver on the ℓ^{th} grid.
 - 6: $v_{2^{\ell-2}h} \leftarrow v_{2^{\ell-2}h} + \mathcal{P}_{2^{\ell-2}h}^{2^{\ell-1}h} v_{2^{\ell-1}h}$ ▷ Correct the iterate on $(\ell - 1)^{\text{th}}$ grid.
 - 7: **for** $j = \ell - 1$ **downto** 2 **do**
 - 8: **for** $i = j$ to $\ell - 1$ **do**
 - 9: $v_{2^{i-1}h} \leftarrow \text{smooth}^{v_1}(\mathbf{L}_{2^{i-1}h}, v_{2^{i-1}h}, b_{2^{i-1}h})$ ▷ Apply smoother v_1 times.
 - 10: $b_{2^i h} \leftarrow \mathcal{R}_{2^{i-1}h}^{2^i h}(b_{2^{i-1}h} - \mathbf{L}_{2^{i-1}h} v_{2^{i-1}h})$ ▷ Restrict residual to the next grid.
 - 11: **for** $i = \ell$ **downto** j **do**
 - 12: **if** $i = \ell$ **then**
 - 13: $\mathbf{L}_{2^{\ell-1}h} v_{2^{\ell-1}h} = b_{2^{\ell-1}h}$ ▷ Direct solve or fast iterative solver on the ℓ^{th} grid.
 - 14: $v_{2^{\ell-2}h} \leftarrow v_{2^{\ell-2}h} + \mathcal{P}_{2^{\ell-2}h}^{2^{\ell-1}h} v_{2^{\ell-1}h}$ ▷ Correct the iterate on $(\ell - 1)^{\text{th}}$ grid.
 - 15: **else if** $\ell < i \leq j$ **then**
 - 16: $v_{2^{i-1}h} \leftarrow \text{smooth}^{v_2}(\mathbf{L}_{2^{i-1}h}, v_{2^{i-1}h}, b_{2^{i-1}h})$ ▷ Apply smoother v_2 times.
 - 17: $v_{2^{i-2}h} \leftarrow v_{2^{i-2}h} + \mathcal{P}_{2^{i-2}h}^{2^{i-1}h} v_{2^{i-1}h}$ ▷ Correct the iterate on $(i - 1)^{\text{th}}$ grid.
 - 18: $v_h \leftarrow \text{smooth}^{v_2}(\mathbf{L}_h, v_h, b_h)$ ▷ Apply smoother v_2 times.
 - 19: $u_h^{(j+1)} \leftarrow v_h$ ▷ Obtain the improved solution to $\mathbf{L}_h u_h = f_h$.
-

Algorithm 4 Termination Criteria of MG CYC when solving $\mathbf{L}_h u_h = f_h$ given the initial guess $u_h^{(0)}$. Take the absolute tolerance, relative tolerance, cycle type, maximum iteration count, and pre/post sweeps (v_1, v_2) as given parameters.

- 1: Compute the residual of the initial guess: $r_h = r_h^{(0)} = f_h - \mathbf{L}_h u_h^{(0)}$.
 - 2: numCycles = 0
 - 3: **if** $\|r_h\| > \text{relTolerance} r_h^{(0)} + \text{absTolerance}$ **AND** $\text{numCycles} \leq \text{maxIterations}$ **then**
 - 4: Update approximation: $u_h \leftarrow \text{MG CYC}(\mathbf{L}_h, f_h, u_h, v_1, v_2, \text{cycleType})$
 - 5: Compute new residual: $r_h = f_h - \mathbf{L}_h u_h$
 - 6: Count the addition cycle: $\text{numCycles} = \text{numCycles} + 1$
-

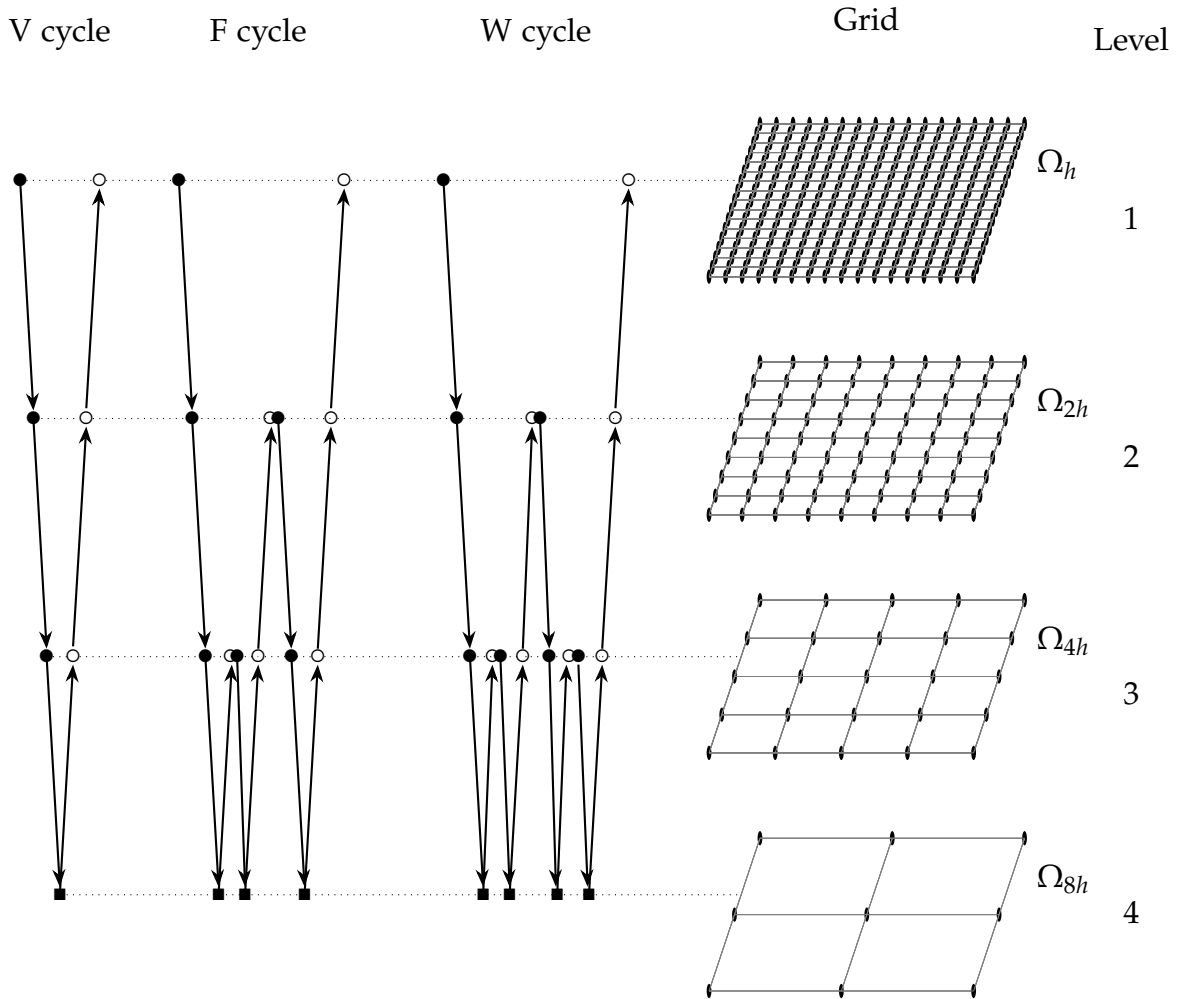


Figure 1.1: Schematic of three common MG CYC. The symbols (\bullet) denote pre-smoothing steps, (\circ) — post-smoothing steps, (\blacksquare) — direct solver, (\searrow) — restriction, and (\nearrow) — prolongation + coarse grid correction.

1.3 Potential Applications

Mathematical models for the various imaging scenarios that range from medicine to seismology are formulated as inverse problems that involve the acoustic wave equation (1.1). Therefore, numerical solution of this equation becomes an important component of the corresponding image processing algorithms and the efficiency of the latter depends on the efficiency of the wave equation solvers.

Table 1.1: Given the cube $D = [x_l, x_r]^3$, we use the following settings for MGCYC.

Multigrid Component	Setting
# auxiliary grids	ℓ
# grid points per axis (w/o boundary points) (N)	$2^\ell - 1$
uniform step size fine grid (h)	$\frac{x_r - x_l}{2^\ell}$
Smoother	Gauss-Seidel
Restriction Operator	Full-Weighting
Prolongation Operator	Tri-Cubic Interpolation
absolute tolerance	10^{-12}
relative tolerance	10^{-12}

1.3.1 Electrical Impedance Tomography (EIT)

Electric Impedance Tomography (EIT) is a method for determining the electrical properties of a body, Ω . The time varying electrical properties are of interest for medical applications including: detecting blood clots or accumulating fluid in the lungs, monitoring internal bleeding, determining the boundary between living or dead flesh, or measuring the local internal temperature associated with hyperthermia treatments. For a survey of EIT, see [25].

In [42], the authors give a mathematical description of the EIT. The EIT is performed by applying a voltage on the surface Γ of the body Ω which induces an electric potential in the body Ω . One then measures the current on Γ and reconstructs the conductivity in the body using the current and voltage measured on Γ . On its own, the EIT is ill-posed. To overcome this limitation, we can combine EIT with another imaging technique such as ultrasound tomography. In addition to applying a voltage on the surface of the body Γ , ultrasound applied to the body Ω induces pressure changes which can also be recorded on Γ . These pressure can be used to determine the absorbed energy. Assuming the electric potential reaches equilibrium almost instantly, the voltage is applied for a short time, the stimulating effect on the nerves is small, and the change in temperature is large enough to produce ultrasound waves, the governing equations are given by

$$\begin{aligned}\nabla \cdot (\sigma(\mathbf{x})\nabla u) &= 0, & \mathbf{x} \in \Omega, \\ u(\mathbf{x}) &= \varphi_\Gamma, & \mathbf{x} \in \Gamma,\end{aligned}$$

and

$$\begin{aligned}\frac{\partial^2 p}{\partial t^2} - \Delta p &= 0, \quad \mathbf{x} \in \mathbb{R}^3, \\ p(\mathbf{x}, 0) &= \sigma(\mathbf{x}) |\nabla u(\mathbf{x})|^2, \quad \mathbf{x} \in \mathbb{R}^3, \\ \frac{\partial p}{\partial t}(\mathbf{x}, 0) &= 0, \quad \mathbf{x} \in \mathbb{R}^3,\end{aligned}$$

where $\varphi_\Gamma(\mathbf{x})$ is the time-invariant voltage applied to the surface of the body, $\sigma(\mathbf{x})$ is the conductivity, and $u(\mathbf{x})$ is the electric potential. The current satisfies $j(\mathbf{x}) = \sigma(\mathbf{x}) \frac{\partial u}{\partial n}$. The inverse problem of impedance-acoustic tomography consists of reconstructing the conductivity σ from the knowledge of the voltage φ_Γ , current $j(\mathbf{x})$, and pressure, p . If we take advantage of the time reversal of the acoustic pressure field [19], we can utilize our time marching scheme to solve the acoustic wave equation.

1.3.2 Photoacoustic Tomography (PAT)

Photoacoustic Tomography (PAT) also known as thermoacoustic tomography is an ultrasound technique augmented with electromagnetic effects to increase image contrast. The technique works by emitting an electromagnetic pulse to irradiate some biological tissue. By the thermoacoustic effect, acoustic signals are emitted. These acoustic signals can be measured along the boundary of the tissue using transducers. The image is constructed using the acoustic measurements along the boundary of the tissue. The electromagnetic energy and initial pressure are much higher in cancerous tissue than in healthy tissue so determining this initial pressure can serve as a diagnostic tool.

Assume that our tissue is given by $\Omega \subset \mathbb{R}^3$ and our point like omni-directional transducers are located on Γ . Then we can formulate the PAT problem as an inverse problem

$$\begin{aligned}\frac{\partial^2 u}{\partial t^2} &= c^2(\mathbf{x}) \Delta u, \quad (\mathbf{x}, t) \in \Omega \times [0, T], \\ u(\mathbf{x}, 0) &= f(\mathbf{x}), \quad \mathbf{x} \in \Omega, \\ \frac{\partial u}{\partial t}(\mathbf{x}, 0) &= 0, \quad \mathbf{x} \in \Omega, \\ u(\mathbf{x}, t) &= \varphi_\Gamma(\mathbf{x}, t), \quad \mathbf{x} \in \Gamma,\end{aligned}$$

where the objective is to find the initial pressure f given the known measurements on the surface of the tissue [91]. If we utilize the time reversal of the acoustic pressure field [19], then our time marching schemes can be used for solving the wave equation. For more on PAT, see [3, 106, 107, 108, 109].

1.3.3 Full Waveform Inversion (FWI)

Full-waveform inversion (FWI) is an inverse problem which seeks to minimize the discrepancy between the observed measurements and synthetic measurements generated from solving a seismic wave equation. More specifically, FWI seeks to minimize some objective function which depends on the discrepancy between the observed and synthetic measurements in an iterative approach. For every iteration, a seismic wave equation must be solved in order to correct the discrepancy. Therefore, the ability to solve the FWI depends on the ability solve a seismic wave equation accurately and efficiently. When the synthetic measurements are modeled by the acoustic wave equation, we believe our scheme can accomplish this goal for large scale applications in 3D.

Recall that, our scheme solves the acoustic wave equation by solving an elliptic PDE at every step. This elliptic PDE is solved fast ($\mathcal{O}(N \log N)$ floating point operations) with geometric multigrid. Another notable feature of multigrid is that the rate of convergence is independent of the condition number (hence, the number of grid points). Both of these features suggest that our scheme will scale well for large-scale applications in \mathbb{R}^3 . Next consider that, our scheme can be sped up with parallel computing. The most computationally intensive portion of our scheme is the multigrid solver, and geometric multigrid is a sequential algorithm (see Section 1.2.5 for a short description). However, components of the multigrid methods can be sped up. One of the most expensive portions of multigrid is the application of the smoother which is Gauss-Seidel in all of our simulations. Among the standard stationary iterative methods: Jacobi, Gauss-Seidel, and successive over-relaxation (SOR), Jacobi's method is the most parallelizable, but has the worst smoothing properties. Conversely, Gauss-Seidel has the best smoothing properties but is a sequential algorithm. So how can we exploit the good smoothing properties of Gauss-Seidel while making it parallelizable? We can use a multicolor Gauss-Seidel as a smoother. The compact scheme stencil has 19 grid nodes in total if you consider a full $3 \times 3 \times 3$ stencil

with the corner nodes removed. This means our scheme is four colorable [114], i.e., can partition the grid into four non-overlapping sets of grids which can be treated separately. Instead of performing lexicographic Gauss-Seidel, we will perform a sweep of Gauss-Seidel within one of these non-overlapping grid sets before moving onto the next. For a given sweep, we can assign multiple processors to each grid set. For more on multicolor smoothing, see [2]. For a complete description of parallel computing and multigrid, see [100]. Third, our scheme is capable of using high order artificial boundary conditions to truncate an unbounded problem in seismology such as required in oil and gas exploration or seismic hazard mitigation where the area of interest is hundreds of kilometers while the truncated part is the rest of the earth. And finally, our scheme has high order accuracy, which helps reduce the dispersion errors. For a complete description of FWI in 3D seismology, see [24]. Examples of FWI in large scale application are given in [11, 31, 38, 48, 73, 74, 120, 103, 105].

1.3.4 Reverse Time Migration

Seismic imaging in general is a method of mapping subsurface structures and properties using seismic data. Reverse time migration is a seismic imaging technique which extrapolates seismic data from recording receivers on the surface to subsurface reflectors. Reverse time migration requires three components in general. The first one is a forward wave field generated by an acoustic wave equation with an estimated source wavelet. The second one is a backward wave field generated by an acoustic wave equation using the time reversed wave field from the forward problem source functions. The last component needed by the reverse time migration is an image condition, which is a quantity which accounts for the time history of the forward wave field and backward wave field and best matches the data to produce a high fidelity image. Our time marching scheme can be employed to generate the two wave fields fast. Since our scheme is high order accurate, it will reduce the numerical dispersion. This will aid in producing a better image. One of the biggest drawbacks of the reverse time migration for three-dimensional problems is the large memory requirements since the image condition requires the time history of two wave fields. One way we can mitigate these storage costs is to choose a computational domain just "tight" enough to contain the receivers and reflectors and choose an artificial boundary condition of sufficiently high order to guarantee the spurious reflections are small. Another

option to save storage costs is to store the forward wave fields around the boundaries, then use these stored values for backward propagation. Since our scheme uses the method of difference potentials, all points which straddle the continuous boundary can be represented by an extension operator written in terms of the spectral form of the trace $(u, \frac{\partial u}{\partial n})$. Provided the solutions are smooth and we choose an orthonormal basis properly, the number of coefficients needed to represent the trace will be much smaller than the total number of nodes which straddle the continuous boundary. We believe our fourth order compact scheme has the capacity to alleviate some the memory demands of reverse time migration under suitable assumptions. For a survey of reverse time migration, see [116].

1.3.5 Time Reversal

Time reversal is a method for solving a class of inverse problems in wave propagation. Specifically, time reversal aims to determine the initial source in an acoustic medium using recorded values on the boundary of the domain. Time reversal exploits the reversibility of wave propagation in nondissipative media by “time marching backwards” to determine the location of the source that initially generated them.

Consider the finite domain Ω which contains the support of the source term we wish to identify. In addition, assume we place several receivers on the boundary Γ of Ω to record the acoustic wave which emanate from the source. After some time, T , the waves will encounter our receivers on Γ . The time reversal method solves an acoustic wave equation with respect to the reversed time $\tilde{t} = t - T$ treating the measured values on Γ as “source” terms until $\tilde{t} = T$. We then use the backwards propagated waves in time to determine the support of the initial source term which generated the waves measured on Γ .

In addition to source identification, the time reversal method can be used to identify obstacles. This works because the scattering of incident waves act as a “source” with respect to the reflected waves. So the logic of the source identification applies to the obstacle. As an added benefit, the time reversal method works better the more heterogeneous the medium.

Our fast time marching scheme can perform this time marching scheme efficiently with high order accuracy. For a survey of time reversal method see [46]. For applications of of time reversal to source identification see [5, 61, 62, 63, 84]. For applications

to identifying obstacles see [6, 29, 60, 83]

1.3.6 Hybrid Solver for Seismic Wave Motion

The survey paper [82] defines a hybrid method loosely as a combination of “standard” techniques to exploit their advantages to construct a more powerful method. These techniques include finite difference methods, finite element methods, spectral element methods, and boundary element methods. Finite difference methods have low computational costs and are simple to implement provided the domain is regular. However, extending finite difference methods to irregular domains is not trivial. In addition, the grid size on the entire computational domain needs to be adjusted depending on the wave speed. A smaller grid size will increase the computational costs and memory demands. Finite element methods offer more geometric flexibility than finite differences. However, finite element methods are slower than finite differences, especially if unstructured grids are employed. Spectral element methods also have more geometric flexibility than finite differences and achieve high order accuracy. In addition, the mass matrices formed by spectral element methods are diagonalizable. However, spectral element methods are typically limited to quadrilateral or hexahedral elements due to employing Gauss-Lobatto-Legendre quadrature nodes. Boundary element methods reduce the dimension of the problem by one. Unfortunately, BEMs are limited to linear homogeneous formulations for which Green’s functions are available. We therefore see that the standard approaches clearly have their trade-offs. Our scheme is able to exploit some of the good qualities of all these standard techniques making it a hybrid method. We obtain our scheme by discretizing the acoustic wave equation in time using the θ -scheme [23, 68] on three consecutive levels. This results in an elliptic PDE on the upper time levels that needs to be solved at every time step. The coefficients of the elliptic PDE do not depend on time. We solve this elliptic PDE by embedding the elliptic BVP into a simple cubic auxiliary domain via the method of difference potentials (Section 1.2.4) and discretizing the PDE using compact finite differences. Since our auxiliary domain is a cube, the finite differences are straightforward to implement. Since we discretize the elliptic PDE with a compact scheme, we are able to obtain high order accuracy without using any additional nodes. In addition, the linear system obtained by discretizing the elliptic PDE can be solved fast with multigrid. This is especially important because our problem is in \mathbb{R}^3 . The method of difference

potentials also reduces our elliptic PDE to an equivalent expression defined on the boundary of the domain similar BEM. However, our scheme applies to a much wider class of problems as it doesn't require a Green's function. As such, our scheme has the capacity to solve problems with variable coefficients which BEM does not permit. One of the most important features of our scheme is the capacity to handle complex geometries. Unlike FEM, it does not rely on unstructured meshes. The method of difference potentials can handle curvilinear boundaries on uniform Cartesian grids with no deterioration of accuracy due to "cut cells." In doing so, the boundary conditions are accommodated using a spectral representation of solution at the boundary and do not need to be approximated on the grid. In summary, our scheme can achieve many of the benefits of the "standard" solution approaches while avoiding some of the drawbacks.

1.4 Outline of the Thesis

Several of the results demonstrated in the subsequent chapters were published or have been accepted for publication. For example, the contents of Chapter 2 were based on the results of [96], and the contents of Chapter 4 were based on the results of [58] and another paper which has been accepted by the ICOSAHOM 2020/2021 Conference Proceedings. Below we will give a short summary of the subsequent chapters of the thesis.

- ◇ **Chapter 2: COMPACT FOURTH ORDER ACCURATE SCHEME.** This chapter lays the foundation for interior and exterior initial boundary value problems. We considers the acoustic wave equation on a cubic domain with homogeneous Dirichlet boundary conditions. We show how to discretize the wave equation on a cubic domain using a $3 \times 3 \times 3 \times 3$ stencil in space-time, demonstrate how to compute the Courant-Friedrichs-Lewy number, and show numerical simulations to see that high order accuracy is met.
- ◇ **Chapter 3: INTERIOR PROBLEM.** This chapter considers the acoustic wave equation on a general domain Ω using the method of difference potentials. We use a cubic auxiliary domain which contains Ω and has homogeneous Dirichlet boundary conditions. As a consequence we can use the scheme derived

in Chapter 2 despite the uniformly discretized auxiliary domain having non-conforming geometry with Ω .

- ◇ **Chapter 4: RADIATION OF WAVES BY A KNOWN SOURCE.** This chapter considers the acoustic wave equation on \mathbb{R}^3 . We take two approaches. The first approach is to terminate the wave equation with a sponge layer on a cubic computational domain. The second approach is to terminate the domain with a high order artificial boundary condition on a spherical outer boundary. Then we use the method of difference potentials on a cubic auxiliary domain to solve the problem. Both approaches utilize the same methodology as Chapters 2 and 3.
- ◇ **Chapter 5: EXTERIOR SCATTERING PROBLEM** This chapter considers the acoustic wave equation on the complement of some domain Ω . We will truncate the problem with a high order artificial boundary condition with a spherical outer boundary which contains Ω . We will choose a cubic auxiliary domain so we can use the same methodology as Chapters 2, 3, and 4.
- ◇ **Chapter 6: CONCLUSIONS.** Here we summarize our accomplishments in this thesis and some ways to build on the work we have done.

1.5 Mathematical Contributions

The following is a very short summary of our contributions towards the numerical simulation of partial differential equations. This thesis lead to the following journal articles listed in reverse chronological order:

- ◇ Smith F, Tsynkov S, Turkel E. High Order Solution to Exterior 3D Wave Equation by the Method of Difference Potentials. *To appear in the Proceedings of the International Conference on Spectral and High Order Methods 2020/2021.* 2022
- ◇ Kahana A, Smith F, Turkel E, Tsynkov S. A high order compact time/space finite difference scheme for the 2D and 3D wave equation with a damping layer. *Journal of Computational Physics.* 2022;460
- ◇ Smith F, Tsynkov S, Turkel E. Compact High Order Accurate Schemes for the Three Dimensional Wave Equation. *Journal of Scientific Computing.* 2019;18:1181–1209.

In addition parts of this work were presented at the conferences:

- ◇ "3D Scheme for the Interior or Exterior Initial Boundary Value Problems for the Wave Equation," International Conference on Spectral and High Order Methods 2020/2021, Vienna
- ◇ "A Fourth Order Compact Scheme for the 3D Wave Equation with Variable Propagation Speed," International Conference on Spectral and High Order Methods 2018, London

Chapter 2

COMPACT FOURTH ORDER ACCURATE SCHEME

In this chapter we will discretize the acoustic wave equation

$$\begin{aligned}\frac{\partial^2 u}{\partial t^2} - c^2(\mathbf{x})\Delta u &= F(\mathbf{x}, t), \quad (\mathbf{x}, t) \in D \times (0, T), \\ u(\mathbf{x}, 0) &= \varphi_0(\mathbf{x}), \quad \mathbf{x} \in D, \\ \frac{\partial u}{\partial t}(\mathbf{x}, 0) &= \varphi_1(\mathbf{x}), \quad \mathbf{x} \in D, \\ u &= 0, \quad \mathbf{x} \in \partial D,\end{aligned}\tag{2.1}$$

with fourth order accuracy in time both time and space on the cubic domain D . We will accomplish this high order discretization using only three levels in time and three levels along the x , y , and z axes respectively. The acoustic wave equation (2.1) will lay the foundation for solving interior and exterior problems with the method of difference potentials. We will also use the benchmark problem (2.1) to guarantee that our fast solver is converging at the appropriate rate. This is important because this fast solver will be the most computationally intensive portion used for our analogous for interior and exterior problems. In Section 2.1 we discretize the acoustic wave equation (2.1) in time using the θ -scheme [23, 68]. The θ -scheme uses three consecutive levels in time and produces a one parameter family of elliptic PDEs on the upper time level where the RHS term contains known quantities from the previous time levels. The parameter θ is chosen to produce fourth order accuracy in time. In Section 2.2 we show how to discretize the elliptic PDE from the θ -scheme with fourth order

accuracy in space using an equation based compact finite difference scheme (See Section 1.2.1 for description). In Section 2.3 we show how to estimate the CFL number using an energy based argument. In Section 2.4 we depict the algorithm for the fourth order time marching scheme needed to solve (2.1). In Section 2.5 we demonstrate empirically and quantitatively that our multigrid method achieves the optimal rate of convergence. Finally, Section 2.6 provides several simulations to demonstrate the fourth order compact scheme achieves the desired order of accuracy.

2.1 Semi-Discrete Approximation in Time

Let τ denote the uniform time step. Consider the acoustic wave equation (2.1) at the n^{th} time level $t^n = n\tau$ for a given $\mathbf{x} \in D$. Applying the θ -scheme [23, 68] to (2.1) produces the semi-discrete scheme

$$\delta_t^2 u^n = c^2 \Delta u^n + \theta \tau^2 \delta_t^2 \Delta u^n + F^n + \theta \tau^2 \delta_t^2 F^n, \quad \theta \in \mathbb{R} \setminus \{0\}, \quad (2.2)$$

where the central difference formula

$$\delta_t^2 u^n = \frac{u^{n+1} - 2u^n + u^{n-1}}{\tau^2}. \quad (2.3)$$

We ignore the case $\theta = 0$ since it produces the second order explicit discretization in time. Substituting (2.3) into (2.2) and rearranging yields the semi-discrete approximation in time

$$\begin{aligned} \left(\Delta u^{n+1} - \frac{u^{n+1}}{\theta \tau^2 c^2} \right) &= 2 \left(\Delta u^n - \frac{u^n}{\theta \tau^2 c^2} \right) - \left(\Delta u^{n-1} - \frac{u^{n-1}}{\theta \tau^2 c^2} \right) - \frac{\Delta u^n}{\theta} \\ &\quad - \frac{1}{c^2} \left(F^{n+1} + \left(\frac{1}{\theta} - 2 \right) F^n + F^{n-1} \right). \end{aligned} \quad (2.4)$$

If we define the variables

$$f^n = \Delta u^n - \kappa^2(\mathbf{x}) u^n, \quad (2.5)$$

$$\kappa^2(\mathbf{x}) = \frac{1}{\theta \tau^2 c^2(\mathbf{x})}, \quad (2.6)$$

then (2.4) simplifies to the modified Helmholtz equation (MHE)

$$\begin{aligned}\Delta u^{n+1} - \kappa^2(\mathbf{x})u^{n+1} &= f^{n+1}, & \mathbf{x} \in D, \\ u^{n+1} &= 0, & \mathbf{x} \in \partial D,\end{aligned}\tag{2.7}$$

where the RHS (def. (2.5)) on the upper time level satisfies the recursive formulas

$$f^{n+1} = 2f^n - f^{n-1} - \frac{1}{\theta}\Delta u^n - \tilde{F}^{n+1}\tag{2.8a}$$

$$= \left(2 - \frac{1}{\theta}\right)f^n - f^{n-1} - \frac{\kappa^2(\mathbf{x})u^n}{\theta} - \tilde{F}^{n+1},\tag{2.8b}$$

and the augmented source term

$$\tilde{F}^{n+1} = \frac{1}{c^2}\left(F^{n+1} + \left(\frac{1}{\theta} - 2\right)F^n + F^{n-1}\right).$$

If $\theta = \frac{1}{12}$, the implicit semi-discrete approximation in time (2.7) is fourth order accurate in time. Solving the acoustic wave equation (2.1) simply amounts to solving a MHE (2.7) at every time step where the RHS term is assembled according to (2.8a) or (2.8b). Of course (2.8b) is more straightforward to implement since it doesn't contain any derivatives which need to be approximated with fourth order accuracy. This is the version we will use for numerical simulations. Furthermore, the coefficients of MHE (2.7) don't vary with time. This implies that the solver associated with the MHE can be pre-computed once in the pre-processing stage and re-used at every time. Since the MHE (2.7) takes place over a cubic domain, we have two fast methods ($\mathcal{O}(N) \log N$) to solve the MHE (2.7). If the "wavenumber" (2.6) is constant we can use the fast Fourier Transform (FFT). Otherwise a geometric multigrid method (See Section 1.2.5) can solve (2.7) efficiently. In the later case we can use the data from previous time steps to provide a very good initial guess to the multigrid method. Using Taylor's Theorem

$$u^{n\pm 1} = u^n \pm \tau \frac{\partial u^n}{\partial t} + \frac{\tau^2}{2} \frac{\partial^2 u^n}{\partial t^2} \pm \frac{\tau^3}{6} \frac{\partial^3 u^n}{\partial t^3} + \frac{\tau^4}{24} \frac{\partial^4 u^n}{\partial t^4} \pm \frac{\tau^5}{120} \frac{\partial^5 u^n}{\partial t^5} + \mathcal{O}(\tau^6).$$

Adding the above and rearranging implies

$$u^{n+1} = 2u^n - u^{n-1} + \tau^2 \frac{\partial^2 u^n}{\partial t^2} + \frac{\tau^4}{12} \frac{\partial^4 u^n}{\partial t^4} + \mathcal{O}(\tau^6).$$

Using the acoustic wave equation (2.1) to replace the second order time derivative in the above implies that

$$u^{n+1} = 2u^n - u^{n-1} + \tau^2 \left(c^2 \Delta u^n + F^n \right) + \frac{\tau^4}{12} \frac{\partial^4 u^n}{\partial t^4} + \mathcal{O}(\tau^6).$$

Accordingly

$$\tilde{u}^{n+1} = 2u^n - u^{n-1} + \tau^2 \left(c^2 \Delta_h u^n + F^n \right), \quad (2.9)$$

where $\Delta_h u^n$ is the central difference approximation to the Laplacian can produce a very good initial guess to the multigrid solver for (2.7). Note that κ^2 is not the wavenumber which describes the variation in linear wave propagation. The notation merely indicates that the coefficient is non-negative and the governing PDE resembles a Helmholtz type equation. The negative sign in front of the “wavenumber” (2.6) is beneficial to solving the MHE (2.7). When discretizing (2.7) in space the “wavenumber” enhances the diagonal dominance of the discrete linear system. When we refine our grid the “wavenumber” only enhances this diagonal dominance since the “wavenumber” (2.6) is inversely proportional to the square of uniform time step τ . This is in stark contrast to the Indefinite Helmholtz Equation $(\Delta + \kappa^2)u = f$ which isn’t amenable to iterative methods for sufficiently large values of κ^2 [32].

2.2 Discrete Modified Helmholtz Equation

In this section we will show how to discretize the generic modified Helmholtz equation

$$\begin{aligned} \Delta u - \kappa^2(\mathbf{x})u &= f, & \mathbf{x} \in D, \\ u &= 0, & \mathbf{x} \in \partial D, \end{aligned} \quad (2.10)$$

for a given RHS f with fourth order accuracy in space. The conventional approach to constructing fourth order accurate schemes would require fourth order central differences or, equivalently, a stencil that contains at least five nodes along each

axis of \mathbb{R}^3 . Instead we will utilize a compact finite difference scheme (Section 1.2.1) to obtain a narrower stencil. In particular we will use the equation based fourth order compact scheme (EBFOCS) described in 1.2.1 to construct a scheme built on a $3 \times 3 \times 3$ stencil in space. Notice that the conventional approach necessitates additional modification near the boundary due to the width of the stencil, while the EBFOCS need no additional treatment near the boundary for Dirichlet boundary conditions. For some examples of compact finite difference schemes applied to the Helmholtz equation see [40, 50, 95, 102].

Given the cubic domain $D = [\bar{x}_l, \bar{x}_r]^3 \subset \mathbb{R}^3$ and the positive integer N , define the uniform step size $h = \frac{\bar{x}_r - \bar{x}_l}{N+1}$ and the coordinates

$$x_i = \bar{x}_l + ih \quad y_j = \bar{x}_l + jh \quad z_k = \bar{x}_l + kh, \quad 0 \leq i, j, k \leq N + 1.$$

Accordingly, the uniformly discretized cube D with step size h is given by the set

$$D_h = \{(x_i, y_j, z_k) \in D \mid 0 \leq i, j, k \leq N + 1\}, \quad (2.11)$$

and the interior grid points of the uniformly discretized cube D are given by

$$D_h^0 = \{(x_i, y_j, z_k) \in D \mid 1 \leq i, j, k \leq N\}. \quad (2.12)$$

Consider the $3 \times 3 \times 3$ stencil depicted in Figure 2.1 centered at the node $(x_i, y_j, z_k) \in D_h^0$ (def. (2.12)). We will refer to grid points demarcated by (■), (●), and (◆) as the side-side, side-corner, and corner-corner nodes respectively. In order to write the equation based fourth order compact scheme economically suppose $u_{i,j,k} \approx u(x_i, y_j, z_k)$, then define the quantities:

$$\begin{aligned} u_{ss} &= u_{i+1,j,k} + u_{i-1,j,k} + u_{i,j+1,k} + u_{i,j-1,k} + u_{i,j,k+1} + u_{i,j,k-1}, \\ u_{sc} &= u_{i+1,j,k+1} + u_{i-1,j,k+1} + u_{i,j+1,k+1} + u_{i,j-1,k+1} + u_{i+1,j+1,k} + u_{i+1,j-1,k} \\ &\quad + u_{i+1,j,k-1} + u_{i-1,j,k-1} + u_{i,j+1,k-1} + u_{i,j-1,k-1} + u_{i-1,j+1,k} + u_{i-1,j-1,k}, \\ u_{cc} &= u_{i+1,j+1,k+1} + u_{i-1,j+1,k+1} + u_{i+1,j-1,k+1} + u_{i-1,j-1,k+1} \\ &\quad + u_{i+1,j+1,k-1} + u_{i-1,j+1,k-1} + u_{i+1,j-1,k-1} + u_{i-1,j-1,k-1}, \end{aligned}$$

where the subscripts ss , sc , and cc correspond to the side-side, side-corner, and corner-corner stencils respectively. Let δ_v^2 , denote the second order central difference operators

for the derivative $\frac{\partial^2}{\partial v^2}$. If we define the central difference operators

$$\Delta_h \stackrel{\text{def}}{=} \delta_x^2 + \delta_y^2 + \delta_z^2,$$

and

$$\mathcal{A}_h \stackrel{\text{def}}{=} \delta_x^2 \delta_y^2 + \delta_x^2 \delta_z^2 + \delta_y^2 \delta_z^2,$$

they can be written economically as

$$\Delta_h u = \frac{u_{ss} - 6u_{i,j,k}}{h^2} \quad \mathcal{A}_h u = \frac{u_{sc} - 4u_{ss} + 12u_{i,j,k}}{h^4}. \quad (2.13)$$

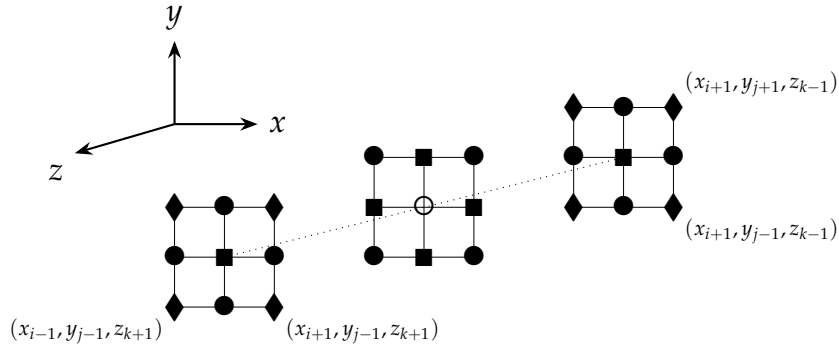


Figure 2.1: The nodes adjacent to the center of the stencil (x_i, y_j, z_k) denoted by (\circ) . The symbols are the side-side nodes (\blacksquare), side-corner nodes (\bullet), and corner-corner nodes (\blacklozenge).

Now we will discretize the generic modified Helmholtz equation (2.10) with fourth order accuracy using our equation based methodology (See 1.2.1). The first thing we will do is discretize the Laplacian with fourth order accuracy. By Taylor Theorem

$$\Delta u = \Delta_h u - \frac{h^2}{12} \left(\frac{\partial^4 u}{\partial x^4} + \frac{\partial^4 u}{\partial y^4} + \frac{\partial^4 u}{\partial z^4} \right) - \frac{h^4}{360} \left(\frac{\partial^6 u}{\partial x^6} + \frac{\partial^6 u}{\partial y^6} + \frac{\partial^6 u}{\partial z^6} \right) + \mathcal{O}(h^6). \quad (2.14)$$

Next we will differentiate the MHE (2.10) to replace the high order unmixed partial derivatives in the $\sim h^2$ term of (2.14). Applying the Laplacian to the MHE (2.10) and

combining like terms yields the expression

$$\frac{\partial^4 u}{\partial x^4} + \frac{\partial^4 u}{\partial y^4} + \frac{\partial^4 u}{\partial z^4} + 2 \left(\frac{\partial^4 u}{\partial x^2 \partial y^2} + \frac{\partial^4 u}{\partial x^2 \partial z^2} + \frac{\partial^4 u}{\partial y^2 \partial z^2} \right) - \Delta(\kappa^2 u) = \Delta f. \quad (2.15)$$

Substituting (2.15) into (2.14) produces

$$\begin{aligned} \Delta u = \Delta_h u - \frac{h^2}{12} \Delta(f + \kappa^2 u) + \frac{h^2}{6} \left(\frac{\partial^4 u}{\partial x^2 \partial y^2} + \frac{\partial^4 u}{\partial x^2 \partial z^2} + \frac{\partial^4 u}{\partial y^2 \partial z^2} \right) \\ - \frac{h^4}{360} \left(\frac{\partial^6 u}{\partial x^6} + \frac{\partial^6 u}{\partial y^6} + \frac{\partial^6 u}{\partial z^6} \right) + \mathcal{O}(h^6). \end{aligned} \quad (2.16)$$

Notice that all the fourth order derivatives in (2.16) contain partial derivatives with at most two derivatives with respect to any one variable. At this point we would replace all the derivatives in the $\sim h^2$ term of (2.16) with their analogous central difference formulas and obtain a fourth order compact scheme. Unfortunately this approach produced an unstable scheme [96]. We didn't do a rigorous analysis to find the origin of this instability. However, we suspected this instability was due to the RHS operator of the fourth order compact scheme being symmetric positive semi-definite. The reason we came to this conclusion is our inability to apply the energy based stability argument outlined in [18]. The stability argument applied to the fourth order compact scheme defines a weighted inner product with the inverse of the RHS operator from the fourth order compact scheme. Since the RHS operator was positive symmetric positive semi-definite, its smallest eigenvalue is zero. In order to fix this instability we modified our scheme so that the energy based stability argument could apply. When we made our modification, the RHS operator would be symmetric positive definite, so the stability argument could apply. In [118, 119] they derive a family of fourth order compact scheme to approximate a more general class of wave equations in \mathbb{R}^n and run into a similar problem where the minimum eigenvalue of certain difference operator (in space) vanishes when the scheme takes place in \mathbb{R}^3 . They resolved their issue by replacing this degenerate difference operator with a similar difference operator which had more favorable spectral properties. In fact [119] compares their fourth order compact scheme (under simplifying assumption) to our eventual "Canonical Equation Based Scheme" derived in [96]. They conclude that their LHS operator ends up being the same (up to scalar multiplication) as ours while their RHS operator uses a smaller stencil than our RHS operator. We suspect that the same degenerate behavior was

being observed in both cases. We will modify our EBFOCS by incorporating some additional terms to improve the spectral properties of the final scheme.

Applying the differential operator $\frac{\partial^4}{\partial x^2 \partial y^2} + \frac{\partial^4}{\partial x^2 \partial z^2} + \frac{\partial^4}{\partial y^2 \partial z^2}$ to (2.10) and combining like terms produces

$$\begin{aligned} & \frac{\partial^6 u}{\partial x^4 \partial y^2} + \frac{\partial^6 u}{\partial x^2 \partial y^4} + \frac{\partial^6 u}{\partial x^4 \partial z^2} + \frac{\partial^6 u}{\partial x^2 \partial z^4} + \frac{\partial^6 u}{\partial y^4 \partial z^2} + \frac{\partial^6 u}{\partial y^2 \partial z^4} + 3 \frac{\partial^6 u}{\partial x^2 \partial y^2 \partial z^2} \\ & - \left(\frac{\partial^4}{\partial x^2 \partial y^2} + \frac{\partial^4}{\partial x^2 \partial z^2} + \frac{\partial^4}{\partial y^2 \partial z^2} \right) (\kappa^2 u) = \left(\frac{\partial^4}{\partial x^2 \partial y^2} + \frac{\partial^4}{\partial x^2 \partial z^2} + \frac{\partial^4}{\partial y^2 \partial z^2} \right) f. \end{aligned} \quad (2.17)$$

Taylor formula yields:

$$\Delta(\kappa^2 u) = \Delta_h(\kappa^2 u) - \frac{h^2}{12} \left(\frac{\partial^4}{\partial x^4} + \frac{\partial^4}{\partial y^4} + \frac{\partial^4}{\partial z^4} \right) (\kappa^2 u) + \mathcal{O}(h^4), \quad (2.18)$$

and

$$\begin{aligned} & \frac{\partial^4 u}{\partial x^2 \partial y^2} + \frac{\partial^4 u}{\partial x^2 \partial z^2} + \frac{\partial^4 u}{\partial y^2 \partial z^2} = \mathcal{A}_h u - \frac{h^2}{12} \left(\frac{\partial^6 u}{\partial x^4 \partial y^2} + \frac{\partial^6 u}{\partial x^2 \partial y^4} + \frac{\partial^6 u}{\partial x^4 \partial z^2} \right. \\ & \left. + \frac{\partial^6 u}{\partial x^2 \partial z^4} + \frac{\partial^6 u}{\partial y^4 \partial z^2} + \frac{\partial^6 u}{\partial y^2 \partial z^4} \right) + \mathcal{O}(h^4). \end{aligned} \quad (2.19)$$

Substituting (2.17) into (2.19), we have:

$$\begin{aligned} & \frac{\partial^4 u}{\partial x^2 \partial y^2} + \frac{\partial^4 u}{\partial x^2 \partial z^2} + \frac{\partial^4 u}{\partial y^2 \partial z^2} = \mathcal{A}_h u - \frac{h^2}{12} \left(\frac{\partial^4 f}{\partial x^2 \partial y^2} + \frac{\partial^4 f}{\partial x^2 \partial z^2} + \frac{\partial^4 f}{\partial y^2 \partial z^2} \right) \\ & - \frac{h^2}{12} \left(\frac{\partial^4}{\partial x^2 \partial y^2} + \frac{\partial^4}{\partial x^2 \partial z^2} + \frac{\partial^4}{\partial y^2 \partial z^2} \right) (\kappa^2 u) - \frac{h^2}{4} \left(\frac{\partial^6 u}{\partial x^2 \partial y^2 \partial z^2} \right) + \mathcal{O}(h^4) \\ & = \mathcal{A}_h u - \frac{h^2}{12} \mathcal{A}_h(\kappa^2 u) - \frac{h^2}{12} \left(\frac{\partial^4 f}{\partial x^2 \partial y^2} + \frac{\partial^4 f}{\partial x^2 \partial z^2} + \frac{\partial^4 f}{\partial y^2 \partial z^2} \right) - \frac{h^2}{4} \left(\frac{\partial^6 u}{\partial x^2 \partial y^2 \partial z^2} \right) + \mathcal{O}(h^4). \end{aligned} \quad (2.20)$$

Combining (2.16), (2.18), and (2.20) with the modified Helmholtz equation (2.10) we

obtain:

$$\begin{aligned} & \Delta_h u + \frac{h^2}{6} \mathcal{A}_h u - \left[1 + \frac{h^2}{12} \Delta_h + \frac{h^4}{72} \mathcal{A}_h \right] (\kappa^2 u) \\ &= \left(1 + \frac{h^2}{12} \Delta + \frac{h^4}{72} \left(\frac{\partial^4}{\partial x^2 \partial y^2} + \frac{\partial^4}{\partial x^2 \partial z^2} + \frac{\partial^4}{\partial y^2 \partial z^2} \right) \right) f + R, \end{aligned} \quad (2.21)$$

where the remainder

$$\begin{aligned} R &= \frac{h^4}{360} \left(\frac{\partial^6 u}{\partial x^6} + \frac{\partial^6 u}{\partial y^6} + \frac{\partial^6 u}{\partial z^6} \right) - \frac{h^4}{144} \left(\frac{\partial^4}{\partial x^4} + \frac{\partial^4}{\partial y^4} + \frac{\partial^4}{\partial z^4} \right) (\kappa^2 u) \\ &\quad + \frac{h^4}{24} \frac{\partial^6 u}{\partial x^2 \partial y^2 \partial z^2} + \mathcal{O}(h^6). \end{aligned}$$

The $\sim \frac{h^4}{72}$ term on the right-hand side of (2.21) is incorporated into the EBFOCS to improve the spectral properties of the final FOCS. This additional term will result in a RHS operator that is symmetric positive definite. Applying the differential operator $\frac{\partial^4}{\partial v^4}$ for $v = \{x, y, z\}$ into (2.10) produces

$$\frac{\partial^6 u}{\partial x^2 \partial v^4} + \frac{\partial^6 u}{\partial y^2 \partial v^4} + \frac{\partial^6 u}{\partial z^2 \partial v^4} - \frac{\partial^4}{\partial v^4} (\kappa^2 u) = \frac{\partial^4 f}{\partial v^4}.$$

As a consequence

$$\begin{aligned} & f + \frac{h^2}{12} \Delta f + \frac{h^4}{72} \left(\frac{\partial^4 f}{\partial x^2 \partial y^2} + \frac{\partial^4 f}{\partial x^2 \partial z^2} + \frac{\partial^4 f}{\partial y^2 \partial z^2} \right) \\ &= f + \frac{h^2}{12} \Delta_h f + \frac{h^4}{72} \mathcal{A}_h f - \frac{h^4}{144} \left(\frac{\partial^4 f}{\partial x^4} + \frac{\partial^4 f}{\partial y^4} + \frac{\partial^4 f}{\partial z^4} \right) + \mathcal{O}(h^6) \\ &= \left(1 + \frac{h^2}{12} \Delta_h + \frac{h^4}{72} \mathcal{A}_h \right) f - \frac{h^4}{144} \left(\frac{\partial^6 u}{\partial x^6} + \frac{\partial^6 u}{\partial y^6} + \frac{\partial^6 u}{\partial z^6} \right) + \frac{h^4}{144} \left(\frac{\partial^4}{\partial x^4} + \frac{\partial^4}{\partial y^4} + \frac{\partial^4}{\partial z^4} \right) (\kappa^2 u) \\ &\quad - \frac{h^4}{144} \left(\frac{\partial^6 u}{\partial x^2 \partial y^4} + \frac{\partial^6 u}{\partial x^4 \partial y^2} + \frac{\partial^6 u}{\partial x^2 \partial z^4} + \frac{\partial^6 u}{\partial x^4 \partial z^2} + \frac{\partial^6 u}{\partial y^2 \partial z^4} + \frac{\partial^6 u}{\partial y^4 \partial z^2} \right) + \mathcal{O}(h^6). \end{aligned} \quad (2.22)$$

Combining (2.21) and (2.22), we have:

$$\Delta_h u + \frac{h^2}{6} \mathcal{A}_h u - \left[1 + \frac{h^2}{12} \Delta_h + \frac{h^4}{72} \mathcal{A}_h \right] (\kappa^2 u) = \left(1 + \frac{h^2}{12} \Delta_h + \frac{h^4}{72} \mathcal{A}_h \right) f + \mathcal{O}(h^4). \quad (2.23)$$

Finally, rescaling (2.23) by a factor of h^2 , dropping the error term, and replacing the

difference operators with (2.13), yields the EBFOCS:

$$\mathbf{L}_h[\kappa^2]u = h^2 \mathbf{R}_h f = f_R, \quad (2.24)$$

where the LHS operator

$$\mathbf{L}_h[\kappa^2] \stackrel{\text{def}}{=} -4u_{i,j,k} + \frac{u_{ss}}{3} + \frac{u_{sc}}{6} - h^2 \left(\frac{2}{3}(\kappa^2 u)_{i,j,k} + \frac{(\kappa^2 u)_{ss}}{36} + \frac{(\kappa^2 u)_{sc}}{72} \right), \quad (2.25)$$

and the RHS operator

$$\mathbf{R}_h f \stackrel{\text{def}}{=} \left(\frac{2}{3}f_{i,j,k} + \frac{f_{ss}}{36} + \frac{f_{sc}}{72} \right). \quad (2.26)$$

We will refer to (2.24) as the discrete Modified Helmholtz equation (DMHE). Now that we have finally discretized the MHE (2.10) with fourth order accuracy in space we have the capacity to advance the time marching scheme.

Remark: Parallel Pointwise Smoother Since the LHS operator (2.24) doesn't contain any of the corner points of the $3 \times 3 \times 3$ stencil, the scheme is four colorable [114]. In other words consider the four non-overlapping grid sets labeled red, black, yellow, and green given by

$$\begin{aligned} D_{h,R}^0 &= \{(x_i, y_j, z_k) \in D_h^0 \mid i, j, k \text{ are all odd or all even} \}, \\ D_{h,B}^0 &= \{(x_i, y_j, z_k) \in D_h^0 \mid i, k \text{ are both odd/even and } j \text{ even/odd} \}, \\ D_{h,Y}^0 &= \{(x_i, y_j, z_k) \in D_h^0 \mid j, k \text{ are both odd/even and } i \text{ even/odd} \}, \\ D_{h,G}^0 &= \{(x_i, y_j, z_k) \in D_h^0 \mid i, j \text{ are both odd/even and } k \text{ even/odd} \}, \end{aligned}$$

and depicted in Figure 2.2. The non-overlapping grid sets satisfy

$$D_h^0 = D_{h,R}^0 \cup D_{h,B}^0 \cup D_{h,Y}^0 \cup D_{h,G}^0.$$

Given the grid point $(x_i, y_j, z_k) \in D_{h,A}^0$ for any $A \in \{R, B, Y, G\}$, none of the 18 surrounding grid points (side corner and side side nodes shown in Figure 2.1) which define the LHS operator (2.24) will be contained in $D_{h,A}^0$. That means if we apply a pointwise smoother, we can update every node in $D_{h,R}^0$, then update the nodes in $D_{h,B}^0$, then update the nodes in $D_{h,Y}^0$, then update the nodes in $D_{h,G}^0$ or any other order we wish. We can use parallel computing to divide up the nodes of $D_{h,A}^0$ for each

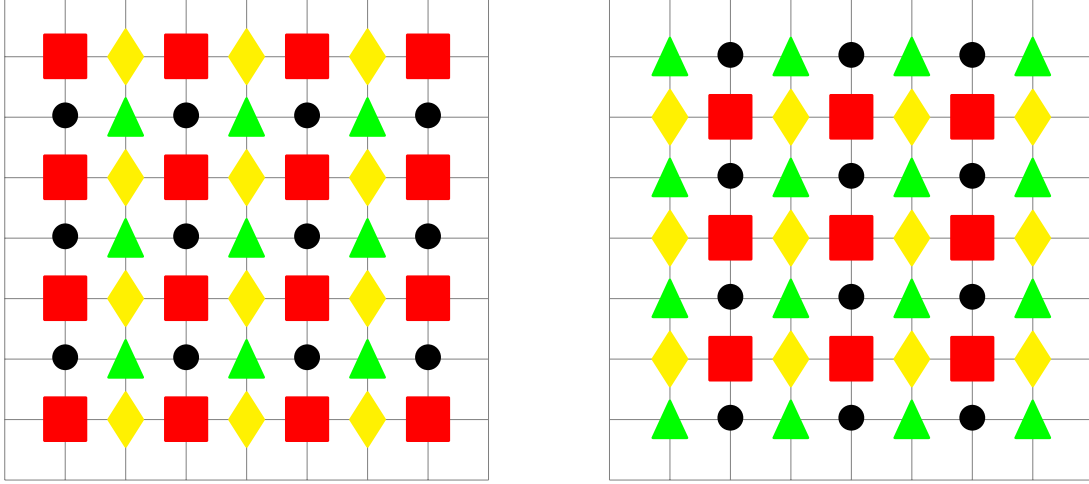


Figure 2.2: A four coloring of the grid set D_h^0 . The left/right grids indicate when the z-plane is oddly/evenly indexed.

$A \in \{R, B, Y, G\}$ to several processors to speed up the smoothing in each grid set. Even though multigrid is a sequential algorithm, parallel computing can speed up the smoother which is the most expensive component of the multigrid method. For a more complete description of multigrid methods with parallel computing [100][Chapter 6].

Remark: Parallel Blockwise Smoothing Instead of updating each grid point one at a time, suppose we wanted to solve for all the grid points $u_{i,j,k}$ where k is given and $1 \leq i, j, \leq N$ simultaneously using Gauss-Seidel as a smoother. Assuming lexicographic ordering, the resulting $N^2 \times N^2$ linear system will be a block tridiagonal system where each subordinate matrix is tridiagonal since our scheme is a compact $3 \times 3 \times 3$ stencil in space. Given the index $1 \leq k \leq N$, this matrix would produce a block tridiagonal system of the form

$$A_{j-1,k} \vec{u}_{j-1,k} + B_{j,k} \vec{u}_{j,k} + C_{j,k} \vec{u}_{j+1,k} = \vec{g}_{j,k} \quad \text{for } 1 \leq j \leq N, \quad (2.27)$$

$\vec{u}_{j,k} = [u_{1,j,k} u_{2,j,k} \dots u_{N,j,k}]^T$, $\vec{g}_{j,k}$ is a block vector of RHS terms for the Gauss-Seidel smoother, and $A_{j,k}, B_{j,k}, C_{j,k} \in \mathbb{R}^{N \times N}$ are tridiagonal matrices where $A_{0,k} = 0 = C_{N+1,k}$ for $k = 1, 2, \dots, N$. The block system (2.27) can be solved fast with the divide and conquer algorithm known as block cyclic reduction or cyclic reduction shown in [52, 92, 99]. For parallel computing we would use zebra plane smoother when solving

the block systems (2.27). That means all the odd numbered planes will be updated before all the even numbered planes are updated. For a more complete description of multigrid methods with parallel computing [100][Chapter 6].

2.3 Stability Criteria

Let $\lambda = \lambda(\mathbf{x})$ denote the CFL number:

$$\lambda(\mathbf{x}) = \frac{c(\mathbf{x})\tau}{h},$$

where h is the uniform grid size in space and τ is the uniform grid size in time. We will show the energy based stability argument proven in [18].

Theorem 2.3.1. Suppose $\frac{1}{h^2}\mathbf{L}_h \approx \Delta$ and satisfies

- ◇ \mathbf{L}_h is negative definite, so there exists a real inner product (\cdot, \cdot) where $(-\mathbf{L}_h u, u) \geq 0$ and there exists two positive numbers $0 < L_{\text{lower}} < L_{\text{upper}}$ such that

$$0 < L_{\text{lower}}\|u\|^2 \leq (-\mathbf{L}_h u, u) \leq L_{\text{upper}}\|u\|^2,$$

where the norm $\|u\| = \sqrt{(u, u)}$.

- ◇ \mathbf{L}_h is self-adjoint, i.e. $(\mathbf{L}_h u, v) = (u, \mathbf{L}_h v)$.

Then discretizing the homogeneous wave equation $\frac{1}{c^2} \frac{\partial^2 u}{\partial t^2} = \Delta u$ in time with the θ -scheme and approximating the Laplacian with $\frac{1}{h^2}\mathbf{L}_h$ produces a scheme which is unconditionally stable if $\theta > \frac{1}{4}$ and conditionally stable when $0 \leq \theta \leq \frac{1}{4}$. In the later case the CFL number satisfies

$$\max_{\mathbf{x}} \lambda^2(\mathbf{x}) \leq \frac{1}{(\frac{1}{4} - \theta)L_{\text{upper}}}.$$

Proof. The θ -scheme applied to the homogeneous wave equation produces

$$\frac{u^{n+1} - 2u^n + u^{n-1}}{\tau^2 c^2} = \frac{\mathbf{L}_h}{h^2} \left(\theta(u^{n+1} - u^n) - \theta(u^n - u^{n-1}) + u^n \right). \quad (2.28)$$

Define the variable $v^{n+1} = u^{n+1} - u^n$ which satisfies

$$\begin{aligned} v^{n+1} - v^n &= u^{n+1} - 2u^n + u^{n-1}, \\ v^{n+1} + v^n &= u^{n+1} - u^{n-1}. \end{aligned}$$

Taking the inner product of $h^2(v^{n+1} + v^n)$ with (2.28) produces

$$\begin{aligned} \frac{h^2}{c^2\tau^2}(v^{n+1} - v^n, v^{n+1} + v^n) &= (\mathbf{L}_h u^n + \theta \mathbf{L}_h(v^{n+1} - v^n), v^{n+1} + v^n) \\ \frac{1}{\lambda^2}(\|v^{n+1}\|^2 - \|v^n\|^2) &= (\mathbf{L}_h u^n, v^{n+1} + v^n) + \theta(\mathbf{L}_h(v^{n+1} - v^n), v^{n+1} + v^n) \\ &= (\mathbf{L}_h u^n, v^{n+1} + v^n) + \theta(\mathbf{L}_h(v^{n+1}, v^{n+1}) - \mathbf{L}_h(v^n, v^n)), \end{aligned}$$

where we have used the self-adjoint property of \mathbf{L}_h to eliminate the cross terms. Rearranging the above

$$\frac{1}{\lambda^2}\|u^{n+1}\|^2 - \theta(\mathbf{L}_h v^{n+1}, v^{n+1}) = \frac{1}{\lambda^2}\|u^n\|^2 - \theta(\mathbf{L}_h v^n, v^n) + (\mathbf{L}_h u^n, v^{n+1} + v^n), \quad (2.29)$$

Substituting the identity

$$\begin{aligned} (\mathbf{L}_h u^n, v^{n+1} + v^n) - (\mathbf{L}_h u^n, u^{n+1} - u^{n-1}) &= \frac{(\mathbf{L}_h v^n, v^n)}{4} - \frac{(\mathbf{L}_h v^{n+1}, v^{n+1})}{4} \\ &\quad - \frac{(\mathbf{L}_h(u^n + u^{n-1}), u^n + u^{n-1})}{4} + \frac{(\mathbf{L}_h(u^n + u^{n+1}), u^n + u^{n+1})}{4}, \end{aligned}$$

into (2.29) and rearranging yields the non-increasing formula

$$E_{n+1} = E_n,$$

where the quantity

$$E_n = \frac{1}{\lambda^2}\|v^n\|^2 + \left(\frac{1}{4} - \theta\right) (\mathbf{L}_h v^n, v^n) - \frac{1}{4}(\mathbf{L}_h(u^n + u^{n-1}), u^n + u^{n-1}). \quad (2.30)$$

In the case where $\theta > \frac{1}{4}$, all the terms which define (2.30) are non-negative due to \mathbf{L}_h being negative definite. In this case, define E_n as the energy norm. Then energy conservation implies unconditional convergence. When $0 \leq \theta < \frac{1}{4}$, the assumption

$0 < L_{\text{lower}}\|u\|^2 \leq (-\mathbf{L}_h u, u) \leq L_{\text{upper}}\|u\|^2$ implies that

$$\begin{aligned} & \left(\frac{1}{\lambda^2} - \left(\frac{1}{4} - \theta \right) L_{\text{upper}} \right) \|v^n\|^2 + \frac{L_{\text{lower}}}{4} \|u^n + u^{n-1}\|^2 \leq E_n \leq \\ & \left(\frac{1}{\lambda^2} - \left(\frac{1}{4} - \theta \right) L_{\text{lower}} \right) \|v^n\|^2 + \frac{L_{\text{upper}}}{4} \|u^n + u^{n-1}\|^2. \end{aligned}$$

Therefore E_n is equivalent to $\|u^n - u^{n-1}\|^2 + \|u^n + u^{n-1}\|^2$ which is equivalent to $\|u^n\|^2 + \|u^{n-1}\|^2$ if and only if $\frac{1}{\lambda^2} - \left(\frac{1}{4} - \theta \right) L_{\text{upper}} \geq 0$. Taking the supremum of the above over all \mathbf{x} completes the proof. \square

Now we want to adapt Theorem 2.3.1 to our fourth order compact scheme. Recall that the parameter $\theta = \frac{1}{12}$ produces the fourth order accurate discretization in time and the discrete modified Helmholtz equation with (2.24) with $\kappa^2 = 0$ discretizes the Laplacian with fourth order accuracy in space. According to Theorem 2.3.1, the CFL number of (2.24) satisfies

$$\max_{\mathbf{x} \in D} \lambda^2(\mathbf{x}) \leq \frac{6}{L_{\text{upper}}}.$$

All that's left to do is compute the quantity L_{upper} . First we will assume the speed in the acoustic wave equation is constant. To apply Theorem 2.3.1 define the weighted inner product $(u, v)_{\mathbf{R}} = (\mathbf{R}_h^{-1} u, v)$ since the matrix form of the RHS operator (2.26) is symmetric positive definite. To estimate L_{upper} take the Fourier transform (in space) and apply the Parseval equality to conduct the analysis in the frequency domain. Negating the Fourier Transform of the discrete Laplacian $\mathbf{R}_h^{-1} \mathbf{L}_h[0] \approx \Delta$ (i.e. apply the Fourier Transform to (2.24) with $\kappa^2 = 0$, then divide by the coefficient of the RHS operator, then negate) yields

$$-\mathbb{L}(\xi, \eta, \zeta) = \frac{4 - \frac{1}{3}X(\xi, \eta, \zeta) - \frac{1}{6}Y(\xi, \eta, \zeta)}{\frac{2}{3} + \frac{1}{36}X(\xi, \eta, \zeta) + \frac{1}{72}Y(\xi, \eta, \zeta)}, \quad (2.31)$$

where $(\xi, \eta, \zeta) \in [-\pi, \pi]^3$ and

$$\begin{aligned} X(\xi, \eta, \zeta) &= \cos(\xi) + \cos(\eta) + \cos(\zeta), \\ Y(\xi, \eta, \zeta) &= \cos(\xi) \cos(\eta) + \cos(\xi) \cos(\zeta) + \cos(\eta) \cos(\zeta). \end{aligned}$$

Using the built-in function `Maximize` of Mathematica on (2.31) over the domain $[-\pi, \pi]^3$ produces

$$L_{\text{upper}} = \max_{(\xi, \eta, \zeta) \in [-\pi, \pi]^3} |\mathbb{L}| = \frac{48}{5}.$$

As a consequence the CFL number of the fourth order compact scheme satisfies

$$\max_x \lambda(\mathbf{x}) \leq \sqrt{\frac{5}{8}}. \quad (2.32)$$

2.4 Full Time Marching Scheme

In this section we will explicitly depict the algorithm for solving the time marching scheme for the acoustic wave equation (2.1). Accordingly, the time marching scheme amounts to solving the discrete elliptic PDE

$$\begin{aligned} \mathbf{L}_h[\kappa^2]u^{n+1} &= f_R^{n+1} = \left(2 - \frac{1}{\theta}\right) f_R^n - f_R^{n-1} - h^2 \mathbf{R}_h \left(\frac{\kappa^2(\mathbf{x})u^n}{\theta} + \tilde{F}^{n+1} \right), \quad \text{in } D_h^0, \\ u^{n+1} &= 0, \quad \text{on } \partial D_h \cap \partial D, \end{aligned} \quad (2.33)$$

where the LHS operator \mathbf{L}_h is defined in (2.25) and the RHS operator \mathbf{R}_h is defined in (2.26). The algorithm for the time marching scheme depicts the preprocessing phase of Algorithm 5 depicts the preprocessing phase of the time marching scheme. Algorithm 6 depicts how the FOCS is initialized. Algorithm 7 shows how to advance the FOCS on the given upper time level.

2.5 Multigrid Convergence Rate

From our previous discussion in Sections 2.1 - 2.4, we know advancing the time marching scheme amounts to solving an elliptic PDE at every step. This is easily the most expensive portion of our time marching scheme. Therefore we want to solve the elliptic PDE as efficiently as possible. Since the coefficients of our elliptic PDE may vary in space, multigrid methods are the fastest available methods for solving an elliptic PDE. We will demonstrate that our multigrid method achieves the optimal

Algorithm 5 Preprocessing phase of the full time marching scheme for solving (2.1).

- 1: **function** PREPROCESSINGFOCS($\bar{x}_l, \bar{x}_r, \ell, c_{\max}$)
 - 2: $N = 2^\ell - 1, h = (\bar{x}_r - \bar{x}_l)/N+1$, and $\tau = h\sqrt{5}/8/c_{\max}$
 - 3: **for** $i = 1$ to ℓ **do**
 - 4: $N_i = 2^{\ell+1-i} - 1$ and $h_i = (\bar{x}_r - \bar{x}_l)/N_i+1$
 - 5: **if** $i = 1$ **then**
 - 6: allocate space for seven grid function on D_h .
 - 7: precompute coefficients of $L_h[\kappa^2]$ and R_h (2.24).
 - 8: **else**
 - 9: allocate space for three grid functions on D_{h_i} (2.11)
 - 10: precompute coefficients of $L_{h_i}[\kappa^2]$ (2.24).
 - 11: Store all the above in the multigrid data structure \mathcal{M} .
-

Algorithm 6 Initialization phase the full time marching scheme for solving (2.1).

- 1: **function** INITIALIZEFOCS(h, τ, L_h)
 - 2: For each $\mathbf{x}_h \in D_h^0$ compute u^0 with the initial data of (2.1).
 - 3: For each $\mathbf{x}_h \in D_h^0$ compute u^1 using the Taylor expansion (C.1).
 - 4: For each $\mathbf{x}_h \in D_h^0$ compute the terms $f_R^i = L_h[\kappa^2]u^i$ for $i \in \{0, 1\}$.
-

Algorithm 7 Advancement portion of the full time marching scheme for solving (2.1).

- 1: **function** ADVANCEFOCS($h, \tau, t^{n+1}, T, \mathcal{M}$)
 - 2: For each $\mathbf{x}_h \in D_h^0$ compute $g^{n+1} = -\frac{144u^n}{\tau^2c^2} - \frac{1}{c^2}(F^{n+1} + 10F^n + F^{n-1})$.
 - 3: For each $\mathbf{x}_h \in D_h^0$ apply the RHS operator i.e. $g_R^{n+1} = h^2 R_h g^{n+1}$.
 - 4: Assemble the recursive RHS $f_R^{n+1} = -10f_R^n - f_R^{n-1} + g_R^{n+1}$ on D_h^0 .
 - 5: Compute $\tilde{u}^{n+1} = 2u^n - u^{n-1} + \tau^2(c^2(\mathbf{x})\Delta_h u^n + F^n)$.
 - 6: Solve DMHE with \mathcal{M} using \tilde{u}^{n+1} and f_R^{n+1} as the initial guess and RHS.
 - 7: **if** $t^{n+1} < T$ **then**
 - 8: $t^{n+1} = t^{n+1} + \tau$
 - 9: For every $\mathbf{x}_h \in D_h^0$ $u^{n-1} = u^n, u^n = u^{n+1}, f_R^{n-1} = f_R^n, f_R^n = f_R^{n+1}$
 - 10: **else**
 - 11: STOP the scheme.
-

convergence rate. Let M_h denote the multigrid operator i.e. the linear operator which contains the smoother, restriction operator, prolongation operator, direct solve on the coarsest grid, ... We loosely state that the multigrid method has an optimal rate of convergence if the spectral radius $\rho(M_h) \approx \frac{1}{10}$. In this section we will describe how to obtain sharp estimates for the spectral radius of the multigrid method. Given

the hierarchical construction of MGCYC (see Figure 1.1 for depictions of the V , F , or W cycles) directly computing the spectral radius is impractical. Instead we will explore two methods to estimate the multigrid convergence rate, then compare the results. In Section 2.5.1 we will describe how to approximate this convergence rate by looking at the error history after a large number of iterations. In Section 2.5.2 we'll estimate the multigrid convergence rate quantitatively using Local Fourier Analysis (LFA). In Section 2.5.3 we compare both estimates for the multigrid convergence rate of the discrete modified Helmholtz equation (2.24) and show for a small number of pre-smoothing and post-smoothing steps, the methods agree.

2.5.1 Empirically Derived Convergence Rates

A simple way to estimate the rate of multigrid convergence is to approximate the convergence factor $\hat{\rho} = \lim_{m \rightarrow \infty} \|r_h^{(m)}\| / \|r_h^{(m-1)}\|$, where $r_h^{(m)}$ is the residual $r_h^{(m)} = \mathbf{R}_h f - \frac{1}{h^2} \mathbf{L}_h[\kappa^2] v_h^{(m)}$, $v_h^{(m)}$ is the m^{th} approximate solution to the modified Helmholtz equation (2.33) and the LHS and RHS operators are defined in (2.25) and (2.26) respectively. To approximate this quantity we will compute the two quantities

$$q^{(m)} = \|r_h^{(m)}\| / \|r_h^{(m-1)}\|,$$

$$\hat{q}^{(m_0, m)} = \sqrt[m-m_0]{q^{(m_0+1)} \cdot q^{(m_0+2)} \dots q^{(m)}} = \sqrt[m-m_0]{\|r_h^{(m)}\| / \|r_h^{(m_0)}\|},$$

where m_0 and m are sufficiently large enough to observe the asymptotic rate of convergence.

2.5.2 Local Fourier Analysis

Local Fourier analysis (LFA) provides sharp estimates of the multigrid convergence rate for a large class of linear elliptic PDEs [12]. A detailed account of LFA can be found, e.g., in [14, 100].

Let ω denote the amplification factor of the Gauss-Seidel smoother \mathcal{S}_h applied to the EBFOCS 2.24. It depends on the frequency $\boldsymbol{\theta} = (\theta_1, \theta_2, \theta_3) \in [-\pi, \pi]^3$ on the grid and on the quantity $h^2 \kappa^2$. In the context of time marching scheme, κ^2 is inversely proportional to the square of the time step τ given in (2.6). Hence, the quantity $h^2 \kappa^2$ is inversely proportional to the CFL number ((2.32)) squared, as follows

from the discussion of stability in Section 2.3. In the case of a variable $\kappa^2 = \kappa^2(\mathbf{x})$, the amplification factor is introduced by freezing the coefficient $\kappa^2(\mathbf{x})$ and thus, in addition to $\boldsymbol{\theta}$, it depends on the location \mathbf{x} where the coefficient κ^2 is frozen.

The smoothing factor is defined as

$$\mu = \mu(h^2\kappa^2) = \max_{\boldsymbol{\theta} \in \Theta_H} |\omega(\boldsymbol{\theta}, h^2\kappa^2)|, \quad (2.34)$$

where $\Theta_H = [-\pi, \pi]^3 \setminus [-\frac{\pi}{2}, \frac{\pi}{2}]^3$ is the subset of high frequencies on the grid. In the simplest case of a constant κ^2 where μ of (2.34) does not depend on \mathbf{x} , the smoothing factor immediately provides an estimate of how slowly the high frequency modes on the grid may decay when damped by a smoother. This, in turn, allows one to estimate the multigrid convergence rate (Recall from Section 1.2.5 that the smoother damps the high frequency components of the error). For example, if we perform $V(\nu_1, \nu_2)$ cycles, then the error should be expected to decrease by a factor of $\mu^{\nu_1 + \nu_2}$ provided that $\nu_1 + \nu_2$ is small. In the case of a variable κ^2 where μ of (2.34) depends on the location \mathbf{x} at which $\kappa^2(\mathbf{x})$ is frozen, the slowest decay (i.e., the worst case scenario) corresponds to the maximum value of μ across all \mathbf{x} . For the Gauss-Seidel smoother applied to the EBFOCS((2.24).), this translates into $\mu = \mu(h^2\kappa_{\min}^2)$, where $\kappa_{\min}^2 = \min_{\mathbf{x}} \kappa^2(\mathbf{x})$. To obtain the amplification factor we will substitute a grid function of the form

$$\varphi(\boldsymbol{\theta}, \mathbf{x}) = e^{i\boldsymbol{\theta} \cdot \mathbf{x}/h} = e^{i\theta_1 x_i/h} e^{i\theta_2 y_j/h} e^{i\theta_3 z_k/h},$$

into the smoother. We were unable to find an explicit formulas for this amplification factor over the set Θ_H . Instead we fixed the value κ^2 and approximated the smoothing factor numerically. In [96][Fig. 5] we plot the smoothing factor as a function of $h^2\kappa^2$. Generally speaking LFA is an asymptotic estimate. As a consequence we would only expect the smoothing factor to agree with the multigrid convergence factor for a couple of digits of accuracy anyway. For more detail on implementing local Fourier analysis see [14, 100].

2.5.3 Validating Multigrid Convergence Rates

In this section we will estimate the multigrid convergence rates described in Sections 2.5.1 and 2.5.2. Consider the test problem

$$\begin{aligned} \Delta w - \kappa^2(\mathbf{x})w &= 0, & \mathbf{x} \in D &= \left[-\frac{\pi}{2}, \frac{\pi}{2}\right]^3, \\ w &= 0, & \text{on } \partial D, \end{aligned} \tag{2.35}$$

The MHE (2.35) is convenient because the solution is clearly $w = 0$. As a consequence we don't need to worry about $\|r_h^{(m)}\|$ stalling near machine precision for large values of m and m_0 . We feed an initial guess which is zero along the boundary and one otherwise. See Table 1.1 for the settings of our multigrid method.

Table 2.1 compares the estimated convergence rates for various wavenumbers κ^2 . We chose $\kappa^2 = 0$ to get the worst case estimate for the rate of convergence, $\kappa^2 = 10^3 + 50 \sin(x^2 + y^2 + z^2)$ to see how a wavenumber with large maximum and minimum values affects the rate of convergence, and $5000 \cdot \exp\left(\frac{8}{\pi^2}(x + \frac{\pi}{2})^2\right)$ to see how a wavenumber with small minimum and large maximum affects the rate of convergence. When the total number of smoothing steps $\nu_1 + \nu_2 \leq 2$, then both estimates for the convergence rate agree (albeit roughly). When $\nu_1 + \nu_2 = 3$, the convergence rate predicted by LFA are somewhat optimistic. However, when the total number of smoothing steps exceeds three, the convergence rate predicted by LFA are much too optimistic. This makes sense because the LFA predicts the rate at which the high frequency components of the error decays. The smoother damps the high frequency components of the error, while having negligible effects on the low frequency components of the error. Once the high frequency components of the error are damped, there's no added benefit to additional applications of the smoother. Instead, it's better to proceed with coarse grid correction. Based on the results shown in Table (2.1) we recommend using $V(1,1), F(0,1), F(1,1), W(0,1),$ or $W(1,1)$ cycles if we want to use the convergence rates predicted by LFA.

Table 2.1: Comparison of empirically derived convergence factors versus the smoothing factor predicted by LFA and the empirically derived convergence factor using (2.35) as a test problem. We employ $V(\nu_1, \nu_2)$ cycles with a step size of $h = \frac{\pi}{256}$.

$\kappa^2(x, y, z)$	(ν_1, ν_2)	$\mu(h^2 \kappa_{min}^2)^{\nu_1 + \nu_2}$	$q^{(50)}$	$\hat{q}^{(10,50)}$
0	(1, 1)	.1232	.1187	.1160
	(1, 2)	.0433	.0556	.0520
	(2, 2)	.0152	.0370	.0370
$10^3 + 50 \sin(x^2 + y^2 + z^2)$	(1, 1)	.1120	.1082	.1008
	(1, 2)	.0375	.0502	.0479
	(2, 2)	.0125	.0258	.0257
$5000 \cdot \exp\left(\frac{8}{\pi^2}\left(x + \frac{\pi}{2}\right)^2\right)$	(1, 1)	.0770	.0859	.0780
	(1, 2)	.0214	.0556	.0520
	(2, 2)	.0059	.0370	.0370

2.6 Numerical Simulations

In this section we show the EBFOCS is fourth order accurate overall. We will measure the error of our scheme using the infinity norm

$$\|u - u_h\|_\infty = \max_n \max_{(x_i, y_j, z_k) \in D_h^0} |u(x_i, y_j, z_k, t^n) - u_h(x_i, y_j, z_k, t^n)|,$$

where u is the smooth solution to the acoustic wave equation (2.1) and u_h is the approximate solution from the EBFOCS using a uniform step size of h and a uniform time step of τ . The rate of convergence is measured by recording the quotient

$$\text{rate} = \log\left(\frac{\|u - u_{2h}\|_\infty}{\|u - u_h\|_\infty}\right) / \log(2). \quad (2.36)$$

If our scheme is correct the quotient (2.36) should approach four as we refine the grid. The following test problems will be used to solve the acoustic wave equation (2.1):

Example 1 Consider the constant speed wave equation

$$\frac{\partial^2 u}{\partial t^2} - c^2 \Delta u = 0, \quad (x, y, z) \in [-2, 2]^3, \quad 0 \leq t \leq 2, \quad (2.37)$$

with $c(x, y, z) = 1$, generated by the test solution

$$u(x, y, z, t) = \sin(2\pi x) \sin(\pi y) \sin(3\pi z) \cos(t\pi\sqrt{14}).$$

The initial data $u(x, y, z, 0) = \sin(2\pi x) \sin(\pi y) \sin(3\pi z)$ and $\frac{\partial u}{\partial t}(x, y, z, 0) = 0$. Please see Table 1.1 for the specific settings for our multigrid method.

Example 2 Consider the variable speed wave equation

$$\frac{\partial^2 u}{\partial t^2} - c^2 \Delta u = F, \quad (x, y, z) \in [-2, 2]^3, \quad 0 \leq t \leq 2, \quad (2.38)$$

where the speed $c(x, y, z) = \exp(-2(x^2 + y^2 + z^2)) \cos(2\pi(-x + y - z))^2$. The source term $F(x, y, z, t)$ is generated by substituting the test solution

$$u(x, y, z, t) = \sin 2\pi x \sin \pi y \sin 3\pi z \cos t,$$

into the LHS portion of the above. Differentiate the above with respect to t and evaluate at zero to obtain the initial conditions. Please see Table 1.1 for the specific settings for our multigrid method.

Example 3 Consider the variable speed wave equation

$$\frac{\partial^2 u}{\partial t^2} - c^2 \Delta u = F, \quad (x, y, z) \in [-2, 2]^3, \quad 0 \leq t \leq 2, \quad (2.39)$$

where the speed $c(x, y, z) = 1/2 + \cos^2(x) \cos^2(y) \cos^2(z)$. The source term $F(x, y, z, t)$ is generated by substituting the test solution

$$u(x, y, z, t) = 2 \sin \pi x \sin \pi y \sin \pi z \exp(-t^2/5),$$

into the above. Differentiate the above with respect to t and evaluate at zero to obtain the initial conditions. Please see Table 1.1 for the specific settings for our multigrid method.

Example 4 Consider the variable speed wave equation

$$\frac{\partial^2 u}{\partial t^2} - c^2 \Delta u = F, \quad (x, y, z) \in [-2, 2]^3, \quad 0 \leq t \leq 2, \quad (2.40)$$

where the speed $c(x, y, z) = 1 + \frac{x^2}{8}$. The source $F(x, y, z, t)$ is generated by substituting the test solution $u(x, y, z, t) = 5 \sin \pi x \sin \pi y \sin \pi z \cos(t - y)$ into the above. Differentiate the above with respect to t and evaluate at zero to obtain the initial conditions. Please see Table 1.1 for the specific settings for our multigrid method.

Tables 2.2, 2.3, 2.4, and 2.5 each demonstrate fourth order accuracy for the test problems (2.37) - (2.40) respectively since the convergence rate (2.36) approaches 4.00 as the grid is refined. Notice how the mean number of multigrid cycles needed to reach the prescribed termination criteria decreases as we refine the grid. We attribute this to our termination criteria being fixed for all grids and (2.9) providing an initial guess in a neighborhood of the solution on the upper time level. Since the error of this the initial guess is $\mathcal{O}(\tau^2 h^2 + \tau^4)$, refining the grid only improves the initial guess. Since the multigrid convergence rate is independent of the step size (see Section 2.5 for a description of this quantity) we reach the termination criteria in fewer steps on average as we refine the grid. Also notice that the runtime per multigrid cycle increases by a factor of 10 as the grid is refined.

Table 2.2: Grid refinement analysis for the test problem (2.37) when the time step τ is 95% of the maximum CFL shown in (2.32).

h	error	rate	mean # V(1,1)-cycles	CPUTIME (sec.)/V(1,1)-cycle
1/8	9.320e-02	—	4.050	0.019
1/16	5.873e-03	3.988	4.439	0.169
1/32	3.992e-04	3.879	3.988	1.770
1/64	2.499e-05	3.998	3.870	14.406
1/128	1.564e-06	3.998	2.991	139.65

Table 2.3: Grid refinement analysis for the test problem (2.38) when the time step τ is 95% of the maximum CFL shown in (2.32).

h	error	rate	mean # V(1,1)-cycles	CPUTIME (sec.)/V(1,1)-cycle
1/8	3.181e-02	—	4.950	0.0196
1/16	1.893e-03	4.071	5.00	0.181
1/32	1.169e-04	4.017	4.857	1.820
1/64	7.280e-06	4.006	3.994	16.995
1/128	4.547e-07	4.000	3.902	138.405

Table 2.4: Grid refinement analysis for the test problem (2.39) when the time step τ is 95% of the maximum CFL shown in (2.32).

h	error	rate	mean # V(1,1)-cycles	CPUTIME (sec.)/V(1,1)-cycle
1/8	4.384e-03	—	6.467	0.026
1/16	2.725e-04	4.007	6.000	0.196
1/32	1.702e-05	4.001	5.929	1.769
1/64	1.066e-06	3.998	5.000	16.248
1/128	6.644e-08	4.003	4.000	137.537

Table 2.5: Grid refinement analysis for the test problem (2.40) when the time step τ is 95% of the maximum CFL shown in (2.32).

h	error	rate	mean # V(1,1)-cycles	CPUTIME (sec.)/V(1,1)-cycle
1/8	8.054e-03	—	6.000	0.019
1/16	4.965e-04	4.020	6.000	0.193
1/32	3.108e-05	3.998	5.000	1.856
1/64	1.940e-06	4.001	5.000	15.625
1/128	1.212e-07	4.000	4.000	135.678

Chapter 3

INTERIOR PROBLEM

In this chapter, we discretize the interior problem (1.2) with fourth order accuracy in time and space using the method of difference potentials [88]. In Section 3.1, we show the semi-discrete approximation of (1.2) in time using the θ -scheme [23, 68]. This yields a one parameter family of elliptic PDEs which need to be solved at every step. The resulting elliptic PDEs are the same as (2.10), with the exception of replacing the cubic domain D with a curvilinear domain Ω , making it more challenging to solve at every time step. In Section 3.2, we use the method of difference potentials to solve the aforementioned elliptic PDEs. Recall from Section 1.2.4 that, if $Lu = f$ is an elliptic PDE on Ω , then the pair $\xi_\Gamma = (\xi_0, \xi_1)$ satisfies the inhomogeneous BEP (1.14) if and only if $\xi_\Gamma = \mathbf{Tr}u$. We will discuss the discrete counterparts to the projection and the trace and how they help obtain the finite difference solution on Ω . In Section 3.3, we show several numerical simulations to corroborate that (1.2) can be solved with fourth order accuracy subject to Dirichlet, Neumann, or Robin boundary conditions on a spherical domain.

3.1 Semi-Discrete Approximation in Time

Consider the interior problem (1.2). For any given $\mathbf{x} \in \Omega$ and time $t = t^n$, the θ -scheme [23, 68] produces the modified Helmholtz Equation (MHE)

$$\begin{aligned} \Delta u^{n+1} - \kappa^2(\mathbf{x})u^{n+1} &= f^{n+1}, & \mathbf{x} \in \Omega, \\ \mathbf{l}_\Gamma(u^{n+1}) &= \varphi_\Gamma^{n+1}, & \mathbf{x} \in \Gamma, \end{aligned} \tag{3.1}$$

where the “wavenumber” $\kappa^2(x)$ is defined in (2.6), the boundary condition $l_{\Gamma}(u^{n+1})$ is defined in (1.3), and the RHS is defined recursively in (2.8a) or (2.8b). For a complete description for how the modified Helmholtz equation (3.1) was derived, see Section 2.1.

Advancing the time marching scheme amounts to solving the elliptic boundary value problem (BVP) (3.1) at every time level where the RHS is assembled from known quantities from previous time levels. In Section 2.1, we discretized the acoustic wave equation (2.1) using a similar approach on a cubic domain with homogeneous boundary conditions. Because of the simple geometry we could solve the modified Helmholtz equation efficiently with geometric multigrid. However, the BVP (3.1) for the modified Helmholtz equation which results from discretizing (1.2) has curvilinear geometry and a more general boundary condition. Our claim is that we can solve (3.1) efficiently with geometric multigrid on a cube with homogeneous boundary conditions despite having curvilinear geometry and a general boundary condition. The method of difference potentials is what facilitates this approach. In Section (3.2), we will adapt the MDP to solving (3.1).

3.2 Method of Difference Potentials (MDP)

The method of difference potentials [88] is a method for solving interior and exterior problems which combines the advantages of finite difference methods and boundary elements methods while avoiding some of the shortcomings inherent in both methods. For example, the method of difference potentials embeds the governing PDE, which may be formulated on a domain with curvilinear geometry, into a domain with simple geometry where finite difference methods flourish. The embedding helps reduce the governing PDE to an equivalent expression defined on the boundary of the domain, similar to boundary element methods. However, the method of difference potentials uses a difference potential which is constructed with the help of a finite difference scheme instead of a Green’s function. As a consequence the method of difference potentials applies to a wider class of problems since Green’s functions are only available for problems with constant coefficients. In addition, the method of difference potentials utilizes a spectral representation of the boundary condition to avoid differentiating near the boundary of the curvilinear domain altogether. For a complete description of method of difference potentials see the monograph [88].

For the remainder of the chapter, we will apply the method of difference potentials to solve (3.1). In Section 3.2.1, we describe the auxiliary problem and its discrete counterpart. We will construct an auxiliary problem whose domain contains the closure of Ω which can be solved using our fourth order compact scheme derived in Section 2.2. In Section 3.2.2, we describe the various grid sets needed to apply the method of difference potentials. In particular, we construct the discrete boundary γ , which consists of all the grid points which straddle the continuous boundary Γ . These grid sets are necessary to construct the discrete counterparts of the trace of the solution on Γ , the Calderón's potential, and the Calderón's projection. In Section 3.2.3, we introduce the discrete generalized Calderón-Seely Boundary Equation with Projection. This equation which is defined on the boundary of *Omega* is equivalent to the finite difference approximation of (3.1) on Ω . In Section 3.2.4, we discuss the extension operator, an affine operator which uses the spectral representation of the trace $\xi_\Gamma = (u, \frac{\partial u}{\partial n})|_\Gamma$ in order to obtain a grid function on γ that the discrete projection operates on. In Section 3.2.5, we present a solution algorithm for (3.1).

3.2.1 Auxiliary Problem (AP)

In this section, we will define the auxiliary problem (AP) needed to solve (3.1). The auxiliary problem must satisfy the following criteria:

- ◇ The PDE of the auxiliary problem must coincide with the PDE on Ω .
- ◇ The AP is to be formulated on a larger domain $\Omega^0 \supset \bar{\Omega}$ that has simple shape.
- ◇ The boundary condition on $\partial\Omega^0$ should guarantee existence and uniqueness of the solution to the AP and its well-posedness.
- ◇ The AP should admit an easy numerical solution.

In general, Ω^0 could be a rectangular prism, cylinder, sphere, or any other region that admits a regular grid. For our purposes we will only consider cubic domains for Ω^0 discretized with Cartesian grids. We will choose Ω^0 sufficiently large so that the nodes of γ which straddle Γ all belong to the interior of Ω^0 . In addition, we will only consider homogeneous boundary conditions on $\partial\Omega^0$. These choices are to remain consistent with our methodology in Chapter 2.

We will define the auxiliary problem for the generic MHE as

$$\begin{aligned}\Delta w^{n+1} - \kappa^2(\mathbf{x})w^{n+1} &= g^{n+1}, & \mathbf{x} \in \Omega^0, \\ w^{n+1} &= 0, & \mathbf{x} \in \Gamma^0 = \partial\Omega^0,\end{aligned}\tag{3.2}$$

where Ω^0 is a cube that contains Ω and g^{n+1} is an arbitrary right hand side function on the upper time level. It's of the utmost importance that the AP (3.2) be uniquely solvable for an arbitrary RHS g^{n+1} , not just the physical RHS f^{n+1} coming from the MHE (3.1). The discrete counterpart to the auxiliary problem (3.2) is given by

$$\begin{aligned}\mathbf{L}_h[\kappa^2]w^{n+1} &= g^{n+1}, & \mathbf{x}_h \in \Omega_h^0, \\ w^{n+1} &= 0, & \mathbf{x}_h \in \Gamma_h^0,\end{aligned}\tag{3.3}$$

where the LHS operator of the fourth order compact scheme is defined in (2.25). Let \mathbf{G}_h denote the solution operator (Green's operator) of the discrete auxiliary problem (DAP) (3.3). In other words,

$$w^{n+1} = \mathbf{G}_h g^{n+1},\tag{3.4}$$

is the unique solution to (3.3) for any given RHS g^{n+1} .

3.2.2 Grid Sets on the Auxiliary Domain

Prior to discussing the solution of (3.1) with the MDP, we will define several grid sets within the auxiliary domain. Given the grid point (x_i, y_j, z_k) , consider the neighboring nodes

$$\mathcal{N}_{i,j,k}^{18} = \{(x_{i+\bar{i}}, y_{j+\bar{j}}, z_{k+\bar{k}}) \mid (\bar{i}, \bar{j}, \bar{k}) \in \{-1, 0, 1\}^3 \text{ and } 1 \leq |\bar{i}| + |\bar{j}| + |\bar{k}| \leq 2\}\tag{3.5}$$

The set $\mathcal{N}_{i,j,k}^{18}$ of (3.5) consists of the $3 \times 3 \times 3$ stencil depicted in Figure 2.1 with the central and corner nodes removed.

Definition 3.2.1. Let Ω denote the domain of the elliptic PDE and Ω^0 denote the auxiliary domain, $\bar{\Omega} \subset \Omega^0$. Define the grid sets

$$\begin{aligned}\diamond \mathbf{N}^0 &= \{(x_i, y_j, z_k) \mid (x_i, y_j, z_k) \in \bar{\Omega}^0\} \\ \diamond \mathbf{M}^0 &= \{(x_i, y_j, z_k) \mid (x_i, y_j, z_k) \in \bar{\Omega}^0 \setminus \partial\Omega^0\}\end{aligned}$$

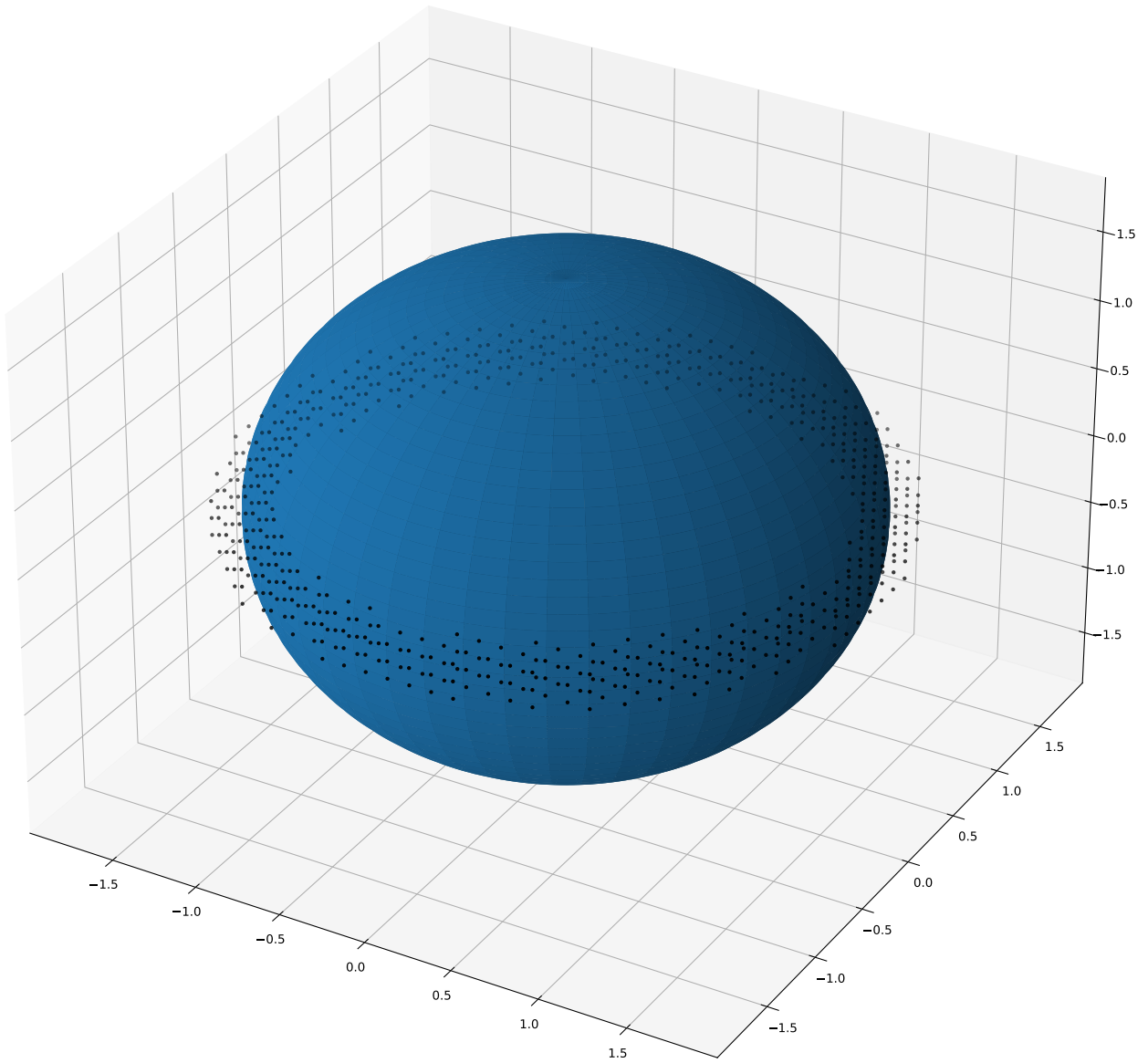


Figure 3.1: Subset of the discrete boundary γ when Ω is a ball of radius 1.65 centered at the origin.

- ◇ $\mathbb{M}^+ = \mathbb{M}^0 \cap \bar{\Omega}$
- ◇ $\mathbb{M}^- = \mathbb{M}^0 \cap (\Omega^0 \setminus \bar{\Omega})$
- ◇ $\mathbb{N}^\pm = \mathbb{M}^\pm \cup \{\cup \mathcal{N}_{i,j,k}^{18} \mid \forall (x_i, y_j, z_k) \in \mathbb{M}^\pm\}$
- ◇ $\gamma = \mathbb{N}^+ \cap \mathbb{N}^-$
- ◇ $\gamma_\pm = \mathbb{M}^\pm \cap \gamma$
- ◇ γ_{proj} is the orthogonal projection of $(x_i, y_j, z_k) \in \gamma$ onto the boundary Γ

\mathbb{N}^0 is a uniform Cartesian grid that discretizes the auxiliary domain Ω^0 . The grid set \mathbb{M}^0 consists of all the grid points which belong to \mathbb{N}^0 except those on the boundary $\partial\Omega^0$. The grid sets \mathbb{M}^\pm consist of the interior/exterior nodes with respect to $\bar{\Omega}$. As a convention, we assume that the nodes on Γ are included in \mathbb{M}^+ . The grid set \mathbb{M}^+ will serve as a discrete counterpart to the volume Ω when defining the discrete Calderón's potential analogous to (1.12). The grid sets \mathbb{N}^\pm are the unions of every interior/exterior grid node along with the adjacent nodes of the fourth order compact scheme. The most important grid set is γ , the discrete counterpart of Γ . We need this grid set to define the discrete Calderón's projection analogous to (1.13) and the inhomogeneous boundary equation with projection analogous to (1.14). We are always assuming that, the domain Ω^0 is sufficiently large to contain all nodes of the grid boundary γ . Figure 3.1 depicts a portion of the discrete boundary γ when Ω is a ball while Figure 3.2 depicts the orthogonal projection of γ onto Γ , namely γ_{proj} . We will use the projected points to establish the relationship between the trace of the solution on Γ to the trace of the solution on γ .

3.2.3 Discrete Generalized Calderón-Seely Projection

In this section, we will formulate the main Theorem needed to solve (3.1). Recall from Section 1.2.4 that, $\text{Tr}u^{n+1} = \boldsymbol{\zeta}^{n+1}$ where u^{n+1} is the solution (3.1) if and only if $\boldsymbol{\zeta}^{n+1}$ satisfies the inhomogeneous boundary equation with projection (1.14). Now that we have defined the various grid sets in Section 3.2.2, we can introduce the discrete counterpart to the above statement.

Definition 3.2.2. A density, w_γ , is a grid function defined on the grid boundary γ .

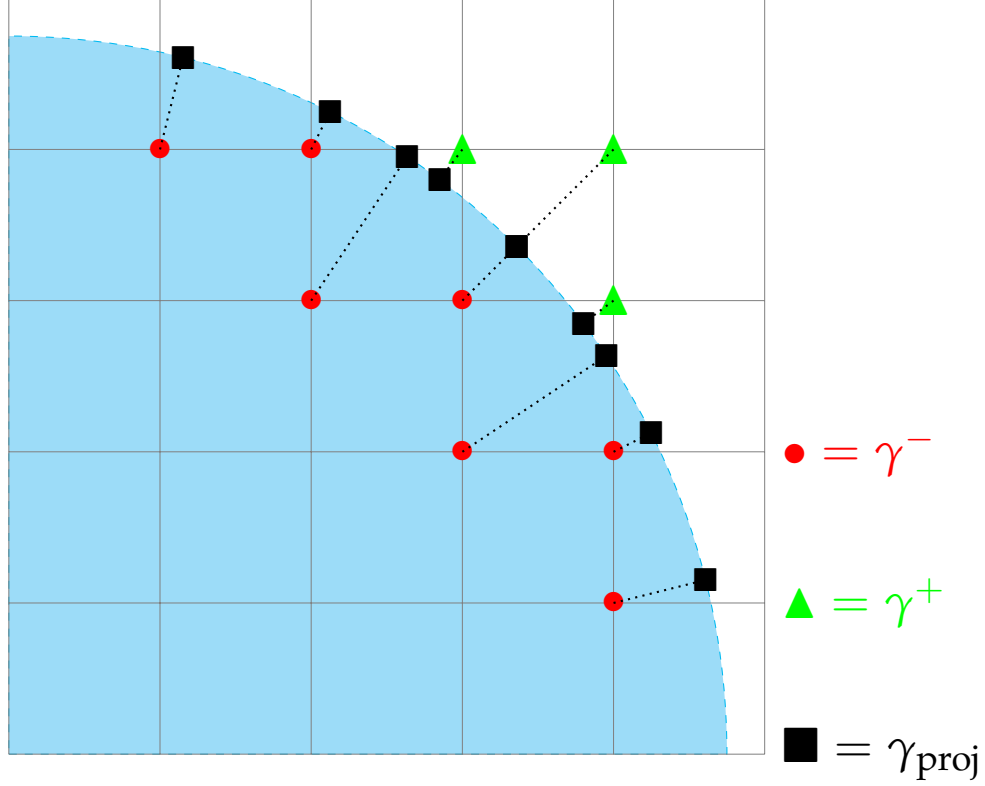


Figure 3.2: Example of the grid sets γ^- , γ^+ , and γ_{proj} which straddle the continuous boundary Γ . The discrete boundary $\gamma = \gamma_+ \cup \gamma_-$.

Definition 3.2.3. Let $w_{\mathbb{N}^0}$ be a grid function defined on \mathbb{N}^0 . The *trace* of $w_{\mathbb{N}^0}$ is the restriction of $w_{\mathbb{N}^0}$ to the discrete boundary γ . In other words, $\text{Tr}_\gamma w_{\mathbb{N}^0} \stackrel{\text{def}}{=} w_{\mathbb{N}^0}|_\gamma$.

Definitions 3.2.2 and 3.2.3 allow us to introduce the difference potential and difference projection which are the discrete counterparts of the Calderón's potential and Calderón's projection, respectively.

Definition 3.2.4. The *difference potential* with density v_γ (see Definition 3.2.2) is a grid function defined on \mathbb{N}^+ :

$$\mathbf{P}_{\mathbb{N}^+} v_\gamma = w_{\mathbb{N}^0} - \mathbf{G}_h[\mathbf{L}_h[\kappa^2]w_{\mathbb{N}^0}|_{\mathbb{M}^+}],$$

where $w_{\mathbb{N}^0}$ is an arbitrary grid function such that $\text{Tr}_\gamma w_{\mathbb{N}^0} = v_\gamma$. The *difference projection* is the trace of the potential: $\mathbf{P}_\gamma v_\gamma = \text{Tr}_\gamma \mathbf{P}_{\mathbb{N}^+} v_\gamma$.

The following Theorem uses the difference projection to define a discrete coun-

terpart of the inhomogeneous boundary equation with projection (1.14) and uses the difference potential to construct an approximate solution to (3.1).

Theorem 3.2.1 (Boundary Equation with Projection).

Consider the discrete modified Helmholtz equation

$$\mathbf{L}_h[\kappa^2]u_{\mathbb{N}^+}^{n+1} = \tilde{f}_R^{n+1}, \quad (3.6)$$

where the solution $u_{\mathbb{N}^+}^{n+1}$ is defined on \mathbb{N}^+ and the right-hand side \tilde{f}_R^{n+1} is defined on \mathbb{M}^+ . Then, the density u_γ^{n+1} coincides with the trace of a solution $u_{\mathbb{N}^+}^{n+1}$: $u_\gamma^{n+1} = \mathbf{Tr}_\gamma u_{\mathbb{N}^+}^{n+1}$, if and only if it satisfies the inhomogeneous BEP

$$u_\gamma^{n+1} = \mathbf{P}_\gamma u_\gamma^{n+1} + \mathbf{Tr}_\gamma \mathbf{G}_h \tilde{f}_R^{n+1}. \quad (3.7)$$

If equation (3.7) holds, the approximate solution $u_{\mathbb{N}^+}^{n+1}$ can be constructed using the generalized Green's formula:

$$u_{\mathbb{N}^+}^{n+1} = \mathbf{P}_{\mathbb{N}^+} u_\gamma^{n+1} + \mathbf{G}_h \tilde{f}_R^{n+1}|_{\mathbb{N}^+}. \quad (3.8)$$

To solve the modified Helmholtz equation (3.1) with the help of Theorem 3.2.1, we need to find the density u_γ^{n+1} which satisfies the inhomogeneous BEP (3.7), where the right-hand side of (3.6) is $\tilde{f}_R^{n+1} = h^2 \mathbf{R}_h f^{n+1}$ on \mathbb{M}^+ . Once the density is known, we can use the generalized Green's formula (3.8) to construct a discrete solution to (3.1) on \mathbb{N}^+ . In Section 3.2.4, we introduce the extension operator that relates the continuous density ξ_Γ (see Section 1.2.4) with the discrete density u_γ^{n+1} and in Section 3.2.5, we incorporate the extension operator into (3.7).

3.2.4 Extension Operator on a Sphere

In this section, we will show how to approximate the discrete density u_γ^{n+1} via ξ_Γ^{n+1} in the case where Ω is a ball. Substituting u_γ^{n+1} represented this way into the BEP (3.7), we can solve the resulting equation with respect to ξ_Γ^{n+1} . Once u_γ^{n+1} is known, we substitute it into the generalized Green's formula (3.8), obtaining the discrete solution to (3.1) on the grid \mathbb{N}^+ .

For every $x_h \in \gamma$, there exists an orthogonal projection onto the continuous boundary Γ , i.e., $\tilde{x}_h \in \gamma_{\text{proj}}$ (See Figure 3.2). We shall use Taylor's theorem about this projected point to approximate the density on the discrete boundary γ . The extension

operator on the ball is defined by

$$\mathbf{Ex}(\boldsymbol{\zeta}^{n+1}) \stackrel{\text{def}}{=} u^{n+1}|_{\tilde{x}_h} + \varrho \frac{\partial u^{n+1}}{\partial r}|_{\tilde{x}_h} + \sum_{i=2}^{I_{\text{Ex}}-1} \frac{\varrho^i}{i!} \frac{\partial^i u^{n+1}}{\partial r^i}|_{\tilde{x}_h} + O(\varrho^{I_{\text{Ex}}}), \quad (3.9)$$

where $\boldsymbol{\zeta}^{n+1} = \mathbf{Tr}(u^{n+1}, \frac{\partial u}{\partial r})$ and the signed distance from the continuous boundary Γ

$$\varrho = \begin{cases} |\mathbf{x}_h - \tilde{\mathbf{x}}_h|, & \text{if } \mathbf{x}_h \in \gamma^+ \\ -|\mathbf{x}_h - \tilde{\mathbf{x}}_h|, & \text{if } \mathbf{x}_h \in \gamma^- \end{cases},$$

We need to choose the order of the extension operator, I_{Ex} , sufficiently high to maintain fourth order accuracy overall. Of course, the accuracy of the extension operator may not be lower than that of the fourth order compact scheme. This implies $I_{\text{Ex}} \geq 4$, because $\varrho \leq Ch$, $C = \text{const} > 0$, where h is the grid size of the discrete AP. According to Reznik's Theorem [85, 86], a sixth order extension operator ($I_{\text{Ex}} = 6$) is sufficient to maintain fourth order accuracy overall when a second order PDE is discretized with fourth order accuracy. However, Reznik's Theorem isn't always necessary in practice. For example, the authors of [17] solve the two dimensional acoustic wave equation with the MDP using a fourth order compact scheme. They use a fourth order accurate extension operator in each of their simulations. This proved sufficient for Dirichlet boundary conditions, but insufficient for the Neumann boundary conditions since the scheme dropped to third order accuracy. Keeping this in mind, we will consider a fifth order accurate extension operator ($I_{\text{Ex}} = 5$).

We can use an equation based approach to eliminate the high order normal derivatives of (3.9). Since Ω is a ball, we will consider the acoustic wave equation in spherical coordinates and differentiate this formula to obtain expressions for the high order normal, i.e., radial, derivatives. The Laplacian in spherical coordinates is $\Delta w = \frac{\partial^2 w}{\partial r^2} + \frac{2}{r} \frac{\partial w}{\partial r} + \frac{\Delta_{\theta, \varphi} w}{r^2}$ where $\Delta_{\theta, \varphi}$ is the Laplace-Beltrami operator which contains the tangential derivatives on the sphere. Differentiating (1.2) in spherical coordinates with respect to the radial coordinate yields the high order derivatives

$$\frac{\partial^2 u}{\partial r^2} = - \left(\frac{2}{r} \frac{\partial u}{\partial r} + \frac{\Delta_{\theta, \varphi} u}{r^2} \right) + \frac{1}{c^2} \left(\frac{\partial^2 u}{\partial t^2} - F \right) \quad (3.10a)$$

$$\frac{\partial^3 u}{\partial r^3} = - \frac{2}{r} \frac{\partial^2 u}{\partial r^2} + \frac{2 - \Delta_{\theta, \varphi}}{r^2} \frac{\partial u}{\partial r} + \frac{2\Delta_{\theta, \varphi} u}{r^3} - \frac{2}{c^3} \frac{\partial c}{\partial r} \left(\frac{\partial^2 u}{\partial t^2} - F \right) + \frac{1}{c^2} \left(\frac{\partial^3 u}{\partial t^2 \partial r} - \frac{\partial F}{\partial r} \right) \quad (3.10b)$$

$$\begin{aligned} \frac{\partial^4 u}{\partial r^4} = & -\frac{2}{r} \frac{\partial^3 u}{\partial r^3} + \frac{4 - \Delta_{\theta,\varphi}}{r^2} \frac{\partial^2 u}{\partial r^2} + \frac{4\Delta_{\theta,\varphi} - 4}{r^3} \frac{\partial u}{\partial r} - \frac{6\Delta_{\theta,\varphi} u}{r^4} + \frac{1}{c^2} \left(\frac{\partial^4 u}{\partial t^2 \partial r^2} - \frac{\partial^2 F}{\partial r^2} \right) \\ & - \frac{4}{c^3} \frac{\partial c}{\partial r} \left(\frac{\partial^3 u}{\partial t^2 \partial r} - \frac{\partial F}{\partial r} \right) + \left(\frac{6}{c^4} \left(\frac{\partial c}{\partial r} \right)^2 - \frac{2}{c^3} \frac{\partial^2 c}{\partial r^2} \right) \left(\frac{\partial^2 u}{\partial t^2} - F \right). \end{aligned} \quad (3.10c)$$

Next, we want to eliminate all the high order unmixed normal derivatives of u which appear on the right hand side terms of (3.10a), (3.10b), and (3.10c). To illustrate our approach, consider the third order normal derivative. We will substitute the expression (3.10a) into (3.10b) and combine like terms. This new expression will only contain zeroth and first order unmixed normal derivatives of u as a result. Similarly, for the fourth order normal derivative we will substitute (3.10a) and (3.10b) into (3.10c) and combine like terms. The new expression will only contain zeroth and first order unmixed normal derivatives of u as a result. Then,

$$\frac{\partial^2 u}{\partial r^2} = - \left(\frac{2}{r} \frac{\partial u}{\partial r} + \frac{\Delta_{\theta,\varphi} u}{r^2} \right) + \frac{1}{c^2} \left(\frac{\partial^2 u}{\partial t^2} - F \right) \quad (3.11a)$$

$$\frac{\partial^3 u}{\partial r^3} = \frac{4\Delta_{\theta,\varphi} u}{r^3} + \frac{6 - \Delta_{\theta,\varphi}}{r^2} \frac{\partial u}{\partial r} - \left(\frac{2}{c^3} \frac{\partial c}{\partial r} + \frac{2}{c^2 r} \right) \left(\frac{\partial^2 u}{\partial t^2} - F \right) + \frac{1}{c^2} \left(\frac{\partial^3 u}{\partial t^2 \partial r} - \frac{\partial F}{\partial r} \right) \quad (3.11b)$$

$$\begin{aligned} \frac{\partial^4 u}{\partial r^4} = & \frac{\Delta_{\theta,\varphi}^2 - 18\Delta_{\theta,\varphi}}{r^4} u + \frac{8\Delta_{\theta,\varphi} - 24}{r^3} \frac{\partial u}{\partial r} + \left(\frac{8}{c^2 r^2} + \frac{4}{c^3 r} \frac{\partial c}{\partial r} + \frac{6}{c^4} \left(\frac{\partial c}{\partial r} \right)^2 - \frac{2}{c^3} \frac{\partial^2 c}{\partial r^2} \right) \left(\frac{\partial^2 u}{\partial t^2} - F \right) \\ & - \left(\frac{4}{c^3} \frac{\partial c}{\partial r} + \frac{2}{rc^2} \right) \left(\frac{\partial^3 u}{\partial t^2 \partial r} - \frac{\partial F}{\partial r} \right) + \frac{1}{c^2} \left(\frac{\partial^4 u}{\partial t^2 \partial r^2} - \frac{\partial^2 F}{\partial r^2} \right) - \Delta_{\theta,\varphi} \left(\frac{1}{c^2 r^2} \left(\frac{\partial^2 u}{\partial t^2} - F \right) \right). \end{aligned} \quad (3.11c)$$

Next we will eliminate the fourth order mixed derivative of u contained in (3.11c). Differentiating (3.11a) twice with respect to t yields

$$\frac{\partial^4 u}{\partial t^2 \partial r^2} = -\frac{\Delta_{\theta,\varphi}}{r^2} \frac{\partial^2 u}{\partial t^2} - \frac{2}{r} \frac{\partial^3 u}{\partial t^2 \partial r} + \frac{1}{c^2} \left(\frac{\partial^4 u}{\partial t^4} - \frac{\partial^2 F}{\partial t^2} \right). \quad (3.12a)$$

Substituting (3.12a) into (3.11a) produces the high order normal derivatives

$$\frac{\partial^2 u}{\partial r^2} = - \left(\frac{2}{r} \frac{\partial u}{\partial r} + \frac{\Delta_{\theta,\varphi} u}{r^2} \right) + \frac{1}{c^2} \left(\frac{\partial^2 u}{\partial t^2} - F \right) \quad (3.13a)$$

$$\frac{\partial^3 u}{\partial r^3} = \frac{4\Delta_{\theta,\varphi} u}{r^3} + \frac{6 - \Delta_{\theta,\varphi}}{r^2} \frac{\partial u}{\partial r} - \left(\frac{2}{c^3} \frac{\partial c}{\partial r} + \frac{2}{rc^2} \right) \left(\frac{\partial^2 u}{\partial t^2} - F \right) + \frac{1}{c^2} \left(\frac{\partial^3 u}{\partial t^2 \partial r} - \frac{\partial F}{\partial r} \right) \quad (3.13b)$$

Table 3.1: Contains the coefficients of the one sided difference schemes backwards in time for several derivatives using a uniform time step τ . Rescale the coefficients of the p^{th} order derivative by a factor of $1/\tau^p$.

Derivative	Accuracy	0	-1	-2	-3	-4	-5
2	1	1	-2	1			
	2	2	-5	4	-1		
	3	35/12	-104/12	114/12	-56/12	11/12	
	4	45/12	-154/12	214/12	-156/12	61/12	-10/12
4	1	1	-4	6	-4	1	
	2	3	-14	26	-24	11	-2

$$\begin{aligned}
\frac{\partial^4 u}{\partial r^4} &= \frac{\Delta_{\theta,\varphi}^2 - 18\Delta_{\theta,\varphi}}{r^4} u + \frac{8\Delta_{\theta,\varphi} - 24}{r^3} \frac{\partial u}{\partial r} + \left(\frac{8 - \Delta_{\theta,\varphi}}{c^2 r^2} + \frac{4\frac{\partial c}{\partial r}}{c^3 r} + \frac{6\left(\frac{\partial c}{\partial r}\right)^2}{c^4} - \frac{2\frac{\partial^2 c}{\partial r^2}}{c^3} \right) \frac{\partial^2 u}{\partial t^2} \\
&- \left(\frac{4\frac{\partial c}{\partial r}}{c^3} + \frac{4}{rc^2} \right) \frac{\partial^3 u}{\partial t^2 \partial r} - \Delta_{\theta,\varphi} \left(\frac{1}{c^2 r^2} \frac{\partial^2 u}{\partial t^2} \right) - \left(\frac{8}{c^2 r^2} + \frac{4\frac{\partial c}{\partial r}}{c^3 r} + \frac{6\left(\frac{\partial c}{\partial r}\right)^2}{c^4} - \frac{2\frac{\partial^2 c}{\partial r^2}}{c^3} \right) F \\
&+ \left(\frac{2}{c^2 r} + \frac{4\frac{\partial c}{\partial r}}{c^3} \right) \frac{\partial F}{\partial r} - \frac{1}{c^2} \frac{\partial^2 F}{\partial r^2} + \frac{1}{c^4} \left(\frac{\partial^4 u}{\partial t^4} - \frac{\partial^2 F}{\partial t^2} \right) + \Delta_{\theta,\varphi} \left(\frac{F}{c^2 r^2} \right). \tag{3.13c}
\end{aligned}$$

Notice that all the normal derivatives of u contained in (3.13a), (3.13b), and (3.13c) are either zeroth or first order. Next we will approximate the second order time derivatives of u contained in (3.13a) - (3.13c) on the upper time level.

Substituting the one sided difference formulas

$$\frac{\partial^{2+i} u^{n+1}}{\partial r^i \partial t^2} \approx d_i^{n+1} \frac{\partial^i u^{n+1}}{\partial r^i} + \sum_{k=0}^{J_i} d_i^{n-k} \frac{\partial^i u^{n-k}}{\partial r^i}, \quad \text{for } i \in \{0, 1\}, \tag{3.14a}$$

$$\frac{\partial^{4+i} u^{n+1}}{\partial r^i \partial t^4} \approx \tilde{d}_i^{n+1} \frac{\partial^i u^{n+1}}{\partial r^i} + \sum_{k=0}^{\tilde{J}_i} \tilde{d}_i^{n-k} \frac{\partial^i u^{n-k}}{\partial r^i}, \quad \text{for } i \in \{0, 1\}, \tag{3.14b}$$

whose coefficients are defined in Table 3.1 into (3.13a) - (3.13c) yields

$$\frac{\partial^2 u^{n+1}}{\partial r^2} \approx \left(\frac{d_0^{n+1}}{c^2} - \frac{\Delta_{\theta,\varphi}}{r^2} \right) u^{n+1} - \frac{2}{r} \frac{\partial u^{n+1}}{\partial r} + \frac{1}{c^2} \left(\sum_{j=0}^{J_0} d_0^{n-j} u^{n-j} - F^{n+1} \right) \quad (3.15a)$$

$$\begin{aligned} \frac{\partial^3 u^{n+1}}{\partial r^3} \approx & \left(-d_0^{n+1} \left(\frac{2}{c^2 r} + \frac{2}{c^3} \frac{\partial c}{\partial r} \right) + \frac{4\Delta_{\theta,\varphi}}{r^3} \right) u^{n+1} + \left(\frac{d_1^{n+1}}{c^2} + \frac{6 - \Delta_{\theta,\varphi}}{r^2} \right) \frac{\partial u^{n+1}}{\partial r} \\ & - \left(\frac{2}{c^2 r} + \frac{2}{c^3} \frac{\partial c}{\partial r} \right) \left(\sum_{j=0}^{J_0} d_0^{n-j} u^{n-j} - F^{n+1} \right) + \frac{1}{c^2} \left(\sum_{j=0}^{J_1} d_1^{n-j} \frac{\partial u^{n-j}}{\partial r} - \frac{\partial F^{n+1}}{\partial r} \right) \end{aligned} \quad (3.15b)$$

$$\begin{aligned} \frac{\partial^4 u^{n+1}}{\partial r^4} \approx & \left\{ d_0^{n+1} \left(\frac{8 - \Delta_{\theta,\varphi}}{c^2 r^2} + \frac{4}{c^3} \frac{\partial c}{\partial r} + \frac{6 \left(\frac{\partial c}{\partial r} \right)^2}{c^4} - \frac{2}{c^3} \frac{\partial^2 c}{\partial r^2} \right) + \frac{\tilde{d}_0^{n+1}}{c^4} + \frac{\Delta_{\theta,\varphi}^2 - 18\Delta_{\theta,\varphi}}{r^4} \right\} u^{n+1} \\ & - d_0^{n+1} \Delta_{\theta,\varphi} \left(\frac{u^{n+1}}{c^2 r^2} \right) + \left\{ -d_1^{n+1} \left(\frac{4}{c^2 r} + \frac{4}{c^3} \frac{\partial c}{\partial r} \right) + \frac{8\Delta_{\theta,\varphi} - 24}{r^3} \right\} \frac{\partial u^{n+1}}{\partial r} \\ & + \left(\frac{8 - \Delta_{\theta,\varphi}}{c^2 r^2} + \frac{4}{c^3} \frac{\partial c}{\partial r} + \frac{6 \left(\frac{\partial c}{\partial r} \right)^2}{c^4} - \frac{2}{c^3} \frac{\partial^2 c}{\partial r^2} \right) \sum_{j=0}^{J_0} d_0^{n-1} u^{n-j} - \sum_{j=0}^{J_0} d_0^{n-j} \Delta_{\theta,\varphi} \left(\frac{u^{n-j}}{c^2 r^2} \right) \\ & - \left(\frac{4}{c^2 r} + \frac{4}{c^3} \frac{\partial c}{\partial r} \right) \sum_{j=0}^{J_1} d_1^{n-j} \frac{\partial u^{n-j}}{\partial r} - \left(\frac{8}{c^2 r^2} + \frac{4}{c^3} \frac{\partial c}{\partial r} + \frac{6 \left(\frac{\partial c}{\partial r} \right)^2}{c^4} - \frac{2}{c^3} \frac{\partial^2 c}{\partial r^2} \right) F^{n+1} \\ & + \Delta_{\theta,\varphi} \left(\frac{F^{n+1}}{c^2 r^2} \right) + \left(\frac{2}{c^2 r} + \frac{4}{c^3} \frac{\partial c}{\partial r} \right) \frac{\partial F^{n+1}}{\partial r} - \frac{1}{c^2} \frac{\partial F^{n+1}}{\partial r^2} \\ & + \frac{1}{c^4} \left(\sum_{j=0}^{J_0} \tilde{d}_0^{n-j} u^{n-j} - \frac{\partial^2 F^{n+1}}{\partial t^2} \right) \end{aligned} \quad (3.15c)$$

where the one sided difference stencils in time (3.14a) - (3.14b) are chosen with sufficiently high order of accuracy to obtain the desired order of accuracy. For example, the second order normal derivative is the lowest order normal derivative which contains the derivative $\frac{\partial^2 u^{n+1}}{\partial t^2}$. Since the second order normal derivative contained in the Taylor series expansion (3.9) is multiplied by a factor of ϱ^2 , we need to use a third order backwards difference approximation. Since $\varrho \approx \tau$, the extension operator will be fifth order accurate overall. By similar reasoning, the lowest order normal derivatives which contains $\frac{\partial^3 u^{n+1}}{\partial t^2 \partial r}$, is the third order normal derivative. Since this term is multiplied by a factor of ϱ^3 , the time derivative $\frac{\partial^3 u^{n+1}}{\partial t^2 \partial r}$ needs to be approximated with at least second order accuracy in time. Using similar reasoning, the derivative

$\frac{\partial^4 u^{n+1}}{\partial t^4}$ needs to be approximated with at least first order accuracy in time so the extension operator remains fifth order accurate overall. Keeping the above in mind, substituting (3.15a), (3.15b), and (3.15c) into the extension operator (3.9) produces the general form

$$\mathbf{Ex}\boldsymbol{\zeta}_\Gamma^{n+1} = \mathbf{Ex}_H\boldsymbol{\zeta}_\Gamma^{n+1} + \mathbf{Ex}_I^{n+1}, \quad (3.16)$$

where

$$\begin{aligned} \mathbf{Ex}_H\boldsymbol{\zeta}_\Gamma^{n+1} = & \left[1 + \frac{\varrho^2}{2} \left(\frac{d_0^{n+1}}{c^2} - \frac{\Delta_{\theta,\varphi}}{r^2} \right) + \frac{\varrho^3}{6} \left(-d_0^{n+1} \left(\frac{2}{c^2 r} + \frac{2}{c^3} \frac{\partial c}{\partial r} \right) + \frac{4\Delta_{\theta,\varphi}}{r^3} \right) \right. \\ & + \frac{\varrho^4}{24} \left(d_0^{n+1} \left(\frac{8 - \Delta_{\theta,\varphi}}{c^2 r^2} + \frac{4}{c^3 r} \frac{\partial c}{\partial r} + \frac{6}{c^4} \left(\frac{\partial c}{\partial r} \right)^2 - \frac{2}{c^3} \frac{\partial^2 c}{\partial r^2} \right) \right. \\ & \left. \left. + \frac{\tilde{d}_0^{n+1}}{c^4} + \frac{\Delta_{\theta,\varphi}^2 - 18\Delta_{\theta,\varphi}}{r^4} \right) \right] u^{n+1} \\ & + \left[\varrho - \frac{\varrho^2}{r} + \frac{\varrho^3}{6} \left(\frac{d_1^{n+1}}{c^4} + \frac{6 - \Delta_{\theta,\varphi}}{r^2} \right) \right. \\ & \left. + \frac{\varrho^4}{24} \left(-d_1^{n+1} \left(\frac{4}{c^2 r} + \frac{4}{c^3} \frac{\partial c}{\partial r} \right) + \frac{8\Delta_{\theta,\varphi} - 24}{r^3} \right) \right] \frac{\partial u^{n+1}}{\partial r} \\ & - \frac{\varrho^4 d_0^{n+1}}{24} \Delta_{\theta,\varphi} \left(\frac{u^{n+1}}{c^2 r^2} \right), \end{aligned} \quad (3.17)$$

and

$$\begin{aligned}
\mathbf{E}x_I^{n+1} = & \left[\frac{\varrho^2}{2c^2} - \frac{\varrho^3}{3} \left(\frac{1}{c^2 r} + \frac{1}{c^3} \frac{\partial c}{\partial r} \right) \right. \\
& + \left. \frac{\varrho^4}{24} \left(\frac{8 - \Delta_{\theta, \varphi}}{c^2 r^2} + \frac{4}{c^3 r} \frac{\partial c}{\partial r} + \frac{6}{c^4} \left(\frac{\partial c}{\partial r} \right)^2 - \frac{2}{c^3} \frac{\partial^2 c}{\partial r^2} \right) \right] \sum_{j=0}^{J_0} d_0^{n-j} u^{n-j} \\
& + \left[\frac{\varrho^3}{6c^2} - \frac{\varrho^4}{24} \left(\frac{4}{c^2 r} + \frac{4}{c^3} \frac{\partial c}{\partial r} \right) \right] \sum_{j=0}^{J_1} d_1^{n-j} \frac{\partial u^{n-j}}{\partial r} - \frac{\varrho^4}{24} \Delta_{\theta, \varphi} \left(\sum_{j=0}^{J_0} \frac{d_0^{n-j} u^{n-j}}{c^2 r^2} \right) \\
& - \left[\frac{\varrho^2}{2c^2} - \frac{\varrho^3}{3c^2 r} + \frac{\varrho^4}{24} \left(\frac{8}{c^2 r^2} + \frac{4}{c^3 r} \frac{\partial c}{\partial r} + \frac{6}{c^4} \left(\frac{\partial c}{\partial r} \right)^2 - \frac{2}{c^3} \frac{\partial^2 c}{\partial r^2} \right) \right] F^{n+1} \\
& - \left[\frac{\varrho^3}{6c^2} - \frac{\varrho^4}{24} \left(\frac{2}{c^2 r} + \frac{4}{c^3} \frac{\partial c}{\partial r} \right) \right] \frac{\partial F^{n+1}}{\partial r} - \frac{\varrho^4}{24c^2} \frac{\partial^2 F^{n+1}}{\partial r^2} + \frac{\varrho^4}{24} \Delta_{\theta, \varphi} \left(\frac{F^{n+1}}{c^2 r^2} \right) \\
& + \frac{\varrho^4}{24c^2} \left(\sum_{j=0}^{\tilde{J}_0} \tilde{d}_0^{n-j} u^{n-j} - \frac{\partial^2 F^{n+1}}{\partial t^2} \right). \tag{3.18}
\end{aligned}$$

The remaining step is to replace the trace $\mathfrak{z}_\Gamma^{n+1}$ in the extension operator (3.16) with its spectral representation. To be more specific, we will represent the trace using spherical harmonics as basis functions. The spherical harmonics have several desirable properties: they are complete over the space of continuous functions on the ball, they form an orthonormal basis with respect to a weighted inner product, they are eigenfunctions of the Laplace-Beltrami operator, and the spherical harmonics representation converges rapidly for smooth functions. For more details on these properties, see Appendix B.1. For a complete description of the spherical harmonics, see [7]. Since the spherical harmonics satisfy $\Delta_{\theta, \varphi} Y_l^m = -l(l+1)Y_l^m$ on the sphere, we can simplify the tangential derivatives in the extension operator to algebraic expressions. Consider the $2(1+L)^2$ complex valued dimensional vector space spanned by the basis vectors

$$\boldsymbol{\psi}_{lm}^{(0)} = (Y_l^m, 0) \quad \boldsymbol{\psi}_{lm}^{(1)} = (0, Y_l^m), \quad 0 \leq l \leq L \text{ and } |m| \leq l. \tag{3.19}$$

As a consequence, the trace $\mathfrak{z}_\Gamma^{n+1}$ can be approximated by

$$\mathfrak{z}_\Gamma^{n+1} \approx \sum_{l=0}^L \sum_{m=-l}^l c_{lm}^{(0, n+1)} \boldsymbol{\psi}_{lm}^{(0)} + \sum_{l=0}^L \sum_{m=-l}^l c_{lm}^{(1, n+1)} \boldsymbol{\psi}_{lm}^{(1)}, \tag{3.20}$$

where the individual basis functions are defined in (3.19), the Fourier coefficients are given by

$$c_{lm}^{(0,n+1)} = \langle u^{n+1}, Y_l^m \rangle \quad c_{lm}^{(1,n+1)} = \left\langle \frac{\partial u^{n+1}}{\partial r}, Y_l^m \right\rangle, \quad (3.21)$$

and the weighted inner product is defined in (B.1). Suppose that the trace is $\boldsymbol{\zeta}_\Gamma^{n+1} = (\zeta_0^{n+1}, \zeta_1^{n+1})$, where ζ_0^{n+1} and ζ_1^{n+1} are arbitrary smooth functions. Substituting the basis functions (3.19) into the homogeneous portion of the extension operator (3.17) yields

$$\begin{aligned} \mathbf{E}x_H \boldsymbol{\psi}_{lm}^{(0)} &= \left[1 + \frac{\varrho^2}{2} \left(\frac{d_0^{n+1}}{c^2} + \frac{l(l+1)}{r^2} \right) - \frac{\varrho^3}{6} \left(d_0^{n+1} \left(\frac{2}{c^2 r} + \frac{2}{c^3} \frac{\partial c}{\partial r} \right) + \frac{4l(l+1)}{r^3} \right) \right. \\ &\quad + \frac{\varrho^4}{24} \left(d_0^{n+1} \left(\frac{8+l(l+1)}{c^2 r^2} + \frac{4}{c^3 r} \frac{\partial c}{\partial r} + \frac{6}{c^4} \left(\frac{\partial c}{\partial r} \right)^2 - \frac{2}{c^3} \frac{\partial^2 c}{\partial r^2} \right) + \frac{\tilde{d}_0^{n+1}}{c^4} \right. \\ &\quad \left. \left. + \frac{l^2(l+1)^2 + 18l(l+1)}{r^4} \right) \right] \boldsymbol{\psi}_{lm}^{(0)} + \sum_{l'=0}^L \sum_{m'=-l'}^{l'} l'(l'+1) \left\langle \frac{1}{c^2} Y_{l'}^m, Y_{l'}^{m'} \right\rangle \boldsymbol{\psi}_{l'm'}^{(0)}, \end{aligned} \quad (3.22)$$

$$\begin{aligned} \mathbf{E}x_H \boldsymbol{\psi}_{lm}^{(1)} &= \left[\varrho - \frac{\varrho^2}{r} + \frac{\varrho^3}{6} \left(\frac{d_1^{n+1}}{c^4} + \frac{6+l(l+1)}{r^2} \right) \right. \\ &\quad \left. - \frac{\varrho^4}{24} \left(d_1^{n+1} \left(\frac{4}{c^2 r} + \frac{4}{c^3} \frac{\partial c}{\partial r} \right) + \frac{8l(l+1) + 24}{r^3} \right) \right] \boldsymbol{\psi}_{lm}^{(1)}, \end{aligned} \quad (3.23)$$

where we have used the approximation

$$\left(\Delta_{\theta, \varphi} (Y_l^m / c^2), 0 \right) \approx - \sum_{l'=0}^L \sum_{m'=-l'}^{l'} l'(l'+1) \left\langle \frac{1}{c^2} Y_{l'}^{m'}, Y_l^m \right\rangle \boldsymbol{\psi}_{l'm'}^{(0)}.$$

Substituting (3.20) into the extension operator (3.16) (along with (3.22) and (3.23) while exploiting the linearity of $\mathbf{E}x_H$), we have:

$$\mathbf{E}x \boldsymbol{\zeta}_\Gamma^{n+1} = \mathbf{E}x_H \boldsymbol{\zeta}_\Gamma^{n+1} + \mathbf{E}x_I^{n+1}. \quad (3.24)$$

The homogeneous portion of the extension operator is written as

$$\mathbf{E}x_H \boldsymbol{\zeta}_\Gamma^{n+1} = \mathbf{A}_0 c_0^{n+1} + \mathbf{A}_1 c_1^{n+1},$$

where the Fourier coefficients (see formula (3.21)) can be arranged as column vectors

$$\mathbf{c}_i^n = \left[c_{0,0}^{(i,n)} \quad c_{1,-1}^{(i,n)} \quad c_{1,0}^{(i,n)} \quad c_{1,1}^{(i,n)} \quad \cdots \quad c_{L,L}^{(i,n)} \right], \quad i \in \{0,1\}, \quad (3.25)$$

and the matrices $\mathbf{A}_0, \mathbf{A}_1$ are constructed as follows

$$\mathbf{A}_i = \left[\mathbf{E}x_H \boldsymbol{\psi}_{0,0}^{(i)}, \quad \mathbf{E}x_H \boldsymbol{\psi}_{1,-1}^{(i)}, \quad \cdots, \quad \mathbf{E}x_H \boldsymbol{\psi}_{L,L}^{(i)} \right], \quad (3.26)$$

whose columns are given by (3.22) or (3.23). The inhomogeneous term (3.18) satisfies

$$\begin{aligned} \mathbf{E}x_I^{n+1} = & \sum_{l=0}^L \sum_{m=-l}^l \left\{ \left[\frac{\varrho^2}{2c^2} - \frac{\varrho^3}{3c^2 r} \right. \right. \\ & + \frac{\varrho^4}{24} \left(\frac{8+l(l+1)}{c^2 r^2} + \frac{4}{c^3 r} \frac{\partial c}{\partial r} + \frac{6}{c^4} \left(\frac{\partial c}{\partial r} \right)^2 - \frac{2}{c^3} \frac{\partial^2 c}{\partial r^2} \right) \left. \right] \boldsymbol{\psi}_{lm}^{(0)} \sum_{j=0}^{J_0} d_0^{n-j} c_{lm}^{(0,n-j)} \\ & + \left[\frac{\varrho^3}{6c^2} - \frac{\varrho^4}{24} \left(\frac{4}{c^2 r} + \frac{4}{c^3} \frac{\partial c}{\partial r} \right) \right] \boldsymbol{\psi}_{lm}^{(1)} \sum_{j=0}^{J_1} d_1^{n-j} c_{lm}^{(1,n-j)} \\ & + \frac{l(l+1)\varrho^4}{24r^2} \boldsymbol{\psi}_{lm}^{(0)} \left(\sum_{l'=0}^L \sum_{m'=-l'}^{l'} \left\langle \frac{1}{c^2} Y_{l'}^{m'}, Y_l^m \right\rangle \sum_{j=0}^{J_0} d_0^{n-j} c_{l'm'}^{(0,n-j)} \right) \\ & + \frac{\varrho^4}{24c^2} \boldsymbol{\psi}_{lm}^{(0)} \left(\sum_{j=0}^{\tilde{J}_0} \tilde{d}_0^{n-j} c_{lm}^{(0,n-j)} - \frac{1}{\tau^2} \left\langle F^{n+2} - 2F^{n+1} + F^n, Y_l^m \right\rangle \right) \left. \right\} + \mathbf{F}^{n+1}, \end{aligned} \quad (3.27)$$

where the contribution of the source term is

$$\begin{aligned}
\mathbf{F}^{n+1} = & \left[\frac{\varrho^2}{2c^2} - \frac{\varrho^3}{3c^2 r} \right. \\
& + \left. \frac{\varrho^4}{24} \left(\frac{8}{c^2 r^2} + \frac{4}{c^3 r} \frac{\partial c}{\partial r} + \frac{6}{c^4} \left(\frac{\partial c}{\partial r} \right)^2 - \frac{2}{c^3} \frac{\partial^2 c}{\partial r^2} \right) \right] \sum_{l=0}^L \sum_{m=-l}^l \langle F^{n+1}, Y_l^m \rangle Y_l^m \\
& - \left[\frac{\varrho^3}{6c^2} - \frac{\rho^4}{24} \left(\frac{2}{c^2 r} + \frac{4}{c^3} \frac{\partial c}{\partial r} \right) \right] \sum_{l=0}^L \sum_{m=-l}^l \left\langle \frac{\partial F^{n+1}}{\partial r}, Y_l^m \right\rangle Y_l^m \\
& - \frac{\varrho^4}{24c^2} \sum_{l=0}^L \sum_{m=-l}^l \left\langle \frac{\partial^2 F^{n+1}}{\partial r^2}, Y_l^m \right\rangle Y_l^m \\
& - \sum_{l=0}^L \sum_{m=-l}^l \frac{l(l+1)\varrho^4}{24r^2} \left(\sum_{l'=0}^L \sum_{m'=-l'}^{l'} \left\langle \frac{1}{c^2} Y_{l'}^{m'}, Y_l^m \right\rangle \langle F^{n+1}, Y_{l'}^{m'} \rangle \right) Y_l^m.
\end{aligned}$$

3.2.5 Solving the Interior Problem

In this section, we will demonstrate how to solve the BVP (3.1) for the modified Helmholtz equation on the domain Ω using the MDP. In Section 3.2.3, we defined the discrete counterparts to the Calderón potential and Calderón projection. These discrete counterparts reduce the discretized BVP (3.1) to an equivalent expression defined on the boundary, called the inhomogeneous boundary equation with projection (3.7). According to Theorem 3.2.1, we can obtain a discrete solution to the BVP (3.1) by substituting the density, u_γ^{n+1} , into the generalized discrete Green's formula (3.8).

We will use the extension operator (3.24) to approximate the density u_γ^{n+1} . In other words, substituting $u_\gamma^{n+1} = \mathbf{E}x_\Gamma^{n+1}$ (defined in (3.24)) into the discrete BEP (3.7) we arrive at the linear system

$$\mathbf{Q}_0 \mathbf{c}_0^{n+1} + \mathbf{Q}_1 \mathbf{c}_1^{n+1} = -\mathbf{Tr}_\gamma \mathbf{G}_h \tilde{f}_R^{n+1} - \mathbf{q}_l^{n+1}, \quad (3.28)$$

where the matrices \mathbf{Q}_i and vector \mathbf{q}_l^{n+1} are given by

$$\mathbf{Q}_i = (\mathbf{P}_\gamma - \mathbf{I}_\gamma) \mathbf{A}_i \in \mathbb{C}^{|\gamma| \times (1+L)^2}, \quad i \in \{0, 1\}, \quad (3.29a)$$

$$\mathbf{q}_l^{n+1} = (\mathbf{P}_\gamma - \mathbf{I}_\gamma) \mathbf{E}x_l^{n+1} \in \mathbb{C}^{|\gamma|}, \quad (3.29b)$$

the matrices $\mathbf{A}_i \in \mathbb{C}^{|\gamma| \times (1+L)^2}$ for $i \in \{0, 1\}$ are defined in (3.26) and the inhomogeneous term $\mathbf{E}x_l^{n+1}$ is defined in (3.18). Note that the matrices (3.29a) only need to be

computed once since they don't vary with time. This is especially important because computing the matrices \mathbf{Q}_0 and \mathbf{Q}_1 is computationally intensive. These matrices require a total of $2(1+L)^2$ applications of the operator $\mathbf{P}_\gamma - \mathbf{I}_\gamma$ where each application $\mathbf{P}_\gamma - \mathbf{I}_\gamma$ requires one call to the (complex valued) solution operator \mathbf{G}_h (3.4). Or we could use the relationship $Y_l^{-m} = (-1)^m (Y_l^m)^*$ to reduce the number of time we need to call \mathbf{G}_h by a factor of approximately two. The spherical harmonics representation of the trace ξ_Γ^{n+1} converges rapidly (Appendix B.1) provided the solution to (3.1) is smooth. This implies that even for sufficiently small L , the accuracy of the spectral representation of ξ_Γ^{n+1} on Γ exceeds the accuracy on the grid, which enables fourth order grid convergence. Moreover, the number of columns of $\mathbf{Q}_0, \mathbf{Q}_1$ appears much smaller than the number of grid points contained in the discrete boundary, i.e., $(1+L)^2 \ll |\gamma|$, which enables efficient solution of (3.28) in the sense of least squares. The RHS term (3.29b) needs to be computed on the upper time level at every step.

Note that, (3.28) contains two vector variables \mathbf{c}_0^{n+1} and \mathbf{c}_1^{n+1} which need to be computed at the upper time level. We will combine (3.28) with the given boundary condition to provide enough equations to compute each set of Fourier coefficients. If a Dirichlet boundary condition is specified on Γ , we can use the fast spherical harmonics transform (FSHT, see Appendix B.3) to compute the Fourier coefficients \mathbf{c}_0^{n+1} directly. Then, (3.28) simplifies to

$$\mathbf{Q}_1 \mathbf{c}_1^{n+1} = -\mathbf{Q}_0 \mathbf{c}_0^{n+1} - \text{Tr}_\gamma \mathbf{G}_h \tilde{f}_R^{n+1} - \mathbf{q}_I^{n+1},$$

where we need to solve for the remaining unknown vector \mathbf{c}_1^{n+1} . If a Neumann boundary condition is given, (3.28) simplifies to

$$\mathbf{Q}_0 \mathbf{c}_0^{n+1} = -\mathbf{Q}_1 \mathbf{c}_1^{n+1} - \text{Tr}_\gamma \mathbf{G}_h \tilde{f}_R^{n+1} - \mathbf{q}_I^{n+1},$$

where we need to solve for the remaining unknown vector \mathbf{c}_0^{n+1} . If the Robin boundary condition $au^{n+1} + b\frac{\partial u^{n+1}}{\partial r} = \varphi_\Gamma^{n+1}$ is given, the Fourier coefficients satisfy

$$a\mathbf{c}_0^{n+1} + b\mathbf{c}_1^{n+1} = \mathbf{c}_\Gamma^{n+1} = \left[\langle \varphi_\Gamma^{n+1}, Y_0^0 \rangle \cdots \langle \varphi_\Gamma^{n+1}, Y_L^L \rangle \right]^T, \quad (3.30)$$

Substituting (3.30) into (3.28) and eliminating the Dirichlet Fourier coefficients \mathbf{c}_0^{n+1}

yields

$$\left(\mathbf{Q}_1 - \frac{b}{a} \mathbf{Q}_0 \right) \mathbf{c}_1^{n+1} = -\frac{1}{a} \mathbf{Q}_0 \mathbf{c}_\Gamma^{n+1} - \mathbf{Tr}_\gamma \mathbf{G}_h \tilde{f}_R^{n+1} - \mathbf{q}_I^{n+1}.$$

Once \mathbf{c}_1^{n+1} is known, we can use the relationship (3.30) to determine the remaining set of Fourier coefficients \mathbf{c}_0^{n+1} . As an alternative approach, we can eliminate the Neumann Fourier coefficients \mathbf{c}_1^{n+1} to obtain the system

$$\left(\mathbf{Q}_0 - \frac{a}{b} \mathbf{Q}_1 \right) \mathbf{c}_0^{n+1} = -\frac{1}{b} \mathbf{Q}_1 \mathbf{c}_\Gamma^{n+1} - \mathbf{Tr}_\gamma \mathbf{G}_h \tilde{f}_R^{n+1} - \mathbf{q}_I^{n+1}.$$

However, we will utilize the previous implementation in all of our simulations. For more general types of boundary conditions adapted to the BEP, see [15].

In summary, combining the boundary condition with (3.28) yields the linear system

$$\mathbf{Q}^{\text{weak}} \mathbf{c}^{\text{weak}} = \mathbf{g}^{\text{weak}}, \quad (3.31)$$

where the matrix

$$\mathbf{Q}^{\text{weak}} = \begin{cases} \mathbf{Q}_1 & , \quad \text{if } l_\Gamma(u) = u \\ \mathbf{Q}_0 & , \quad \text{if } l_\Gamma(u) = \frac{\partial u}{\partial r} \\ \mathbf{Q}_1 - \frac{b}{a} \mathbf{Q}_0 & , \quad \text{if } l_\Gamma(u) = au + b \frac{\partial u}{\partial r} \end{cases},$$

the unknown

$$\mathbf{c}^{\text{weak}} = \begin{cases} \mathbf{c}_1^{n+1} & , \quad \text{if } l_\Gamma(u) = u \\ \mathbf{c}_0^{n+1} & , \quad \text{if } l_\Gamma(u) = \frac{\partial u}{\partial r} \\ \mathbf{c}_1^{n+1} & , \quad \text{if } l_\Gamma(u) = au + b \frac{\partial u}{\partial r} \end{cases},$$

and the RHS

$$\mathbf{g}^{\text{weak}} = \begin{cases} -\mathbf{Q}_0 \mathbf{c}_0^{n+1} - \mathbf{Tr}_\gamma \mathbf{G}_h \tilde{f}_R^{n+1} - \mathbf{q}_I^{n+1} & , \quad \text{if } l(u) = u \\ -\mathbf{Q}_1 \mathbf{c}_1^{n+1} - \mathbf{Tr}_\gamma \mathbf{G}_h \tilde{f}_R^{n+1} - \mathbf{q}_I^{n+1} & , \quad \text{if } l(u) = \frac{\partial u}{\partial r} \\ -\frac{1}{a} \mathbf{Q}_0 \mathbf{c}_\Gamma^{n+1} - \mathbf{Tr}_\gamma \mathbf{G}_h \tilde{f}_R^{n+1} - \mathbf{q}_I^{n+1} & , \quad \text{if } l(u) = au + b \frac{\partial u}{\partial r} \end{cases}.$$

Since the matrix $\mathbf{Q}^{\text{weak}} \in \mathbb{C}^{|\gamma| \times (1+L)^2}$ and $(1+L)^2 \ll |\gamma|$, we can solve the overdetermined linear system (3.31) in the least squares sense using QR factorization. In our implementation, we use LAPACK [4] to compute the QR factorization and solve the least squares problem (3.31). Once the Fourier coefficients c_0^{n+1} and c_1^{n+1} are known, the discrete density can be computed $u_\gamma^{n+1} = \mathbf{E} \mathbf{x} \boldsymbol{\xi}_\Gamma^{n+1}$ (def. (3.24)). Finally, we will use (3.8) to construct the discrete solution to (3.1) on the upper time level and advance the time marching scheme.

3.3 Numerical Simulations of the Interior Problem

In this section, we show that the interior problem (1.2) can be solved with fourth order accuracy using the MDP. We will measure the error of our scheme using the infinity norm

$$\|u - u_h\|_\infty = \max_n \max_{(x_i, y_j, z_k) \in \mathbb{M}^+} |u(x_i, y_j, z_k, t^n) - u_h(x_i, y_j, z_k, t^n)|,$$

where u is a given smooth solution to the interior problem (1.2) and u_h is the approximate solution to (1.2) on a uniform Cartesian grid with size h and time step τ . The rate of convergence is measured by recording the quotient

$$\text{rate} = \log \left(\frac{\|u - u_{2h}\|_\infty}{\|u - u_h\|_\infty} \right) / \log(2).$$

The following test problems will be used for simulations of the interior problem (1.2).

Example 1 Consider the test problem

$$\frac{\partial^2 u}{\partial t^2} - c^2 \Delta u = F, \quad (\mathbf{x}, t) \in \Omega \times [0, T], \quad (3.32)$$

where Ω is a ball of radius 0.9 centered at the origin. The test solution is $u(x, y, z, t) = \sin(\pi r^2) \sin(t)$ where the radial coordinate $r(x, y, z) = \sqrt{x^2 + y^2 + z^2}$ and one of the following speeds are employed: $c(x, y, z) = 1$, $c(x, y, z) = \frac{1}{2} + \frac{1}{4} \sin r$, or $c(x, y, z) = e^{(y+z)/10}$. The source term is the result of substituting the test solution and speed $c(x, y, z)$ into the left hand side of (3.32). We consider the Dirichlet boundary condition $\mathbf{l}_\Gamma(u) = \sin(\pi r^2) \sin(t)$, the Neumann boundary condition $\mathbf{l}_\Gamma(u) = 2\pi r \cos(\pi r^2) \sin(t)$, or the Robin boundary condition $\mathbf{l}_\Gamma(u) = (\sin(\pi r^2) + 2\pi r \cos(\pi r^2)) \sin(t)$ for $r = R$.

Algorithm 8 The Full Time Marching Scheme for solving the interior problem (1.2) when $\Omega = \{x \mid \|x\|_2 \leq R\}$ for a given $R > 0$, the number of auxiliary grids is ℓ (multigrid), the terminal time is t_{Final} .

- 1: Choose a cubic auxiliary domain Ω^0 which contains Ω such that $\text{dist}(\partial\Omega^0, \Omega) > 3h$.
 - 2: Build the grid sets $\mathbb{M}^+, \mathbb{M}^-, \mathbb{N}_0, \mathbb{N}^+, \mathbb{N}^-, \gamma, \gamma_{\text{proj}}$ described in Definition 3.2.1.
 - 3: There exists of a set $\Omega \subset \tilde{\Omega} \subset \Omega^0$ such that the grid set $\mathbb{N}^+ \subset \tilde{\Omega}$. Compute the time step τ using the CFL number (2.32) over $\tilde{\Omega}$.
 - 4: Precompute the components of the FSHT (see B.3).
 - 5: Precompute the matrices which define $\mathbf{E}x_H\boldsymbol{\zeta}_\Gamma$ and $\mathbf{E}x_I^{n+1}$ of (3.24).
 - 6: Compute the matrices $\mathbf{Q}_0, \mathbf{Q}_1$ of (3.29a).
 - 7: Compute the QR factorization of the matrix \mathbf{Q}^{weak} of (3.31).
 - 8: Precompute the structures associated with multigrid and FOCS.
 - 9: Initialize u on \mathbb{M}^+ and γ^+ using (C.1) and (C.5) respectively. Use these values to compute $\tilde{f}_R = h^2 \mathbf{R}_h$ on \mathbb{M}^+ .
 - 10: Initialize the Fourier coefficients c_0, c_1 for the initial time steps using the FSHT along with (C.1) and (C.3) and/or the given boundary condition.
 - 11: Evaluate the speed $c(x)$ on \mathbb{M}^+ . Use Taylor series expansion to approximate the speed on γ_{out} .
 - 12: Set $t^{n+1} = 2\tau$.
 - 13: **while** $t^{n+1} < t_{\text{Final}}$ **do**
 - 14: Assemble \tilde{f}_R^{n+1} , using (2.33) and $\tilde{f}_R^{n+1} = h^2 \mathbf{R}_h f^{n+1}$ on \mathbb{M}^+ .
 - 15: Apply the solution operator \mathbf{G}_h of (3.4) to the RHS \tilde{f}_R^{n+1} given the initial guess

$$\tilde{u}^{n+1} = 2u^n - u^{n-1} + \tau^2(c^2(x)\Delta_h u^n + F^n) \quad \text{on } \mathbb{M}^+.$$
 - 16: Compute $\mathbf{E}x_I^{n+1}$ of (3.27), then apply the operator $\mathbf{P}_\gamma - \mathbf{I}_\gamma$ of Definition 3.2.4.
 - 17: Compute the Fourier coefficients as outlined in Section 3.2.5.
 - 18: Compute the density u_γ^{n+1} using the extension operator (3.24).
 - 19: Use the generalized Green's formula (3.8) to advance the scheme.
 - 20: Reindex the variables u, \tilde{f}_R and the Fourier coefficients c_0, c_1 , and t^{n+1} .
-

The initial data is obtained from the test solution as well.

Example 2 Consider the test problem

$$\frac{\partial^2 u}{\partial t^2} - c^2 \Delta u = F, \quad (x, t) \in \Omega \times [0, T], \quad (3.33)$$

where Ω is a ball of radius 1.50 centered at the origin. Consider the generating function

$$v(x, y, z, t) = \left(1 - e^{-\frac{4}{5}r^9}\right) \left(2 \sin(t) + \frac{3}{2} \sin(t\sqrt{3})\right), \quad (3.34)$$

where the radial distance $r(x, y, z) = \sqrt{x^2 + y^2 + z^2}$. The test solution to (3.33) is given by differentiating the generating function (3.34) with respect to x . In other words the solution to (3.33) is

$$u(x, y, z, t) = \frac{36}{5} x e^{-\frac{4}{5}r^9} r^7 \left(2 \sin(t) + \frac{3}{2} \sin(t\sqrt{3})\right),$$

where the radial coordinate $r(x, y, z) = \sqrt{x^2 + y^2 + z^2}$ and one of the following speeds are employed: $c(x, y, z) = 1$, $c(x, y, z) = \frac{1}{2} + \frac{1}{4} \sin r$, or $c(x, y, z) = e^{(y+z)/10}$. The source term is generated by substituting the test solution into (3.33). The Dirichlet boundary condition is

$$l_{\Gamma}(u) = \frac{36}{5} x e^{-\frac{4}{5}r^9} r^7 \left(2 \sin(t) + \frac{3}{2} \sin(t\sqrt{3})\right),$$

the Neumann boundary condition

$$l_{\Gamma}(u) = \frac{36}{5} x e^{-\frac{4}{5}r^9} r^6 (1 + 9(4r^9/5 - 1)) \left(2 \sin(t) + \frac{3}{2} \sin(t\sqrt{3})\right),$$

and the Robin boundary condition

$$l_{\Gamma}(u) = \frac{36}{5} x e^{-\frac{4}{5}r^9} r^6 (r + 1 + 9(4r^9/5 - 1)) \left(2 \sin(t) + \frac{3}{2} \sin(t\sqrt{3})\right),$$

whenever $(x, y, z) \in \Gamma$.

Table 3.2: Grid refinement analysis for the test problem (3.32) where the auxiliary domain $\Omega_0 = [-1.5, 1.5]^3$ and the terminal time $T = 5$. Here the speed is $c(x, y, z) = 1$, the uniform time step τ is 90% of the maximum CFL shown in (2.32), and the order of the spectral representation $L = 20$. See Table 1.1 for the specific settings for our multigrid method.

Grid	Dirichlet		Neumann		Robin	
	error	rate	error	rate	error	rate
$33 \times 33 \times 33$	1.076e-03	—	1.012e-01	—	1.628e-02	—
$65 \times 65 \times 65$	6.114e-05	4.133	7.853e-03	3.687	1.221e-03	3.736
$129 \times 129 \times 129$	3.761e-06	4.028	4.531e-04	4.115	7.049e-05	4.115
$257 \times 257 \times 257$	2.382e-07	3.981	2.664e-05	4.088	4.164e-06	4.082

Table 3.3: Grid refinement analysis for the test problem (3.32) where $R = 0.90$ and the auxiliary domain $\Omega_0 = [-1.5, 1.5]^3$. Here the speed is $c(x, y, z) = \frac{1}{2} + \frac{1}{4} \sin \sqrt{x^2 + y^2 + z^2}$. The order of the spectral representation $L = 20$. The uniform time step τ is 90% of the maximum CFL shown in (2.32). See Table 1.1 for the specific settings for our multigrid method.

Grid	Dirichlet		Neumann		Robin	
	error	rate	error	rate	error	rate
$33 \times 33 \times 33$	1.592e-03	—	4.388e-02	—	1.111e-02	—
$65 \times 65 \times 65$	1.023e-04	3.960	3.336e-03	3.717	8.320e-04	3.746
$129 \times 129 \times 129$	6.346e-06	4.011	1.857e-04	4.167	4.686e-05	4.150
$257 \times 257 \times 257$	3.998e-07	3.989	1.015e-05	4.194	2.593e-06	4.176

Table 3.4: Grid refinement analysis for the test problem (3.32) where $R = 0.90$ and the auxiliary domain $[-1.5, 1.5]^3$. Here the speed is $c(x, y, z) = e^{(y+z)/10}$. The uniform time step τ is 90% of the maximum CFL shown in (2.32). The order of the spectral representation $L = 20$. The maximum speed was taken on the smallest ball which contains the grid set \mathbb{N}^+ on the coarsest grid used in our simulations. See Table 1.1 for the specific settings for our multigrid method.

Grid	Dirichlet		Neumann		Robin	
	error	rate	error	rate	error	rate
$33 \times 33 \times 33$	1.025e-03	—	1.048e-01	—	1.674e-02	—
$65 \times 65 \times 65$	6.159e-05	4.057	8.022e-03	3.708	1.249e-03	3.744
$129 \times 129 \times 129$	3.928e-06	3.971	4.616e-04	4.119	7.221e-05	4.113
$257 \times 257 \times 257$	2.489e-07	3.980	2.707e-05	4.092	4.253e-06	4.089

Table 3.5: Grid refinement analysis for the test problem (3.33) the auxiliary domain $[-2.0, 2.0]^3$, and the order of the spectral representation $L = 20$. Here the speed is $c(x, y, z) = 1$. The uniform time step τ is 98% of the maximum CFL shown in (2.32). See Table 1.1 for the specific settings for our multigrid method.

Grid	Dirichlet		Neumann		Robin	
	error	rate	error	rate	error	rate
$33 \times 33 \times 33$	3.687e-01	—	3.687e-01	—	3.687e-01	—
$65 \times 65 \times 65$	2.052e-02	4.167	2.052e-02	4.167	2.052e-02	4.167
$129 \times 129 \times 129$	1.162e-03	4.143	1.162e-03	4.143	1.162e-03	4.143
$257 \times 257 \times 257$	7.086e-05	4.036	7.086e-05	4.036	7.086e-05	4.036

Table 3.6: Grid refinement analysis for the test problem (3.33) where $R = 1.5$, the auxiliary domain $[-2.0, 2.0]^3$, and the order of the spectral representation $L = 20$. Here the speed is $c(x, y, z) = \frac{1}{2} + \frac{1}{4} \sin \sqrt{x^2 + y^2 + z^2}$. The uniform time step τ is 98% of the maximum CFL shown in (2.32). See Table 1.1 for the specific settings for our multigrid method.

Grid	Dirichlet		Neumann		Robin	
	error	rate	error	rate	error	rate
$33 \times 33 \times 33$	3.735e-01	—	3.735e-01	—	3.735e-01	—
$65 \times 65 \times 65$	2.077e-02	4.169	2.077e-02	4.169	2.077e-02	4.169
$129 \times 129 \times 129$	1.181e-03	4.136	1.181e-03	4.136	1.181e-03	4.136
$257 \times 257 \times 257$	7.244e-05	4.027	7.244e-05	4.027	7.244e-05	4.027

Table 3.7: Grid refinement analysis for the test problem (3.33) where $R = 1.5$, the auxiliary domain $[-2.0, 2.0]^3$, and the order of the spectral representation $L = 20$. Here the speed is $c(x, y, z) = e^{(y+z)/10}$. The uniform time step τ is 98% of the maximum CFL shown in (2.32). The maximum speed was taken on the smallest ball which contains the grid set \mathbb{N}^+ on the coarsest grid used in our simulations. See Table 1.1 for the specific settings for our multigrid method.

Grid	Dirichlet		Neumann		Robin	
	error	rate	error	rate	error	rate
$33 \times 33 \times 33$	3.773e-01	—	3.733e-01	—	3.727e-01	—
$65 \times 65 \times 65$	2.055e-02	4.199	2.034e-02	4.198	2.033e-02	4.196
$129 \times 129 \times 129$	1.158e-03	4.150	1.161e-03	4.131	1.160e-03	4.131
$257 \times 257 \times 257$	7.090e-05	4.029	7.099e-05	4.032	7.094e-05	4.032

Chapter 4

RADIATION OF WAVES BY A KNOWN SOURCE

Consider the exterior problem (1.4) on the entire \mathbb{R}^3 . In order to solve this exterior problem with a conventional approach such as a finite difference or finite element method, one needs to truncate the domain of (1.4). We will consider two approaches.

The first approach is to use a damping layer (or sponge layer). We will consider a sufficiently large cubic vacuum region D_{vac} that contains the support of the source term F . Then, we will surround this cube with a layer of thickness ℓ on all sides. The purpose of this layer is to damp any outgoing waves from D_{vac} . Finally we will replace the exterior problem (1.4) with the damped acoustic equation

$$\begin{aligned} \frac{\partial^2 u}{\partial t^2} + \sigma(\mathbf{x}) \frac{\partial u}{\partial t} &= c^2(\mathbf{x}) \Delta u + F, & \mathbf{x} \in D, \\ u &= 0, & \mathbf{x} \in \partial D, \end{aligned} \tag{4.1}$$

where $D_{\text{vac}} = [\bar{x}_l, \bar{x}_r]^3$ and $D = [\bar{x}_l - \ell, \bar{x}_r + \ell]^3$. By construction, the damping profile σ is zero in the vacuum region D_{vac} and positive in the damping layer $D \setminus D_{\text{vac}}$ (while for the source term F it is the other way around). In the layer, the damping profile σ steadily increases from zero at the boundary of D_{vac} to some maximum value at the edge of the computational domain D . The damped acoustic wave equation (4.1) clearly coincides with (1.4) in the vacuum region D_{vac} . However, replacing (1.4) with (4.1) introduces artificial reflections from the boundary of the computational domain D . We will show that if the profile σ is chosen carefully and the damping layer is

sufficiently thick, we can attenuate these artificial reflections. See Section 4.1 for our discussion of the sponge layer.

The second approach is the use of an artificial boundary condition on a spherical artificial outer boundary. We will choose a sufficiently large spherical domain (a ball) to contain the support of the source term F . On the boundary of the ball, we will impose the p^{th} order ABC $B_p u = 0$, see Section 1.2.2, where p is chosen so as to provide high level of absorption for any outgoing waves. In other words, we will replace the exterior problem (1.4) with

$$\begin{aligned} \frac{\partial^2 u}{\partial t^2} - c^2(\mathbf{x})\Delta u &= F(\mathbf{x}, t), \quad \mathbf{x} \in \Omega \times (0, \infty), \\ u(\mathbf{x}, 0) &= 0, \quad \mathbf{x} \in \mathbb{R}^3, \\ \frac{\partial u}{\partial t}(\mathbf{x}, 0) &= 0, \quad \mathbf{x} \in \mathbb{R}^3, \\ B_p u &= 0, \quad \mathbf{x} \in \Gamma, \end{aligned} \tag{4.2}$$

where one can take $R > 0$ such that $\Omega = \{\mathbf{x} \mid \|\mathbf{x}\|_2 \leq R\}$. In Section 4.2, we will discuss the implementation of the high order artificial boundary condition $B_p u = 0$ (1.10a) - (1.10b).

4.1 Sponge Layer

In this section, we will discuss the damped acoustic wave equation (4.1). To be more specific, Section 4.1.1 will discuss how to approximate (4.2) in time and space with fourth order accuracy. We discretize (4.2) in time using the θ -scheme [23, 68]. This produces a one parameter family of elliptic PDEs using only three levels in time. This elliptic PDE is discretized in space using a $3 \times 3 \times 3$ stencil. In section 4.1.2, we perform a stability analysis of the scheme. We demonstrate that the CFL number is not affected by the damping profile $\sigma(\mathbf{x})$. In Section 4.1.3, we will show how the damping profile $\sigma(\xi)$ is constructed from the arc tangent function. Finally, Section 4.1.4 presents the results of numerical simulations for the sponge layer. We show that the fourth order grid convergence takes place provided that the sponge layer is sufficiently thick.

4.1.1 High Order Discretization of the Damped Wave Equation

We will mimic the semi-discrete approach employed in Chapter 2. This means, we will discretize (4.1) with fourth order accuracy in time using only three time levels. This will produce a modified Helmholtz equation on the upper time level which needs to be solved at every time step. Then, we will use the fourth order compact scheme derived in Section 2.2 to discretize the modified Helmholtz equation in space.

Consider the damped wave equation (4.1) at the n^{th} time level for a given $\mathbf{x} \in D$. Applying central differences on the n^{th} time level to (4.1) yields

$$\delta_t^2 u^n + \sigma \delta_t u^n - \frac{\tau^2}{12} \left(\frac{\partial^4 u^n}{\partial t^4} + 2\sigma \frac{\partial^3 u^n}{\partial t^3} \right) + \mathcal{O}(\tau^4) = c^2 \Delta u^n + F^n, \quad (4.3)$$

where

$$\delta_t^2 u^n = \frac{u^{n+1} - 2u^n + u^{n-1}}{\tau^2}, \quad \delta_t u^n = \frac{u^{n+1} - u^{n-1}}{2\tau}.$$

Next, we will replace the high order derivatives contained in the $\sim \tau^2$ term of equation (4.3). Differentiating (4.1) once and twice with respect to t yields the third and fourth order derivatives:

$$\frac{\partial^3 u}{\partial t^3} = c^2 \Delta \frac{\partial u}{\partial t} - \sigma \frac{\partial^2 u}{\partial t^2} + \frac{\partial F}{\partial t}, \quad (4.4a)$$

$$\frac{\partial^4 u}{\partial t^4} = c^2 \Delta \frac{\partial^2 u}{\partial t^2} - \sigma \frac{\partial^3 u}{\partial t^3} + \frac{\partial^2 F}{\partial t^2}. \quad (4.4b)$$

Combining (4.4a) - (4.4b) implies that

$$\begin{aligned} \frac{\partial^4 u^n}{\partial t^4} + 2\sigma \frac{\partial^3 u^n}{\partial t^3} &= (c^2 \Delta - \sigma^2) \frac{\partial^2 u^n}{\partial t^2} + \sigma c^2 \Delta \frac{\partial u^n}{\partial t} + \sigma \frac{\partial F^n}{\partial t} + \frac{\partial^2 F^n}{\partial t^2} \\ &= (c^2 \Delta - \sigma^2) \delta_t^2 u^n + \sigma c^2 \Delta \delta_t u^n + \delta_t^2 F^n + \mathcal{O}(\tau^2), \end{aligned} \quad (4.5)$$

where $\sigma \frac{\partial F}{\partial t} = 0$ since the source vanishes in the damping layer and the damping profile vanishes in vacuum region D_{vac} . Substituting (4.5) into (4.3) produces

$$\left(1 + \frac{\tau^2}{12}(\sigma^2 - c^2 \Delta)\right) \delta_t^2 u^n + \sigma \left(1 - \frac{\tau^2 c^2}{12} \Delta\right) \delta_t u^n = c^2 \Delta u^n + F^n + \frac{\tau^2}{12} \delta_t^2 F^n + \mathcal{O}(\tau^4). \quad (4.6)$$

Expanding (4.6), gathering terms on the upper time level, and dropping the error term

$\mathcal{O}(\tau^4)$ yields

$$\begin{aligned} \frac{1}{12} \left(\frac{12}{\tau^2} + \sigma^2 + \frac{6\sigma}{\tau} \right) u^{n+1} - \frac{c^2}{12} \left(1 + \frac{\tau\sigma}{2} \right) \Delta u^{n+1} &= \frac{1}{6} \left(\frac{12}{\tau^2} + \sigma^2 \right) u^n + \frac{5c^2}{6} \Delta u^n \\ - \frac{1}{12} \left(\frac{12}{\tau^2} + \sigma^2 - \frac{6\sigma}{\tau} \right) u^{n-1} + \frac{c^2}{12} \left(1 - \frac{\tau\sigma}{2} \right) \Delta u^{n-1} &+ \frac{1}{12} \left(F^{n+1} + 10F^n + F^{n-1} \right). \end{aligned} \quad (4.7)$$

Rearranging (4.7) leads to the modified Helmholtz Equation

$$(\Delta - \kappa^2)u^{n+1} = f^{n+1}, \quad (4.8)$$

where

$$\kappa^2 = \frac{\frac{12}{\tau^2} + \sigma^2 + \frac{6\sigma}{\tau}}{c^2 \left(1 + \frac{\tau\sigma}{2} \right)}, \quad (4.9)$$

will be referred to as the ‘‘wavenumber’’ and the RHS term is given by

$$\begin{aligned} f^{n+1} &= -\frac{\frac{12}{\tau^2} + \sigma^2}{6c^2 \left(1 + \frac{\tau\sigma}{2} \right)} u^n + \frac{\frac{12}{\tau^2} + \sigma^2 - \frac{6\sigma}{\tau}}{12c^2 \left(1 + \frac{\tau\sigma}{2} \right)} u^{n-1} - \frac{5\Delta u^n}{6 \left(1 + \frac{\tau\sigma}{2} \right)} - \frac{1 - \frac{\tau\sigma}{2}}{1 + \frac{\tau\sigma}{2}} \Delta u^{n-1} \\ &- \frac{F^{n+1} + 10F^n + F^{n-1}}{12 \left(1 + \frac{\tau\sigma}{2} \right)}. \end{aligned} \quad (4.10)$$

Discretizing (4.8) in space produces the discrete modified Helmholtz equation

$$\mathbf{L}_h[\kappa^2]u^{n+1} = h^2 \mathbf{R}_h f^{n+1}, \quad (4.11)$$

where the left- and right-hand side operators are described in (2.25) and (2.26), respectively. Note that, equation (4.8) implies $\Delta u^{n+1} = f^{n+1} + \kappa^2 u^{n+1}$ where the ‘‘wavenumber’’ κ^2 is defined in (4.9). This allows us to express the fourth order accurate Laplacian Δu^{n+1} on the upper time level via the solution u^{n+1} and the quantities that pertain to the previous two time levels, including the Laplacian, see (4.10). Moreover, Δu is zero on ∂D because the source term has compact support, $u = 0$ on ∂D , and the propagation speed $c(x) > 0$ for all $x \in D$. Therefore, we can treat the Laplacian as an additional quantity to keep track of in our time marching scheme. For a complete description of how to discretize the modified Helmholtz equation with fourth order

accuracy in space, please see Section 2.2.

The fourth order compact scheme (4.11) will be solved using a multigrid method. See (1.2.5) for a short description of multigrid and Table 1.1 for our particular settings for multigrid. We can use the data from the previous time steps to provide a very good initial guess to our multigrid method. According to the Taylor's formula, we have:

$$u^{n\pm 1} = u^n \pm \tau \frac{\partial u^n}{\partial t} + \frac{\tau^2}{2} \frac{\partial^2 u^n}{\partial t^2} \pm \frac{\tau^3}{6} \frac{\partial^3 u^n}{\partial t^3} + \frac{\tau^4}{24} \frac{\partial^4 u^n}{\partial t^4} \pm \frac{\tau^5}{120} \frac{\partial^5 u^n}{\partial t^5} + \mathcal{O}(\tau^6).$$

Therefore,

$$u^{n+1} = 2u^n - u^{n-1} + \tau^2 \frac{\partial^2 u^n}{\partial t^2} + \frac{\tau^4}{12} \frac{\partial^4 u^n}{\partial t^4} + \mathcal{O}(\tau^6).$$

Replacing the second order time derivative in the previous formula with the expression derived from damped wave equation (4.1), we obtain:

$$u^{n+1} = 2u^n - u^{n-1} + \tau^2 \left(c^2 \Delta u^n + F^n - \sigma \frac{\partial u^n}{\partial t} \right) + \frac{\tau^4}{12} \frac{\partial^4 u^n}{\partial t^4} + \mathcal{O}(\tau^6).$$

Approximating the first order time derivative in this equation with central differences and rearranging, we arrive at

$$\left(1 + \frac{\tau\sigma}{2} \right) u^{n+1} = 2u^n - \left(1 - \frac{\tau\sigma}{2} \right) u^{n-1} + \tau^2 \left(c^2 \Delta u^n + F^n \right) + \mathcal{O}(\tau^4).$$

Then, we can use the initial guess

$$\tilde{u}^{n+1} = \frac{2u^n}{1 + \frac{\tau\sigma}{2}} - \frac{\left(1 - \frac{\tau\sigma}{2} \right) u^{n-1}}{1 + \frac{\tau\sigma}{2}} + \frac{\tau^2}{1 + \frac{\tau\sigma}{2}} \left(c^2 \Delta u^n + F^n \right), \quad (4.12)$$

for the multigrid solver for (4.11).

4.1.2 Stability Criteria

Let $\lambda = \lambda(\mathbf{x})$ denote the CFL number:

$$\lambda(\mathbf{x}) = \frac{c(\mathbf{x})\tau}{h},$$

where h is the grid size in space and τ is the grid size in time. The following proof was first presented in our work [58]. It is a generalization of the proof previously published in [18], see also [96]. We will see that the additional damping term $\sigma \frac{\partial u}{\partial t}$ incorporated into the wave equation doesn't decrease the CFL number described in Section 2.3.

Theorem 4.1.1. Let the discrete operator $\frac{1}{h^2} \mathbf{L}_h$ approximate the Laplacian Δ and satisfy

- ◇ \mathbf{L}_h is negative definite. In other words, there exists a real inner product (\cdot, \cdot) where $(-\mathbf{L}_h u, u) \geq 0$ and there exists two positive numbers $0 < L_{\text{lower}} < L_{\text{upper}}$ such that

$$0 < L_{\text{lower}} \|u\|^2 \leq (-\mathbf{L}_h u, u) \leq L_{\text{upper}} \|u\|^2,$$

where the norm is induced by the inner product.

- ◇ \mathbf{L}_h is self-adjoint. In other words $(\mathbf{L}_h u, v) = (u, \mathbf{L}_h v)$.

Then discretizing the homogeneous damped wave equation $\frac{1}{c^2} \frac{\partial^2 u}{\partial t^2} + \sigma \frac{\partial u}{\partial t} = \Delta u$ in time according to (4.6) (or (4.7)) and approximating the Laplacian with $\frac{1}{h^2} \mathbf{L}_h$ produces a scheme which is conditionally stable provided

$$\max_x \lambda^2(\mathbf{x}) \leq \frac{6}{L_{\text{upper}}}.$$

Proof. After expanding (4.6) and replacing the Laplacian with \mathbf{L}_h/h^2 , we obtain

$$\begin{aligned} & \left(\frac{1}{c^2 \tau^2} + \frac{\sigma^2}{12c^2} \right) (u^{n+1} - 2u^n + u^{n-1}) + \frac{\sigma}{2c^2 \tau} (u^{n+1} - u^{n-1}) \\ &= \frac{\mathbf{L}_h}{12h^2} (u^{n+1} + 10u^n + u^{n-1}) + \frac{\tau \sigma \mathbf{L}_h}{24h^2} (u^{n+1} - u^{n-1}) \\ &= \frac{\mathbf{L}_h}{h^2} \left(\frac{1}{12} (u^{n+1} - u^n) - \frac{1}{12} (u^n - u^{n-1}) + u^n \right) + \frac{\tau \sigma \mathbf{L}_h}{24h^2} (u^{n+1} - u^{n-1}). \end{aligned} \quad (4.13)$$

Define the variable $v^{n+1} = u^{n+1} - u^n$ which satisfies

$$\begin{aligned} v^{n+1} - v^n &= u^{n+1} - 2u^n + u^{n-1}, \\ v^{n+1} + v^n &= u^{n+1} - u^{n-1}. \end{aligned}$$

Taking the inner product of $h^2(v^{n+1} + v^n)$ with (4.13) yields

$$\begin{aligned} & \frac{h^2}{c^2\tau^2} \left(1 + \frac{\tau^2\sigma^2}{12}\right) (v^{n+1} - v^n, v^{n+1} + v^n) + \frac{h^2}{2c^2\tau} (\sigma(v^{n+1} + v^n), v^{n+1} + v^n) \\ &= \left(\mathbf{L}_h u^n + \frac{1}{12}\mathbf{L}_h(v^{n+1} - v^n), v^{n+1} + v^n\right) + \frac{\tau}{2} \left(\frac{\sigma}{12}\mathbf{L}_h(v^{n+1} + v^n)v^{n+1} + v^n\right). \end{aligned}$$

Since the CFL number $\lambda = c\tau/h$, the previous equation simplifies to

$$\begin{aligned} & \frac{1}{\lambda} \left(1 + \frac{\tau^2\sigma^2}{12}\right) (\|v^{n+1}\|^2 - \|v^n\|^2) + \frac{h^2}{2c^2\tau} (\sigma(v^{n+1} + v^n), v^{n+1} + v^n) \\ &= \frac{1}{12} ((\mathbf{L}_h v^{n+1}, v^{n+1}) - (\mathbf{L}_h v^n, v^n)) + (\mathbf{L}_h u^n, u^{n+1} + v^n) \\ & \quad + \frac{\tau}{2} \left(\frac{\sigma}{12}\mathbf{L}_h(v^{n+1} + v^n), v^{n+1} + v^n\right), \end{aligned}$$

where we have used the self-adjoint property of \mathbf{L}_h to eliminate the cross terms. Rearranging the last equation, we have

$$\begin{aligned} & \frac{1}{\lambda^2} \left(1 + \frac{\tau^2\sigma^2}{12}\right) \|v^{n+1}\|^2 - \frac{1}{12} (\mathbf{L}_h v^{n+1}, v^{n+1}) + \frac{h^2}{2c^2\tau} (\sigma(v^{n+1} + v^n), v^{n+1} + v^n) \\ &= \frac{1}{\lambda^2} \left(1 + \frac{\tau^2\sigma^2}{12}\right) \|v^n\|^2 - \frac{1}{12} (\mathbf{L}_h v^n, v^n) + (\mathbf{L}_h u^n, v^{n+1} + v^n) \\ & \quad + \frac{\tau}{2} \left(\frac{\sigma}{12}\mathbf{L}_h(v^{n+1} + v^n)v^{n+1} + v^n\right). \end{aligned} \tag{4.14}$$

Substituting the identity

$$\begin{aligned} & (\mathbf{L}_h u^n, v^{n+1} + v^n) - (\mathbf{L}_h u^n, u^{n+1} - u^{n-1}) \\ &= \frac{1}{4} \left((\mathbf{L}_h v^n, v^n) - (\mathbf{L}_h v^{n+1}, v^{n+1}) - (\mathbf{L}_h(u^n + u^{n-1}), u^n + u^{n-1}) \right. \\ & \quad \left. + (\mathbf{L}_h(u^n + u^{n+1}), u^n + u^{n+1}) \right), \end{aligned}$$

into (4.14) and rearranging, we arrive at

$$E_{n+1} = E_n - \frac{h^2}{2c^2\tau} (\sigma(v^{n+1} + v^n), v^{n+1} + v^n) + \frac{\tau}{2} \left(\frac{\sigma}{12}\mathbf{L}_h(v^{n+1} + v^n)v^{n+1} + v^n\right),$$

where the energy

$$E_n = \frac{1}{\lambda^2} \left(1 + \frac{\sigma^2 \tau^2}{12} \right) \|v^n\|^2 + \frac{1}{6} (\mathbf{L}_h v^n, v^n) - \frac{1}{4} (\mathbf{L}_h (u^n + u^{n-1}), u^n + u^{n-1}).$$

Note that the inner product satisfies the inequality

$$\sigma_{\min} \|v^{n+1} + v^n\| \leq (\sigma(v^{n+1} + v^n), v^{n+1} + v^n) \leq \sigma_{\max} \|v^{n+1} + v^n\|,$$

and $(\frac{\sigma}{12} \mathbf{L}_h (v^{n+1} + v^n), v^{n+1} + v^n) \leq 0$ when σ is constant. Therefore, $\{E_n\}_{n \geq 0}$ is a non-increasing sequence. All that's left to show is that E_n is equivalent to some norm. Using the property $0 < L_{\text{lower}} \|u\|^2 \leq (-\mathbf{L}_h u, u) \leq L_{\text{upper}} \|u\|^2$ one can show that

$$\begin{aligned} \left(\frac{1}{\lambda^2} - \frac{1}{6} L_{\text{upper}} \right) \|v^n\|^2 + \frac{L_{\text{lower}}}{4} \|u^n + u^{n-1}\|^2 &\leq E_n \leq \\ \left(\frac{1}{\lambda^2} - \frac{1}{6} L_{\text{lower}} \right) \|v^n\|^2 + \frac{L_{\text{upper}}}{4} \|u^n + u^{n-1}\|^2. \end{aligned}$$

Therefore E_n is equivalent to $\|u^n - u^{n-1}\|^2 + \|u^n + u^{n-1}\|^2$ which is equivalent to $\|u^n\|^2 + \|u^{n-1}\|^2$ if and only if $\frac{1}{\lambda^2} - \frac{1}{6} L_{\text{upper}} \geq 0$. Taking the maximum over all x completes the proof. \square

Thus the addition of the damping term to the acoustic wave equation doesn't affect the size of the CFL number. So the CFL number predicted in Section 2.3 will remain the same. In other words the CFL for the time marching scheme of the sponge layer is

$$\max_x \lambda(x) \leq \sqrt{\frac{5}{8}}.$$

4.1.3 Damping Profile

In this section, we will explicitly define the damping profile $\sigma(x)$ described in (4.1). Recall that, the damping profile needs to be zero inside the vacuum region D_{vac} where the damped wave equation is supposed to coincide with the original wave equation of (1.4). However, the damping profile is positive inside the damping layer $D \setminus D_{\text{vac}}$. We will construct the overall damping profile as a linear combination of individual damping profiles that vary along the $x, y,$ and z axes, respectively. Consider the shape

function

$$s(x) = \frac{1}{2} + \frac{\arctan \alpha(2x - 1)}{2 \arctan \alpha}, \quad x \in [0, 1], \quad \alpha > 0, \quad (4.15)$$

which we show in Figure 4.1 for several values of α . The shape function (4.15) is a

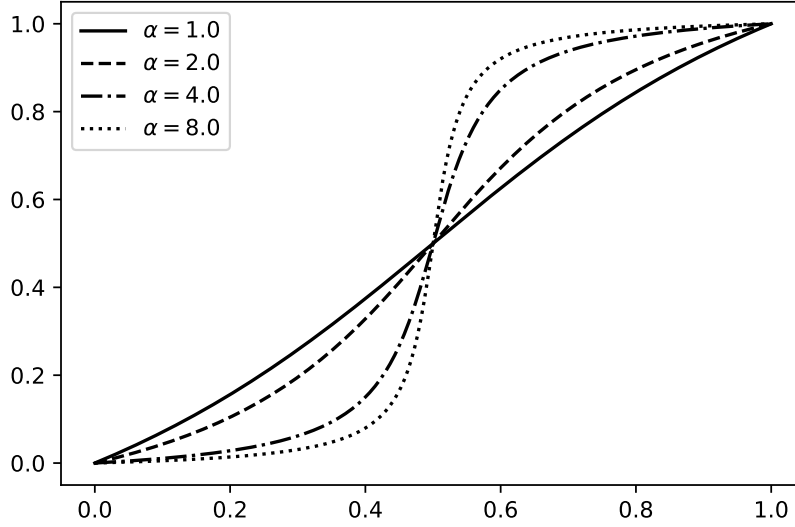


Figure 4.1: Plots of the shape function (4.15) for several values of α .

monotonically increasing function over $[0, 1]$ with the maximum value of one and minimum value of zero. We will use this shape function to construct a damping profile that varies along one direction. Accordingly,

$$\sigma^{(x)}(x) = \begin{cases} \sigma_{\max} s(|x - \bar{x}_r|/\ell) & \text{if } \bar{x}_r < x \leq \bar{x}_r + \ell \\ 0 & \text{if } \bar{x}_l \leq x \leq \bar{x}_r \\ \sigma_{\max} s(|x - \bar{x}_l|/\ell) & \text{if } \bar{x}_l - \ell \leq x < \bar{x}_l \end{cases}, \quad (4.16)$$

where the shape function s is defined in (4.15) and $\sigma_{\max} > 0$. Figure 4.2 shows several examples of the profile (4.16). By construction, the univariate damping profile (4.16) is non-zero in the damping layer, but zero in the vacuum region. Finally we will define

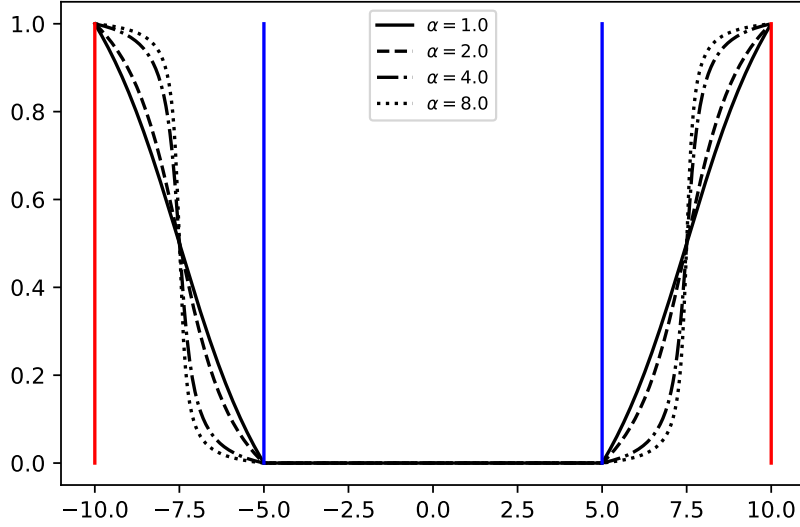


Figure 4.2: Plots of the univariate damping profile (4.16) assuming $\bar{x}_l = -5.0$, $\bar{x}_r = 5.0$, $\ell = 5.0$, and $\sigma_{\max} = 1.0$ for several values of α . The interval between the two vertical blue lines represents the vacuum region. The interval between the vertical blue line and vertical red line is the damping region.

the overall damping profile as follows

$$\sigma(x, y, z) = \sigma^{(x)}(x) + \sigma^{(y)}(y) + \sigma^{(z)}(z),$$

where the univariate damping profiles are given by (4.16). In principle, (4.15) is not the only choice and we could use any increasing function $s(x)$ satisfying $s(0) = 0$ and $s(1) = 1$ where $0 \leq s(x) \leq 1$ for each $x \in [0, 1]$. However, we observed in [58] that the sensitivity of the error to the shape of the profile was low. In addition, we observed that increasing σ_{\max} did not substantially improve the error either. Hence, we will only consider $\sigma_{\max} = 1$ and focus on increasing the sponge layer thickness ℓ to reach the desired level of accuracy.

4.1.4 Numerical Simulations with the Sponge Layer

In this section we show that the exterior problem (1.4) truncated with the sponge layer can be solved with fourth order accuracy provided that the sponge layer is sufficiently

thick. We will measure the error of our scheme using the infinity norm

$$\|u - u_h\|_\infty = \max_n \max_{(x_i, y_j, z_k) \in D_{\text{vac}}} |u(x_i, y_j, z_k, t^n) - u_h(x_i, y_j, z_k, t^n)|, \quad (4.17)$$

where u is a smooth solution to the exterior problem (1.4) and u_h is a discrete solution to (4.1) on a uniform grid with spatial size h and time step of τ . The vacuum region in (4.17) is $D_{\text{vac}} = [-\bar{x}, \bar{x}]^3$, while the uniform grid with size h extends over the entire computational domain $D = [-(\bar{x} + \ell), \bar{x} + \ell]^3$. The rate of convergence is defined as

$$\text{rate} = \log \left(\frac{\|u - u_{2h}\|_\infty}{\|u - u_h\|_\infty} \right) / \log(2). \quad (4.18)$$

The performance of the algorithm will be tested by solving a constant-coefficient wave equation subject to the homogeneous initial conditions, which is a particular realization of (1.4):

$$\begin{aligned} \frac{\partial^2 u}{\partial t^2} - \Delta u &= F(\mathbf{x}, t), \quad (\mathbf{x}, t) \in \mathbb{R}^3 \times (0, \infty), \\ u(\mathbf{x}, 0) &= 0, \quad \mathbf{x} \in \mathbb{R}^3, \\ \frac{\partial u}{\partial t}(\mathbf{x}, 0) &= 0, \quad \mathbf{x} \in \mathbb{R}^3, \end{aligned} \quad (4.19)$$

The specific test solutions to (4.19) that we are going to use are as follows.

Test solution 1. The solution $u = u_{7,1.5}^{\text{Test}}$ (see formula (A.3)) and source term $F = F_{7,1.5}^{\text{Test}}$ (see formula (A.5)) are generated by the wavelet $S(t) = 5(1 - 12t^2)e^{-6t^2}$ centered at the origin $(x_0, y_0, z_0) = (0, 0, 0)$ with the translation $t_0 = 3$.

Test solution 2. The solution $u = u_{7,1.0}^{\text{Test}}$ (see formula (A.3)) and source term $F = F_{7,1.0}^{\text{Test}}$ (see formula (A.5)) are generated by the sinusoidal pulse $S(t) = 3 \sin(8t)e^{-6t^2}$ centered at $(x_0, y_0, z_0) = \left(\frac{15}{100}, \frac{15}{100}, \frac{15}{100}\right)$ with the translation $t_0 = 4.0$.

Recall that, there are two sources of error: the reflection error due to replacing the exterior problem (1.4) with the damped wave equation (4.1) and the discretization error due to approximating (4.1) with the fourth order compact scheme. The total error $E^{(h,\ell)} = \tilde{E}^{\text{Sponge}} + \tilde{E}^h$ where the discretization error $\tilde{E}^h = \mathcal{O}(h^4)$ and the reflection error

$\tilde{E}^{\text{Sponge}}$ decreases as the thickness of the sponge layer, ℓ , increases. If $|\tilde{E}^{\text{Sponge}}| \ll |\tilde{E}^h|$ the quotient $\log \left(E^{(2h,\ell)} / E^{(h,\ell)} \right) \approx 4$. Once $|\tilde{E}^{\text{Sponge}}| \approx |\tilde{E}^h|$, refining the grid no longer improves the error since the reflection errors don't depend on the grid size h . This behavior is clearly demonstrated in Figure 4.3. When $t < 5.0$ there's a clear separation between the graphs which appear to be fourth order convergent up to that point. However, when $t \approx 7.0$ the graphs on the two finest grids begin to overlap. Beyond this point in time the graphs are nearly identical. As a consequence the convergence rate (4.18) is nearly zero on the two finest grids.

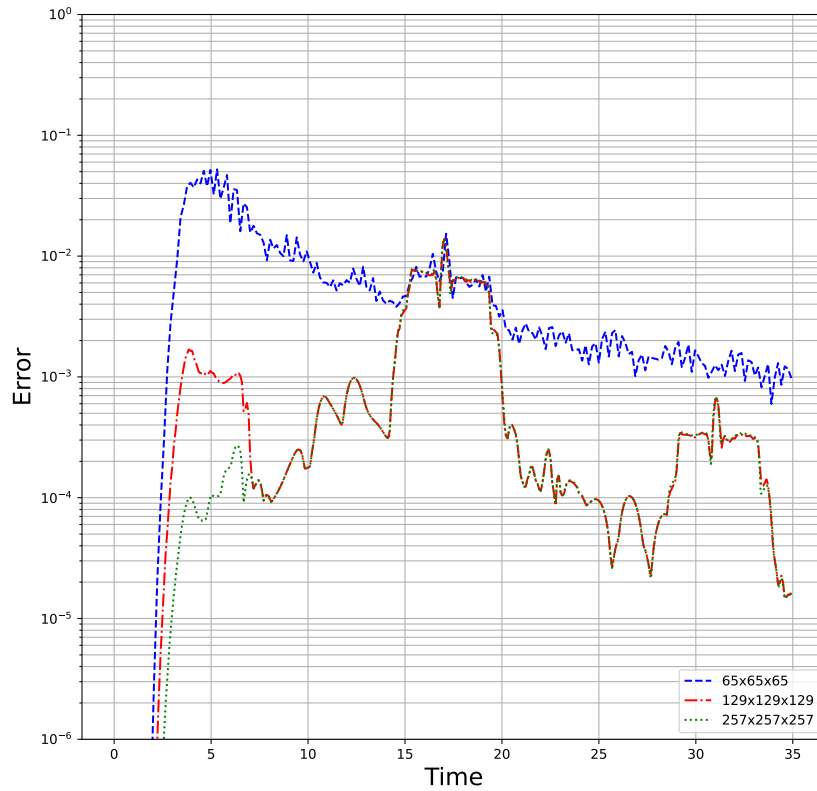


Figure 4.3: Plots of the error history for Test Solution 1 (page 90) when $D_{\text{vac}} = [-2.0, 2.0]^3$ and the sponge thickness $\ell = 5.0$.

There is a delicate balancing act that needs to be considered when trying to demonstrate fourth order accuracy. On one hand, we should choose a sufficiently thick sponge layer to guarantee that $|\tilde{E}^{\text{Sponge}}| \ll |\tilde{E}^h|$ where h is the grid size of our finest

grid. If the sponge layer is sufficiently thick

$$\log \left(E^{(2h,\ell)} / E^{(h,\ell)} \right) / \log 2 \approx 4.$$

However there is a penalty making the sponge layer too thick. Suppose the vacuum region D_{vac} is fixed and we discretize the computational domain using an $N \times N \times N$ grid on our finest grid. If we increase the sponge layer thickness beyond what is necessary to produce fourth order convergence, the diameter of the computational domain concomitantly increases the discretization error. We will need to experiment with the sponge layer thickness to strike the right balance. Table 4.1 and 4.2 demonstrate fourth order accuracy for the test problems.

Table 4.1: Error of Test Solution 1 (page 90) where $D_{\text{vac}} = [-2, 2]^3$, the sponge thickness $\ell = \frac{19}{2}$, and the terminal time $T = 35$.

grid	error	rate	avg # MGCYC
$65 \times 65 \times 65$	7.145e-01	—	4.81
$129 \times 129 \times 129$	1.526e-02	5.55	3.99
$257 \times 257 \times 257$	9.477e-04	4.01	3.79

4.2 High Order Non-Reflective Boundary Condition

In this section, we will discuss the truncated exterior problem (4.2). To be more specific, in Section 4.2.1 we present the discretization of (4.2) in time by means of the θ -scheme [23, 68]. It produces a one parameter family of elliptic PDEs which require only three levels in time with an artificial boundary condition (Section 1.2.2) imposed on the

Table 4.2: Error of Test Solution 2 (page 90) where $D_{\text{vac}} = [-2, 2]^3$, the sponge thickness $\ell = \frac{17}{2}$, and the terminal time $t = 35$.

grid	error	rate	avg # MGCYC
$65 \times 65 \times 65$	3.935e-01	—	4.17
$129 \times 129 \times 129$	3.179e-02	3.63	3.76
$257 \times 257 \times 257$	6.992e-04	5.51	3.39

boundary of the spherical domain. In Section 4.2.2, we discuss how to solve the aforementioned elliptic PDE using the method of difference potentials. Finally, Section 4.2.3 shows that if the order of the artificial boundary condition is sufficiently high our simulations are fourth order accurate.

4.2.1 Semi Discrete Approximation in Time

When applying the θ -scheme [23, 68] to (4.2) we obtain the modified Helmholtz equation on the upper time level subject to the chosen ABC at the outer boundary:

$$\begin{aligned}\Delta u^{n+1} - \kappa^2 u^{n+1} &= f^{n+1}, & \mathbf{x} \in \Omega, \\ B_p u &= 0, & \mathbf{x} \in \Gamma,\end{aligned}\tag{4.20}$$

where the wavenumber $\kappa^2(\mathbf{x})$ is defined in (2.6) and the RHS f^{n+1} is defined recursively in (2.8a) (or (2.8b)). Section 2.1 gives the details on how the modified Helmholtz equation was derived. The NRBC $B_p u = 0$ is given by (1.10a) - (1.10b). In the subsequent section, we will discuss how to solve the elliptic boundary value problem (4.20) with fourth order accuracy in space using the method of difference potentials.

4.2.2 Advancing the time marching scheme with MDP

In this section, we solve the boundary value problem (4.20) using the MDP (see Section 3.2 for detail). The method of difference potentials first embeds Ω into a simple auxiliary domain and construct an auxiliary problem which coincides with (4.20) on Ω . By solving the AP, we compute difference potentials that are the discrete counterparts of Calderón's potentials. The discrete solution to (4.20) on the grid boundary γ (a fringe of nodes around the continuous boundary Γ) satisfies the inhomogeneous boundary equation with projection. On the other hand, it can be represented with the affine operator known as the extension operator. Substituting the spectral representation of the extension operator into the inhomogeneous boundary equation with projection and the artificial boundary condition, can solve the BEP and obtain the discrete solution on γ . Once it is known, the overall solution of (4.20) is obtained in the form of a difference potential.

First, we will consider a continuous auxiliary problem

$$\begin{aligned}\Delta w^{n+1} - \kappa^2(\mathbf{x})w^{n+1} &= g^{n+1}, & \mathbf{x} \in \Omega^0, \\ w^{n+1} &= 0, & \mathbf{x} \in \Gamma^0,\end{aligned}\tag{4.21}$$

where Ω^0 is a cube which contains Ω and g^{n+1} is an arbitrary right-hand side function on the upper time level. In order to solve (4.20) using the MDP, we need the capacity to solve the AP (4.21) for a number of different RHSs, not just the RHS term which comes from (4.20). The discrete counterpart to the auxiliary problem (4.21) is given by

$$\begin{aligned}\mathbf{L}_h[\kappa^2]w^{n+1} &= g^{n+1}, & \mathbf{x}_h \in \Omega_h^0, \\ w^{n+1} &= 0, & \mathbf{x}_h \in \Gamma_h^0,\end{aligned}$$

where the LHS operator of the fourth order compact scheme is defined in (2.25) and Ω_h^0 (Γ_h^0) is the discretization grid on Ω^0 (Γ^0). The discrete solution to (4.20) is obtained with the help of Theorem 3.2.1. First, we represent the unknown discrete density u_γ^{n+1} using the extension operator derived in Section 3.2.4. Then, we solve the discrete BEP (3.7) to find the density u_γ^{n+1} and employ the generalized Green's formula (3.8) to compute the solution $u_{\mathbb{N}^+}^{n+1}$ once the density $u_\gamma^{n+1} = \mathbf{Tr}_\gamma u_{\mathbb{N}^+}^{n+1}$ is known.

The domain Ω of problem (4.2) is chosen so that the source term F is compactly supported on Ω . Therefore, with no loss of generality we can assume that the source term vanishes in the vicinity of Γ . In addition, there exists a ball contained in Ω such that the propagation speed is constant on its compliment. Hence, there exists $c_\infty > 0$ such that $c(\mathbf{x}) = c_\infty$ for all $\mathbf{x} \in \Gamma$. If we follow the same approach as Section 3.2.4 (assuming the speed is constant and the source term is zero near Γ), then the extension operator satisfies

$$\mathbf{E}\mathbf{x}\boldsymbol{\zeta}_\Gamma^{n+1} = \mathbf{E}\mathbf{x}_H\boldsymbol{\zeta}_\Gamma^{n+1} + \mathbf{E}\mathbf{x}_I^{n+1},\tag{4.22}$$

where the linear portion of the affine operator (4.22) can be written as follows

$$\mathbf{E}\mathbf{x}_H\boldsymbol{\zeta}_\Gamma^{n+1} = \mathbf{A}_0\mathbf{c}_0^{n+1} + \mathbf{A}_1\mathbf{c}_1^{n+1}.\tag{4.23}$$

For the matrices \mathbf{A}_0 and \mathbf{A}_1 in (4.23) we have

$$\mathbf{A}_i = \left[\mathbf{E}x_H \boldsymbol{\psi}_{0,0}^{(i)} \quad \mathbf{E}x_H \boldsymbol{\psi}_{1,-1}^{(i)} \quad \mathbf{E}x_H \boldsymbol{\psi}_{1,0}^{(i)} \quad \mathbf{E}x_H \boldsymbol{\psi}_{1,1}^{(i)} \quad \cdots \quad \mathbf{E}x_H \boldsymbol{\psi}_{L,L}^{(i)} \right], \quad i \in \{0,1\} \quad (4.24)$$

where the columns are given by

$$\begin{aligned} \mathbf{E}x_H \boldsymbol{\psi}_{lm}^{(0)} &= \left[1 + \frac{\varrho^2}{2} \left(\frac{d_0^{n+1}}{c_\infty^2} + \frac{l(l+1)}{r^2} \right) - \frac{\varrho^3}{6} \left(\frac{2d_0^{n+1}}{c_\infty^2 r} + \frac{4l(l+1)}{r^3} \right) \right. \\ &\quad \left. + \frac{\varrho^4}{24} \left(d_0^{n+1} \left(\frac{8+2l(l+1)}{c_\infty^2 r^2} \right) + \frac{\tilde{d}_0^{n+1}}{c_\infty^4} + \frac{l^2(l+1)^2 + 18l(l+1)}{r^4} \right) \right] \boldsymbol{\psi}_{lm}^{(0)}, \\ \mathbf{E}x_H \boldsymbol{\psi}_{lm}^{(1)} &= \varrho + \frac{\varrho^2}{r} + \frac{\varrho^3}{6} \left(\frac{d_1^{n+1}}{c_\infty^2} + \frac{6+l(l+1)}{r^2} \right) - \frac{\varrho^4}{24} \left(\frac{4d_1^{n+1}}{c_\infty^2 r} + \frac{8l(l+1)+24}{r^3} \right) \boldsymbol{\psi}_{lm}^{(1)}, \end{aligned}$$

and the vectors of Fourier coefficients c_0^{n+1} , c_1^{n+1} are introduced in (3.25). The inhomogeneous term of the extension operator (4.22) is given by

$$\begin{aligned} \mathbf{E}x_I^{n+1} &= \sum_{l=0}^L \sum_{m=-l}^l \left\{ \left[\frac{\varrho^2}{2c_\infty^2} - \frac{\varrho^3}{3c_\infty^2 r} + \frac{\varrho^4}{24} \left(\frac{8+2l(l+1)}{c_\infty^2 r^2} \right) \right] \boldsymbol{\psi}_{lm}^{(0)} \sum_{j=0}^{J_0} d_0^{n-j} c_{lm}^{(0,n-j)} \right. \\ &\quad \left. + \left[\frac{\varrho^3}{6c_\infty^2} - \frac{\varrho^4}{6c_\infty^2 r} \right] \boldsymbol{\psi}_{lm}^{(1)} \sum_{j=0}^{J_1} d_1^{n-j} c_{lm}^{(1,n-j)} + \frac{\varrho^4}{24c_\infty^2} \boldsymbol{\psi}_{lm}^{(0)} \left(\sum_{j=0}^{\tilde{J}_0} \tilde{d}_0^{n-j} c_{lm}^{(0,n-j)} \right) \right\}. \quad (4.25) \end{aligned}$$

Using the extension operator (4.22), we can represent the discrete density as $u_\gamma^{n+1} = \mathbf{E}x \boldsymbol{\zeta}_\Gamma^{n+1}$, where $\boldsymbol{\zeta}_\Gamma^{n+1}$ is given by the truncated series (3.20) with the coefficients c_0^{n+1} , c_1^{n+1} .

We know the discrete density must satisfy the inhomogeneous BEP (3.7). Therefore, substituting $u_\gamma^{n+1} = \mathbf{E}x \boldsymbol{\zeta}_\Gamma^{n+1}$ into (3.7), we have

$$\mathbf{Q}_0 c_0^{n+1} + \mathbf{Q}_1 c_1^{n+1} = -\text{Tr}_\gamma \mathbf{G}_h \tilde{f}_R^{n+1} - \mathbf{q}_I^{n+1}, \quad (4.26)$$

where

$$\mathbf{Q}_i = (\mathbf{P}_\gamma - \mathbf{I}_\gamma) \mathbf{A}_i \in \mathbb{C}^{|\gamma| \times (1+L)^2}, \quad i \in \{0,1\}, \quad (4.27a)$$

$$\mathbf{q}_I^{n+1} = (\mathbf{P}_\gamma - \mathbf{I}_\gamma) \mathbf{E}x_I^{n+1} \in \mathbb{C}^{|\gamma|}. \quad (4.27b)$$

The matrices $\mathbf{A}_i \in \mathbb{C}^{|\gamma| \times (1+L)^2}$ for $i \in \{0,1\}$ are defined in (4.24) and the inhomoge-

neous term $\mathbf{E}x_l^{n+1}$ is defined in (4.25). In order to determine the Fourier coefficients c_0^{n+1} , c_1^{n+1} we will supplement (4.26) with the high order NRBC. Substituting the spectral representation

$$v_j = \sum_{l=1}^{\infty} \sum_{m=-l}^l v_{lm}^{(j)} Y_l^m(\theta, \varphi),$$

into the p^{th} order NRBC (1.10a) - (1.10b), we obtain

$$\frac{1}{c_{\infty}} \frac{\partial u}{\partial t} + \frac{\partial u}{\partial r} + \frac{u}{R} = \sum_{l=1}^{\infty} \sum_{m=-l}^l (v_{lm} \cdot e_1) Y_l^m(\theta, \varphi), \quad (4.28a)$$

$$\frac{\partial v_{lm}}{\partial t} = \mathbf{B}_l v_{lm} - \frac{l(l+1)c_{\infty}}{2R^2} \left\langle u, Y_l^m \right\rangle e_1, \quad (4.28b)$$

where each \mathbf{B}_l is a tridiagonal matrix

$$\mathbf{B}_l = \begin{pmatrix} -\frac{1}{c_{\infty}R} & 1 & 0 & 0 & \cdots & 0 \\ \frac{2(1-l(l+1))}{4R^2} & -\frac{2}{c_{\infty}R} & 1 & 0 & \cdots & 0 \\ \vdots & & \ddots & & & \vdots \\ 0 & \cdots & 0 & \frac{(p-1)(p-2)-l(l+1)}{4R^2} & -\frac{(p-1)}{c_{\infty}R} & 1 \\ 0 & \cdots & & 0 & \frac{p(p-1)-l(l+1)}{4R^2} & -\frac{p}{c_{\infty}R} \end{pmatrix} \in \mathbb{R}^{p \times p}, \quad (4.29)$$

the vector of auxiliary variables is

$$v_{lm} = [v_{lm}^{(1)}, v_{lm}^{(2)}, \dots, v_{lm}^{(p)}]^T \in \mathbb{C}^p, \quad (4.30)$$

the first canonical basis vector is $e_1 = [1, 0, \dots, 0]^T \in \mathbb{R}^p$, and the weighted inner product $\langle \cdot, \cdot \rangle$ is defined in (B.1).

We would like to rewrite (4.28a) - (4.28b) completely in terms of the spherical harmonics. To do this, we will approximate the first order derivatives in time with an implicit multistep method on the upper time level and subsequently replace the trace with its spectral representation. Then, we will exploit the fact that the spherical harmonics are orthogonal to simplify the final expression. Specifically, we will discretize (4.28a) - (4.28b) in time using the implicit linear multistep method known as backward differentiation formula of order q (BDF q) which approximates

the ODE $\frac{dw}{dt} = g$ and is written as

$$w^{n+1} + \sum_{i=1}^q a_i w^{n+1-i} = \tau b_0 g^{n+1}. \quad (4.31)$$

Applying (4.31) to (4.28a) - (4.28b), we arrive at

$$\begin{aligned} -\sum_{i=1}^q a_i u^{n+1-i} &= \left(1 + \frac{\tau b_0 c_\infty}{R}\right) u^{n+1} + \tau b_0 c_\infty \left(\frac{\partial u^{n+1}}{\partial r} - \sum_{l=1}^{\infty} \sum_{m=-l}^l (\mathbf{v}_{lm}^{n+1} \cdot \mathbf{e}_1) Y_l^m(\theta, \varphi) \right), \\ -\sum_{i=1}^q a_i \mathbf{v}_{lm}^{n+1-i} &= (\mathbf{I}_{p \times p} - \tau b_0 \mathbf{B}_l) \mathbf{v}_{lm}^{n+1} + \frac{\tau b_0 l(l+1)c_\infty}{2R^2} \langle u^{n+1}, Y_l^m \rangle \mathbf{e}_1. \end{aligned}$$

Substituting the spectral representations

$$u^n = \sum_{l=0}^{\infty} \sum_{m=-l}^l c_{lm}^{(0,n)} Y_l^m(\theta, \varphi) \quad \frac{\partial u^n}{\partial r} = \sum_{l=0}^{\infty} \sum_{m=-l}^l c_{lm}^{(1,n)} Y_l^m(\theta, \varphi),$$

into the above then taking the inner product with $Y_{l'}^{m'}$ yields

$$-\sum_{i=1}^q a_i c_{l'm'}^{(0,n+1-i)} = \left(1 + \frac{\tau b_0 c_\infty}{R}\right) c_{l'm'}^{(0,n+1)} + \tau b_0 c_\infty c_{l'm'}^{(1,n+1)} - \tau b_0 c_\infty (1 - \delta_{l'0}) (\mathbf{v}_{l'm'}^{n+1} \cdot \mathbf{e}_1),$$

for $l' = 0, 1, 2, \dots$ and $m' = -l', \dots, l'$. Then, (4.28a) - (4.28b) can be approximated with

$$-\sum_{i=1}^q a_i c_{lm}^{(0,n+1-i)} = \left(1 + \frac{\tau b_0 c_\infty}{R}\right) c_{lm}^{(0,n+1)} + \tau b_0 c_\infty c_{lm}^{(1,n+1)} - \tau b_0 c_\infty (1 - \delta_{l0}) (\mathbf{v}_{lm}^{n+1} \cdot \mathbf{e}_1), \quad (4.33a)$$

$$-\sum_{i=1}^q a_i \mathbf{v}_{lm}^{n+1-i} = (\mathbf{I}_{p \times p} - \tau b_0 \mathbf{B}_l) \mathbf{v}_{lm}^{n+1} + \frac{\tau b_0 l(l+1)c_\infty}{2R^2} c_{lm}^{(0,n+1)} \mathbf{e}_1, \quad (4.33b)$$

where $l = 0, 1, 2, \dots$ and $m = -l, \dots, l$. Finally we can combine (4.33a) - (4.33b) to obtain

$$-\sum_{i=1}^q a_i c_{0,0}^{(0,n+1-i)} = \left(1 + \frac{\tau c_\infty b_0}{R}\right) c_{0,0}^{(0,n+1)} + \tau c_\infty b_0 c_{0,0}^{(1,n+1)}, \quad (l, m) = (0, 0), \quad (4.34a)$$

$$-\sum_{i=1}^q a_i \tilde{\mathbf{v}}_{lm}^{n+1-i} = \tilde{\mathbf{B}}_l \tilde{\mathbf{v}}_{lm}^{n+1} + \tau c_\infty b_0 c_{lm}^{(1,n+1)} \tilde{\mathbf{e}}_1, \quad l = 1, 2, \dots, m = -l, \dots, l, \quad (4.34b)$$

where

$$\tilde{\mathbf{B}}_l = \left(\begin{array}{c|c} 1 + \frac{\tau b_0 c_\infty}{R} & -\tau b_0 c_\infty \mathbf{e}_1^T \\ \hline \frac{\tau b_0 c_\infty l(l+1)}{2R^2} \mathbf{e}_1 & \mathbf{I}_{p \times p} - \tau b_0 \mathbf{B}_l \end{array} \right) \in \mathbb{R}^{p+1 \times p+1}, \quad (4.35)$$

is a tridiagonal matrix where \mathbf{B}_l (def. (4.29)) is a $p \times p$ real tridiagonal matrix, $\mathbf{I}_{p \times p}$ is the identity matrix of rank p , the canonical unit vector $\tilde{\mathbf{e}}_1 = [1, 0, \dots, 0]^T \in \mathbb{R}^{p+1}$, and

$$\tilde{\mathbf{v}}_{lm}^{n+1} = \begin{pmatrix} c_{lm}^{(0,n+1)} \\ \mathbf{v}_{lm}^{n+1} \end{pmatrix},$$

where the auxiliary variables v_{lm} are defined in (4.30). We will only consider the Fourier coefficients associated with the indices (l, m) for $l = 0, 1, \dots, L$ and $m = -l, \dots, l$. For numerical simulations, we assume that $v_{0,0}^{(j)} = 0$ for $j = 1, 2, \dots, p$ on every time level. There are three sets of Fourier coefficients that we need to keep track of: the Fourier coefficients of the Dirichlet data, $c_{0,0}^{n+1}$, the Fourier coefficients of the Neumann data, c_1^{n+1} , and the Fourier coefficients of the auxiliary variables, \mathbf{v}_{lm}^{n+1} , for $l = 1, \dots, L$ and $m = -l, \dots, l$. However, a simple rearrangement of (4.34a) - (4.34b) can eliminate the auxiliary variables on the upper time level from the Dirichlet and Neumann coefficients on the upper time level. As a consequence (4.34a) - (4.34b) can be rearranged to produce

$$-\sum_{i=1}^q \frac{a_i c_{0,0}^{(0,n+1-i)}}{1 + \tau c_\infty b_0 / R} = c_{0,0}^{(0,n+1)} + \frac{\tau c_\infty b_0}{1 + \tau c_\infty b_0 / R} c_{0,0}^{(1,n+1)}, \quad (l, m) = (0, 0), \quad (4.36a)$$

$$-\tilde{\mathbf{B}}_l^{-1} \left(\sum_{i=1}^q a_i \tilde{\mathbf{v}}_{lm}^{n+1-i} \right) = \tilde{\mathbf{v}}_{lm}^{n+1} + \tau c_\infty b_0 c_{lm}^{(1,n+1)} \tilde{\mathbf{B}}_l^{-1} \tilde{\mathbf{e}}_1, \quad l = 1, \dots, L, m = -l, \dots, l. \quad (4.36b)$$

Notice how (4.36a) and the first block component of (4.36b) only depend on the Fourier coefficients of the Dirichlet and Neumann data on the upper time level, while the RHS terms are composed of known quantities from previous time levels. We will use this to construct a condition which resembles of Robin boundary condition. If we take (4.36a) and first component of (4.36b), it produces the "Robin-like" boundary

condition

$$\mathbf{M}_0 \mathbf{c}_0^{n+1} + \mathbf{M}_1 \mathbf{c}_1^{n+1} = \mathbf{c}_{\text{NRBC}}^{n+1}, \quad (4.37)$$

where \mathbf{c}_0^{n+1} and \mathbf{c}_1^{n+1} are defined in (3.25), the matrices \mathbf{M}_0 and \mathbf{M}_1 are diagonal, and $\mathbf{c}_{\text{NRBC}}^{n+1}$ contains known Fourier coefficients from previous time steps. Solving (4.37) for \mathbf{c}_0^{n+1} and substituting the expression into (4.26), we obtain

$$\left(\mathbf{Q}_1 - \mathbf{Q}_0 \mathbf{M}_0^{-1} \mathbf{M}_1 \right) \mathbf{c}_1^{n+1} = -\mathbf{Q}_0 \mathbf{M}_0^{-1} \mathbf{c}_{\text{NRBC}}^{n+1} - \text{Tr}_\gamma \mathbf{G}_h \tilde{f}_R^{n+1} - \mathbf{q}_I^{n+1}, \quad (4.38)$$

where the matrices $\mathbf{Q}_0, \mathbf{Q}_1 \in \mathbb{C}^{|\gamma| \times (1+L)^2}$ are defined in (4.27a), the vector \mathbf{q}_I^{n+1} is defined in (4.27b), the RHS term \tilde{f}_R^{n+1} is defined in (3.6), and the solution operator, \mathbf{G}_h , is defined in (3.4). Since the total number of columns $(1+L)^2 \ll |\gamma|$, we can solve the over-determined system for \mathbf{c}_1^{n+1} using QR factorization of the LHS matrix of (4.38). Then we can compute the Dirichlet Fourier coefficients \mathbf{c}_0^{n+1} with (4.37). Finally, we can compute the Fourier coefficients of the auxiliary variable v_{lm}^{n+1} for $l = 1, \dots, L$ and $m = -l, \dots, l$ with (4.34b). Once the Fourier coefficients are obtained, we can compute the density $u_\gamma^{n+1} = \mathbf{E} \mathbf{x} \boldsymbol{\xi}_\Gamma^{n+1}$ using the extension operator (4.22), then substitute the result into the generalized Green's formula (3.8) to solve the discrete modified Helmholtz equation at every time step. The proposed computational procedure is summarized in Algorithms 9, 10, and 11.

4.2.3 Numerical Simulations with NRBC

In this section, we show that the exterior problem (1.4) truncated with the NRBC(p) given by (1.10a) - (1.10b) can be solved with fourth order accuracy using the MDP. We will measure the error of our scheme by means of the infinity norm

$$\|u - u_h\|_\infty = \max_n \max_{(x_i, y_j, z_k) \in \mathbb{M}^+} |u(x_i, y_j, z_k, t^n) - u_h(x_i, y_j, z_k, t^n)|,$$

where u is a smooth solution to the exterior problem (1.4) and u_h is a discrete solution to (4.2) with high order NRBC(p) of (1.10a) - (1.10b) on a uniform grid with spatial

Algorithm 9 Preprocessing phase of the full time marching scheme for solving (4.2).

- 1: **function** PREPROCESSINGNRBC($\bar{x}_l, \bar{x}_r, \ell, c_{\max}, c_{\infty}, L, q, p$)
 - 2: $N = 2^\ell - 1$ and the uniform step size $h = (\bar{x}_r - \bar{x}_l)/N + 1$.
 - 3: Compute the uniform time step τ using the CFL number 2.32.
 - 4: Create structure associated with the FSHT.
 - 5: Create structure associated with the complex valued multigrid with ℓ levels.
 - 6: Store the grid sets $\mathbb{N}^0, \mathbb{M}^0, \mathbb{N}^\pm, \mathbb{M}^\pm, \gamma, \gamma^\pm, \gamma_{\text{proj}}$ (def. (3.2.1)) assuming $\Omega^0 = [\bar{x}_l, \bar{x}_r]^3$.
 - 7: Store the spherical harmonics $(Y_l^m(\theta, \varphi))_{0 \leq l \leq L, |m| \leq l}$ for every node in γ_{proj} .
 - 8: Store the matrices $\mathbf{A}_0, \mathbf{A}_1$ (def. (4.24)).
 - 9: Store the matrices needed to construct $\mathbf{E}\mathbf{x}_l^{n+1}$ (def. (4.25)).
 - 10: Store $\mathbf{Q}_0, \mathbf{Q}_1$ (def. (4.27a))
 - 11: Precompute the tridiagonal matrices $\tilde{\mathbf{B}}_l$ (4.35) for $l = 0, \dots, L$ assuming BDF q .
 - 12: Store the diagonal matrices \mathbf{M}_0 and \mathbf{M}_1 (4.37).
 - 13: Compute the QR factorization of $(\mathbf{Q}_1 - \mathbf{Q}_0\mathbf{M}_0^{-1}\mathbf{M}_1)$
-

Algorithm 10 Initialization phase of the full time marching scheme for solving (4.2).

- 1: **function** INITIALIZENRBC($c(\mathbf{x}), \mathbb{N}^+, \mathbb{M}^+, \gamma^+, \gamma_{\text{proj}}$)
 - 2: For each $\mathbf{x}_h \in \mathbb{N}^+$ let $u^0 = 0$ and $u^1 = 0$.
 - 3: For each $\mathbf{x}_h \in \mathbb{M}^+$ let $f_R^0 = 0$ and $f_R^1 = 0$. u^1 .
 - 4: For each $\mathbf{x}_h \in \mathbb{N}^+$ store the speed $c(\mathbf{x}_h)$.
 - 5: Compute $n_\Gamma = \max(q + 1, J_0 + 2, J_1 + 2, \tilde{J}_0 + 2, \tilde{J}_1 + 2)$
 - 6: Set the Fourier coefficients $\mathbf{0} = \mathbf{c}_0^n = \mathbf{c}_1^n$ for $n = 1, 0, -1, \dots, -(n_\Gamma - 2)$.
 - 7: Set the Fourier coefficients $\mathbf{0} = \mathbf{v}_{lm}^n$ for $n = 1, 0, -1, \dots, -(n_\Gamma - 2)$
-

size h and time step τ . The rate of convergence is defined as in (4.18):

$$\text{rate} = \log \left(\frac{\|u - u_{2h}\|_\infty}{\|u - u_h\|_\infty} \right) / \log(2).$$

We will demonstrate the performance of the algorithm by solving the wave equation subject to the homogeneous initial conditions. In the case of a constant propagation

Algorithm 11 Advancement portion of the full time marching scheme for solving (4.2).

- 1: **function** ADVANCEFOCS($h, \tau, t^{n+1}, T, \mathbb{N}^+, \mathbb{M}^+, \gamma$)
 - 2: For each $\mathbf{x}_h \in \mathbb{N}^+$ compute $g^{n+1} = -\frac{144u^n}{\tau^2 c^2} - \frac{1}{c^2}(F^{n+1} + 10F^n + F^{n-1})$.
 - 3: For each $\mathbf{x}_h \in \mathbb{M}^+$ apply the RHS operator i.e. $g_R^{n+1} = h^2 \mathbf{R}_h g^{n+1}$.
 - 4: Assemble the recursive RHS $\tilde{f}_R^{n+1} = -10\tilde{f}_R^n - \tilde{f}_R^{n-1} + g_R^{n+1}$ on \mathbb{M}^+ .
 - 5: Compute $\mathbf{G}_h \tilde{f}_R^{n+1}$ using the initial guess $\tilde{u}^{n+1} = 2u^n - u^{n-1} + \tau^2(c^2(\mathbf{x})\Delta_h u^n + F^n)$.
 - 6: Compute $\mathbf{E}\mathbf{x}_I^{n+1}$ and $\mathbf{q}_I^{n+1} = (\mathbf{P}_\gamma - \mathbf{I}_\gamma)\mathbf{E}\mathbf{x}_I^{n+1}$
 - 7: Assemble the Fourier coefficients $\mathbf{c}_{\text{NRBC}}^{n+1}$
 - 8: solve $(\mathbf{Q}_1 - \mathbf{Q}_0 \mathbf{M}_0^{-1} \mathbf{M}_1) \mathbf{c}_1^{n+1} = -\mathbf{Q}_0 \mathbf{M}_0^{-1} \mathbf{c}_{\text{NRBC}}^{n+1} - \text{Tr}_\gamma \mathbf{G}_h \tilde{f}_R^{n+1} - \mathbf{q}_I^{n+1}$ with QR factorization.
 - 9: Compute \mathbf{c}_0^{n+1} knowing $\mathbf{c}_{\text{NRBC}}^{n+1} = \mathbf{M}_0 \mathbf{c}_0^{n+1} + \mathbf{M}_1 \mathbf{c}_1^{n+1}$
 - 10: Compute the density $u_\gamma^{n+1} = \mathbf{E}\mathbf{x}\boldsymbol{\zeta}^{n+1}$ with $\mathbf{c}_0^{n+1}, \mathbf{c}_1^{n+1}$, and $\mathbf{E}\mathbf{x}_I^{n+1}$.
 - 11: Compute the solution $u_{\mathbb{N}^+}^{n+1} = \mathbf{P}_{\mathbb{N}^+} u_\gamma^{n+1} + \mathbf{G}_h \tilde{f}_R^{n+1}|_{\mathbb{N}^+}$.
 - 12: **if** $t^{n+1} < T$ **then**
 - 13: $t^{n+1} = t^{n+1} + \tau$.
 - 14: For every $\mathbf{x}_h \in \mathbb{N}^+$ $u^{n-1} = u^n, u^n = u^{n+1}$.
 - 15: For every $\mathbf{x}_h \in \mathbb{M}^+$ $\tilde{f}_R^{n-1} = \tilde{f}_R^n, \tilde{f}_R^n = \tilde{f}_R^{n+1}$.
 - 16: Reindex the Fourier coefficients in a similar manner
 - 17: **else**
 - 18: STOP the scheme.
-

speed we have:

$$\begin{aligned}
\frac{\partial^2 u}{\partial t^2} - \Delta u &= F(\mathbf{x}, t), \quad (\mathbf{x}, t) \in \mathbb{R}^3 \times (0, \infty), \\
u(\mathbf{x}, 0) &= 0, \quad \mathbf{x} \in \mathbb{R}^3, \\
\frac{\partial u}{\partial t}(\mathbf{x}, 0) &= 0, \quad \mathbf{x} \in \mathbb{R}^3,
\end{aligned} \tag{4.39}$$

The following three test solutions for problem (4.39) will be used.

Test Solution 1. The solution $u = u_{7,1.5}^{\text{Test}}$ (see formula (A.3)) and source term $F = F_{7,1.5}^{\text{Test}}$ (see formula (A.5)) are generated by the wavelet $S(t) = 5(1 - 12t^2)e^{-6t^2}$ centered at the origin $(x_0, y_0, z_0) = (0, 0, 0)$ with the translation $t_0 = 3$. Since the test solution is radially symmetric and centered at the origin, the direction of propagation is normal

to the spherical artificial boundary. This is the best case scenario for an absorbing boundary condition. We take Ω to be the ball of radius 1.5 centered at the origin and the auxiliary domain is a cube $[-2, 2]^3$.

Test Solution 2. The solution $u = u_{7,1.0}^{\text{Test}}$ (see formula (A.3)) and source term $F = F_{7,1.0}^{\text{Test}}$ (see formula (A.5)) are generated by the sinusoidal pulse $S(t) = 3 \sin(8t)e^{-6t^2}$ centered at $(x_0, y_0, z_0) = \left(\frac{15}{100}, \frac{15}{100}, \frac{15}{100}\right)$ with the translation $t_0 = 4.0$. This test problem is more demanding than Test Solution 1 since the solution is not centered at the origin. As a consequence, the direction of propagation is not always normal to the spherical artificial boundary and the absorption may be weaker. In addition, the current test solution is more oscillatory than than Test Solution 1. We take Ω to be a ball of radius 1.5 centered at the origin and the auxiliary domain is a cube $[-2, 2]^3$.

Test Solution 3. The solution $u = \frac{\partial^2 u_{12,75}^{\text{Test}}}{\partial x \partial y}$ (see formula (A.3)) and source term $F = \frac{\partial^2 F_{12,75}^{\text{Test}}}{\partial x \partial y}$ (see formula (A.5)) are generated by the function

$$S(t) = \begin{cases} \sin^{11}\left(\frac{\pi t}{5}\right) + \frac{1}{\sqrt{3}} \sin^{11}\left(\frac{\pi t}{5\sqrt{2}}\right) & t > 0 \\ 0 & t \leq 0 \end{cases}, \quad (4.40)$$

centered about the point $(x_0, y_0, z_0) = \left(\frac{1}{2}, 0, \frac{1}{4}\right)$ with the translation $t_0 = 0.20$. This test problem was deliberately chosen to produce additional spurious reflections. Differentiating (A.3) and (A.5) and translating the center (x_0, y_0, z_0) away from the origin creates asymmetries which makes the absorbing boundary less effective. In addition, the function $S(t)$ of (4.40) does not vanish as $t \rightarrow \infty$ and is not periodic in time. As a consequence the source term provides continuous output in time once it "activates." We take Ω to be a ball of radius 1.5 centered at the origin and the auxiliary domain is a cube $[-2, 2]^3$.

Test Solution 4. Here, we consider a variable-coefficient wave equation:

$$\begin{aligned} \frac{\partial^2 u}{\partial t^2} - c^2(\mathbf{x})\Delta u &= F(\mathbf{x}, t), \quad (\mathbf{x}, t) \in \mathbb{R}^3 \times (0, \infty), \\ u(\mathbf{x}, 0) &= 0, \quad \mathbf{x} \in \mathbb{R}^3, \\ \frac{\partial u}{\partial t}(\mathbf{x}, 0) &= 0, \quad \mathbf{x} \in \mathbb{R}^3, \end{aligned} \tag{4.41}$$

where the propagation speed is given by $c^2(x, y, z) = \frac{4}{5} + \frac{1}{5}e^{-20(x^2+y^2+z^2)}$. The solution of (4.41) $u = u_{7,1.0}^{\text{Test}}$ (see formula (A.6)) and source term $F = F_{7,1.5}^{\text{Test}}$ (see formula (A.7)) are generated by the wavelet $S(t) = 3 \sin(8t)e^{-6t^2}$ centered at the origin $(x_0, y_0, z_0) = (\frac{15}{100}, \frac{15}{100}, \frac{15}{100})$ with the translation $t_0 = 3$. This is a variable speed counterpart to Test Solution 2.

Recall from the discussion in Section 1.2.2 that, there are two sources of error: the reflection error due to replacing the exterior problem (1.4) with the truncated problem (4.2) and the discretization error from approximating the truncated problem (4.2) on the grid. Suppose that the overall error of the scheme satisfies $E^{(h,p)} = \tilde{E}^{\text{NRBC}(p)} + \tilde{E}^h$ where the discretization error $\tilde{E}^h = \mathcal{O}(h^4)$ and the reflection error $\tilde{E}^{\text{NRBC}(p)} = \mathcal{O}(|\text{diam}(\Omega)|^{-2p-1})$ for a given Ω . For the discretization error we have

$$\limsup_{h \rightarrow 0} |\tilde{E}^h| = 0,$$

while for the reflection error on a given Ω we can write

$$\limsup_{p \rightarrow \infty} |\tilde{E}^{\text{NRBC}(p)}| = 0.$$

To conduct a grid refinement analysis of our test problems, we will choose a sufficiently large p so that $|\tilde{E}^{\text{NRBC}(p)}| \ll |\tilde{E}^h|$. As a consequence, $\log(|\tilde{E}^{\text{NRBC}(p)}|/|\tilde{E}^h|) / \log(2) \approx 4$ for all sufficiently small h , which implies fourth order grid convergence. However, for a given p , there exists a sufficiently fine grid size h_0 such that $|\tilde{E}^{\text{NRBC}(p)}| \approx |\tilde{E}^{h_0}|$. Hence, $E^{(h,p)} \approx E^{(h_0,p)}$ whenever $h \leq h_0$, which implies that refining the grid further does not improve the overall error. We observe this behavior in Figure 4.4. Indeed, the graphs on the top and middle plots overlap for several stretches in time. However, the bottom plot of Figure 4.4 shows fourth order convergence since the order of the ABC is sufficiently large. The main takeaway is that we should choose p sufficiently

large so that the reflection errors are much smaller than the discretization error on our finest grid.

Table 4.3 demonstrates fourth order convergence (in the sense described above) for the Test Solutions 1, 2, 3, and 4.

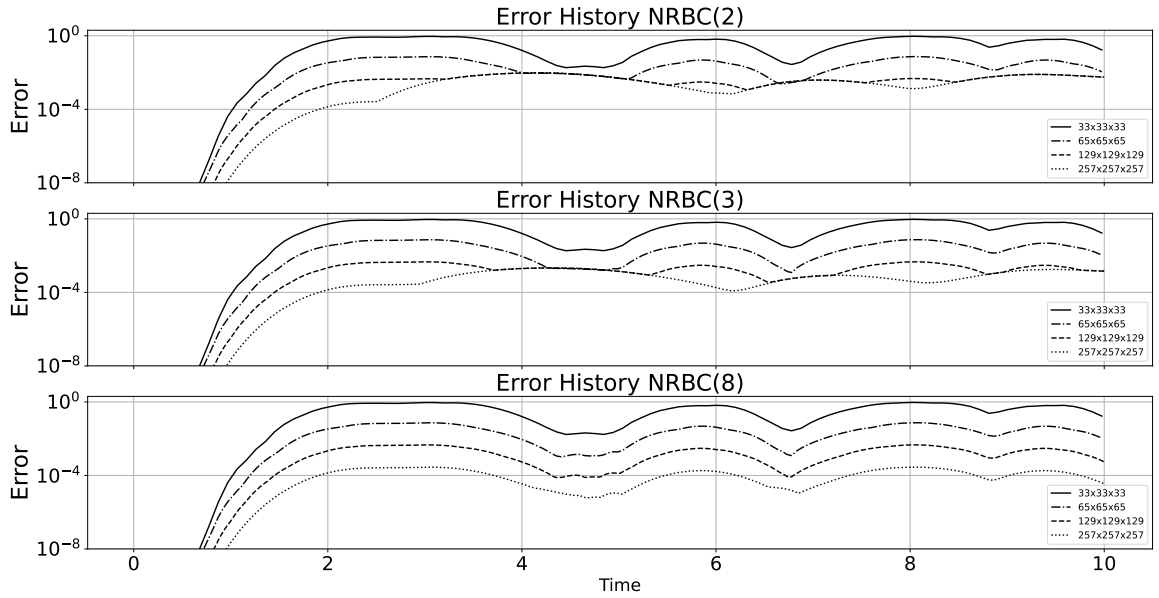


Figure 4.4: Error History for Test Solution 3 assuming $L = 25$ for several different NRBCs.

Table 4.3: Error of Test Solutions 1 – 4 when using NRBC(8). The uniform time step τ is 98% of the maximum CFL shown in (2.32) and the terminal time is $T = 10.0$. The order of the spherical harmonics expansion is $L = 25$. The setting of the multigrid method is summarized in Table 1.1.

	h	error	conv. rate	CPUTIME (sec.)		Average # MGCYCs		
				Preprocessing	Avg Solve MHE	$G_h \tilde{f}_R^{n+1}$	q_I^{n+1}	$P_{N+} u_\gamma^{n+1}$
Example 1	4/33	4.979e-01	—	1.801e+01	7.765e-02	4.30	3.91	3.85
	4/65	3.262e-02	3.93	2.676e+02	6.522e-01	3.94	3.47	3.39
	4/129	2.281e-03	3.84	3.852e+03	5.988e+00	3.66	3.25	3.21
	4/257	1.698e-04	3.75	2.089e+04	3.201e+01	3.36	2.96	2.92
Example 2	4/33	5.332e-01	—	1.802e+01	7.182e-02	3.74	3.43	3.39
	4/65	4.166e-02	3.68	3.090e+02	6.082e-01	3.40	3.07	3.07
	4/129	2.594e-03	4.01	3.345e+03	5.360e+00	3.31	2.94	2.91
	4/257	1.707e-04	3.92	2.114e+04	2.868e+01	3.09	2.70	2.69
Example 3	4/33	9.410e-01	—	1.800e+01	1.620e-01	4.64	4.47	4.51
	4/65	7.361e-02	3.68	2.775e+02	1.514e+00	4.63	4.42	4.44
	4/129	4.616e-03	4.00	3.353e+03	1.331e+02	4.64	4.40	4.41
	4/257	2.841e-04	4.02	2.099e+04	8.590e+02	4.63	4.39	4.39
Example 4	4/33	7.366e-01	—	1.904e+01	9.212e-02	3.87	3.64	3.59
	4/65	7.708e-02	3.24	2.901e+02	8.242e-01	3.99	3.53	3.52
	4/129	4.453e-03	4.11	4.144e+03	6.801e+00	3.96	3.35	3.28
	4/257	3.097e-04	3.85	2.288e+04	4.125e+01	3.61	3.21	3.05

Chapter 5

EXTERIOR SCATTERING PROBLEM

Consider the exterior problem (1.5). To solve this problem with a conventional approach such as a finite difference or finite element method, one needs to truncate the domain of (1.5) so that the computational domain becomes finite. We use a spherical artificial outer boundary for truncation. Accordingly, the truncated domain is a spherical shell. The inner boundary of the shell coincides with the scattering surface while an ABC is to be imposed on the outer boundary of the shell to absorb any outgoing wave. If the spherical shell is defined as

$$\Omega = \{\mathbf{x} \mid R_1 \leq \|\mathbf{x}\|_2 \leq R_0\}, \quad (5.1)$$

then the truncation of (1.5) yields

$$\begin{aligned} \frac{\partial^2 u}{\partial t^2} - c^2(\mathbf{x})\Delta u &= 0, \quad \mathbf{x} \in \Omega \times (0, T], \\ u(\mathbf{x}, 0) &= \varphi_0(\mathbf{x}), \quad \mathbf{x} \in \Omega, \\ \frac{\partial u}{\partial t}(\mathbf{x}, 0) &= \varphi_1(\mathbf{x}), \quad \mathbf{x} \in \Omega, \\ B_p(u) &= 0, \quad \mathbf{x} \in \Gamma_0 = \{\mathbf{x} \mid \|\mathbf{x}\|_2 = R_0\}, \\ l_{\Gamma_1}(u) &= \varphi_{\Gamma_1}(\mathbf{x}, t), \quad \mathbf{x} \in \Gamma_1 = \{\mathbf{x} \mid \|\mathbf{x}\|_2 = R_1\}, \end{aligned} \quad (5.2)$$

where the operator \mathcal{L}_{Γ_1} that specifies the boundary condition on the scattering surface has the form

$$\mathcal{L}_{\Gamma_1}(u) = \left(au + b \frac{\partial u}{\partial \mathbf{n}} \right) \Big|_{\Gamma_1}, \quad (5.3)$$

and may correspond to a Dirichlet $((a, b) = (1, 0))$, Neumann $((a, b) = (0, 1))$, or Robin $(a, b) \neq (0, 0)$ boundary condition. The relation $B_p u = 0$ is a generic p^{th} order artificial boundary condition, see Section 1.2.2. The wave propagation speed $c(\mathbf{x})$ in the exterior problem (1.5) is constant outside some bounded region. Here we assume that the radius R_0 is taken sufficiently large so that the speed is constant on Γ_0 and beyond.

5.1 Semi Discrete Approximation in Time

When applying the θ -scheme [23, 68] to (5.2), we obtain the modified Helmholtz equation on the upper time level

$$\begin{aligned} \Delta u^{n+1} - \kappa^2 u^{n+1} &= f^{n+1}, & \mathbf{x} \in \Omega, \\ B_p u^{n+1} &= 0, & \mathbf{x} \in \Gamma_0, \\ \mathcal{L}_{\Gamma_1}(u^{n+1}) &= \varphi_{\Gamma_1}(\mathbf{x}, t^{n+1}), & \mathbf{x} \in \Gamma_1, \end{aligned} \quad (5.4)$$

where Ω is the spherical shell defined in (5.1), the “wavenumber” $\kappa^2(\mathbf{x})$ is defined in (2.6), and the RHS f^{n+1} is defined recursively in (2.8a) (or (2.8b)). The operator B_p defines a p^{th} order ABC on the artificial outer boundary Γ_0 and the operator \mathcal{L}_{Γ_1} of (5.3) specifies the boundary condition on the scattering surface Γ_1 . Section 2.1 gives the details on how the modified Helmholtz equation was derived. In the subsequent section, we will discuss how to solve the elliptic boundary value problem (5.4) with fourth order accuracy in space using the method of difference potentials. In Section 5.3, we present the results of numerical simulations for the truncated scattering problem.

5.2 Solution on the upper time level by MDP

In this section, we solve the boundary value problem (5.4) using the MDP (see Section 3.2 for detail). The method of difference potentials first embeds Ω into a simple auxiliary domain where an auxiliary problem is formulated for the same governing equation as that in (5.4). By solving the AP, we compute the difference potentials that are the discrete counterparts of Calderón's potentials. The discrete solution to (5.4) on the grid boundary γ (a fringe of nodes around the continuous boundary Γ) satisfies the inhomogeneous boundary equation with projection. On the other hand, it can be represented as an extension of the boundary trace of a continuous solution (by means of an affine operator known as the extension operator). Substituting a spectral representation of the extension into the inhomogeneous boundary equation with projection and the artificial boundary condition, can solve the BEP and obtain the discrete solution on γ . Once it is known, the overall solution of (5.4) is obtained in the form of a difference potential. All of these components are described in detail in Section 3.2 where the MDP is applied to the interior problem (1.2), as well as in Section 4.2.2 where the MDP is adapted to the exterior problem (1.4). For the sake of brevity, in this section we will only emphasize the major differences between the implementation for problem (5.4) and the previous implementations.

First, we will need the auxiliary problem described in Section 3.2.1. To solve the modified Helmholtz equation (5.4), we need the capacity to solve the auxiliary problem (3.2) on a cube Ω^0 sufficiently large to contain the spherical shell Ω defined in (5.1). The discrete counterpart of the AP (3.2) is given by (3.3). The solution to (3.3) is obtained by applying the solution operator, G_h of (3.4), to the RHS term of (3.3). The next component needed are the grids sets on the auxiliary domain Ω^0 . They are given explicitly in Definition 3.2.1. The only difference is that Ω of (5.1) is a spherical shell rather a sphere. In addition, we will introduce the discrete boundaries γ_i as the nodes that straddle $\Gamma_i = \{\mathbf{x} \mid \|\mathbf{x}\|_2 = R_i\}$ for $i = 0$ or 1 . The discrete boundary of the spherical shell is $\gamma = \gamma_0 \cup \gamma_1$. We will also assume that the uniform grid h is sufficiently fine so that $\gamma_0 \cap \gamma_1 = \emptyset$. The final piece needed to solve (5.4) is the solution to the inhomogeneous boundary equation with projection (3.7). According to Theorem 3.2.1, once the trace of the solution (5.4) on the discrete boundary γ , u_γ^{n+1} , is known we can use the generalized Green's formula (3.8) to solve (5.4) on \mathbb{N}^+ (the discrete version of Ω). We shall use the extension operator to represent the

trace u_γ^{n+1} . Upon substituting the spectral form of the extension into (3.7), we obtain a linear system which can be solved in the least squares sense. This approach was taken for the interior problem (1.2) in Sections 3.2.4 and 3.2.5 and for the exterior problem (1.1.2) in Section 4.2.2. However, in those cases the continuous boundary Γ only consists of one contiguous set. For the truncated scattering problem (5.2), the continuous boundary $\Gamma = \Gamma_0 \cup \Gamma_1$ consists of two disjoint subsets. We shall spent the remainder of the section constructing the extension operator on $\gamma = \gamma_0 \cup \gamma_1$ and the resulting linear system when substituting the extension into (3.7) .

5.2.1 Extension Operator

In this section, we represent the trace of a discrete solution u_γ^{n+1} on the grid boundary $\gamma = \gamma_0 \cup \gamma_1$ of the spherical shell Ω as the extension of the trace of a continuous solution on Γ . We need to be especially careful since the boundary consists of two disjoint parts, $\Gamma = \Gamma_0 \cup \Gamma_1$ where $\Gamma_0 = \{\mathbf{x} \mid \|\mathbf{x}\|_2 = R_0\}$ and $\Gamma_1 = \{\mathbf{x} \mid \|\mathbf{x}\|_2 = R_1\}$.

We shall start with finding the extension operator about Γ_j for $j = 0$ or 1 . Since Ω given by (5.1) has spherical symmetry, we will use the spherical coordinates (r, θ, φ) where r is the radial distance from the origin, θ is the the zenith angle which varies from the north pole of the sphere to the south pole, and the azimuthal angle φ wraps around the equator. If the continuous trace is defined as $\boldsymbol{\zeta}_{\Gamma_j}^{n+1} = (u^{n+1}, \frac{\partial u}{\partial r})|_{\Gamma_j}$ for $j = 0$ or 1 , then the extension operator about Γ_j is given by the Taylor expansion

$$\mathbf{Ex}_j(\boldsymbol{\zeta}_{\Gamma_j}^{n+1}) \stackrel{\text{def}}{=} u^{n+1}|_{\tilde{\mathbf{x}}_h} + \varrho \frac{\partial u^{n+1}}{\partial r}|_{\tilde{\mathbf{x}}_h} + \sum_{i=2}^{I_{Ex}-1} \frac{\varrho^i}{i!} \frac{\partial^i u^{n+1}}{\partial r^i}|_{\tilde{\mathbf{x}}_h} + O(\varrho^{I_{Ex}}), \quad (5.5)$$

where $\mathbf{x}_h \in \gamma_j$ and $\tilde{\mathbf{x}}_h$ is the orthogonal projection of \mathbf{x}_h onto Γ_j . The quantity ϱ the signed distance: $\varrho = |\mathbf{x}_h - \tilde{\mathbf{x}}_h|$ if \mathbf{x}_h is not in the solid sphere which has Γ_j as its boundary and $\varrho = -|\mathbf{x}_h - \tilde{\mathbf{x}}_h|$ otherwise for $j = 0$ or 1 . We can replace the high order radial (normal) derivatives using equation based differentiation. That is, we can obtain expressions for the high order normal derivatives contained in (5.5) by differentiating the acoustic wave equation in spherical coordinates. Following this process we can rewrite (5.5) as an expression containing the trace, as well as its various tangential and time derivatives, on the upper time level. Next, we discretize the time derivatives on the upper time level using one sided backward time differences. Assuming that $\tau \approx \varrho$, we choose the order of this time discretization so that the resulting scheme maintains

the same order accuracy as (5.5). This process is detailed explicitly in Sections 3.2.4 and 4.2.2 using a fifth order accurate extension operator ($I_{Ex_j} = 5$ for $j = 0$ or 1) in both cases. Accordingly, the extension operator can be written as

$$\mathbf{E}x_j \boldsymbol{\zeta}_{\Gamma_j}^{n+1} = \mathbf{E}x_{H_j} \boldsymbol{\zeta}_{\Gamma_j}^{n+1} + \mathbf{E}x_{I_j}^{n+1}, \quad (5.6)$$

for $j = 0$ or 1 . The homogeneous term on Γ_0 satisfies

$$\begin{aligned} \mathbf{E}x_{H_0} \boldsymbol{\zeta}_{\Gamma_0}^{n+1} &= \left[1 + \frac{\varrho^2}{2} \left(\frac{d_0^{n+1}}{c_\infty^2} - \frac{\Delta_{\theta,\varphi}}{r^2} \right) + \frac{\varrho^3}{6} \left(-\frac{2d_0^{n+1}}{c_\infty^2 r} + \frac{4\Delta_{\theta,\varphi}}{r^3} \right) \right. \\ &+ \left. \frac{\varrho^4}{24} \left(d_0^{n+1} \left(\frac{8 - 2\Delta_{\theta,\varphi}}{c_\infty^2 r^2} \right) + \frac{\tilde{d}_0^{n+1}}{c_\infty^4} + \frac{\Delta_{\theta,\varphi}^2 - 18\Delta_{\theta,\varphi}}{r^4} \right) \right] u^{n+1} \\ &+ \left[\varrho - \frac{\varrho^2}{r} + \frac{\varrho^3}{6} \left(\frac{d_1^{n+1}}{c_\infty^4} + \frac{6 - \Delta_{\theta,\varphi}}{r^2} \right) + \frac{\varrho^4}{24} \left(-\frac{4d_1^{n+1}}{c_\infty^2 r} + \frac{8\Delta_{\theta,\varphi} - 24}{r^3} \right) \right] \frac{\partial u^{n+1}}{\partial r}, \quad (5.7) \end{aligned}$$

where $c(\mathbf{x}) = c_\infty$ for all $\mathbf{x} \in \Gamma_0$, the homogeneous term on Γ_1 satisfies

$$\begin{aligned} \mathbf{E}x_{H_1} \boldsymbol{\zeta}_{\Gamma_1}^{n+1} &= \left[1 + \frac{\varrho^2}{2} \left(\frac{d_0^{n+1}}{c^2} - \frac{\Delta_{\theta,\varphi}}{r^2} \right) + \frac{\varrho^3}{6} \left(-d_0^{n+1} \left(\frac{2}{c^2 r} + \frac{2}{c^3} \frac{\partial c}{\partial r} \right) + \frac{4\Delta_{\theta,\varphi}}{r^3} \right) \right. \\ &+ \left. \frac{\varrho^4}{24} \left(d_0^{n+1} \left(\frac{8 - \Delta_{\theta,\varphi}}{c^2 r^2} + \frac{4}{c^3 r} \frac{\partial c}{\partial r} + \frac{6}{c^4} \left(\frac{\partial c}{\partial r} \right)^2 - \frac{2}{c^3} \frac{\partial^2 c}{\partial r^2} \right) \right. \right. \\ &+ \left. \left. \frac{\tilde{d}_0^{n+1}}{c^4} + \frac{\Delta_{\theta,\varphi}^2 - 18\Delta_{\theta,\varphi}}{r^4} \right) \right] u^{n+1} \\ &+ \left[\varrho - \frac{\varrho^2}{r} + \frac{\varrho^3}{6} \left(\frac{d_1^{n+1}}{c^4} + \frac{6 - \Delta_{\theta,\varphi}}{r^2} \right) \right. \\ &+ \left. \frac{\varrho^4}{24} \left(-d_1^{n+1} \left(\frac{4}{c^2 r} + \frac{4}{c^3} \frac{\partial c}{\partial r} \right) + \frac{8\Delta_{\theta,\varphi} - 24}{r^3} \right) \right] \frac{\partial u^{n+1}}{\partial r} \\ &- \frac{\varrho^4 d_0^{n+1}}{24} \Delta_{\theta,\varphi} \left(\frac{u^{n+1}}{c^2 r^2} \right), \quad (5.8) \end{aligned}$$

the inhomogenous term on Γ_0 satisfies

$$\begin{aligned} \mathbf{E}x_{I_0}^{n+1} &= \left[\frac{\varrho^2}{2c_\infty^2} - \frac{\varrho^3}{3c_\infty^2 r} + \frac{\varrho^4(8 - 2\Delta_{\theta,\varphi})}{24c_\infty^2 r^2} \right] \sum_{j=0}^{J_0} d_0^{n-j} u^{n-j} + \left[\frac{\varrho^3}{6c_\infty^2} - \frac{\varrho^4}{6c_\infty^2 r} \right] \sum_{j=0}^{J_1} d_1^{n-j} \frac{\partial u^{n-j}}{\partial r} \\ &+ \frac{\varrho^4}{24c_\infty^2} \left(\sum_{j=0}^{J_0} \tilde{d}_0^{n-j} u^{n-j} \right), \end{aligned} \quad (5.9)$$

and the inhomogeneous term on Γ_1 is

$$\begin{aligned} \mathbf{E}x_{I_1}^{n+1} &= \left[\frac{\varrho^2}{2c^2} - \frac{\varrho^3}{3} \left(\frac{1}{c^2 r} + \frac{1}{c^3} \frac{\partial c}{\partial r} \right) \right. \\ &+ \left. \frac{\varrho^4}{24} \left(\frac{8 - \Delta_{\theta,\varphi}}{c^2 r^2} + \frac{4}{c^3 r} \frac{\partial c}{\partial r} + \frac{6}{c^4} \left(\frac{\partial c}{\partial r} \right)^2 - \frac{2}{c^3} \frac{\partial^2 c}{\partial r^2} \right) \right] \sum_{j=0}^{J_0} d_0^{n-j} u^{n-j} \\ &+ \left[\frac{\varrho^3}{6c^2} - \frac{\varrho^4}{24} \left(\frac{4}{c^2 r} + \frac{4}{c^3} \frac{\partial c}{\partial r} \right) \right] \sum_{j=0}^{J_1} d_1^{n-j} \frac{\partial u^{n-j}}{\partial r} - \frac{\varrho^4}{24} \Delta_{\theta,\varphi} \left(\sum_{j=0}^{J_0} \frac{d_0^{n-j} u^{n-j}}{c^2 r^2} \right) \\ &+ \frac{\varrho^4}{24c^2} \left(\sum_{j=0}^{J_0} \tilde{d}_0^{n-j} u^{n-j} \right). \end{aligned} \quad (5.10)$$

Notice that, the inhomogeneous terms $\mathbf{E}x_{I_j}^{n+1}$ for $j = 0$ or 1 can be assembled from known quantities: the trace $\boldsymbol{\xi}_\Gamma = (u, \frac{\partial u}{\partial r})|_\Gamma$ from previous time levels, tangential derivatives of the trace via the Laplace-Beltrami operator, and normal derivatives of the propagation speed. Also notice that, the homogeneous terms $\mathbf{E}x_{H_j}^{n+1} \boldsymbol{\xi}_\Gamma^{n+1}$ depend on the trace on the upper time level. We will formally think of (5.6) as an affine operator where the trace is replaced with a general smooth pair of functions $\boldsymbol{\xi}_{\Gamma_j} = (\xi_0^j, \xi_1^j)$. This formulation will be convenient when representing the trace $\boldsymbol{\xi}_{\Gamma_j}^{n+1}$ in the form of a spectral expansion.

Consider the $2(1 + L_j)^2$ dimensional linear space spanned by the basis functions

$$\boldsymbol{\psi}_{lm}^{(0,j)} = (Y_l^m, 0) \quad \boldsymbol{\psi}_{lm}^{(1,j)} = (0, Y_l^m), \quad 0 \leq l \leq L_j, \text{ and } |m| \leq l. \quad (5.11)$$

Then, the trace on Γ_j has the spectral representation

$$\boldsymbol{\xi}_{\Gamma_j}^{n+1} \approx \sum_{l=0}^{L_j} \sum_{m=-l}^l \left(c_{lm}^{(0,j,n+1)} \boldsymbol{\psi}_{lm}^{(0,j)} + c_{lm}^{(1,j,n+1)} \boldsymbol{\psi}_{lm}^{(1,j)} \right), \quad (5.12)$$

where $c_{lm}^{(0,j,n+1)}$ and $c_{lm}^{(1,j,n+1)}$ are the Fourier coefficients of the Dirichlet and Neumann data, respectively, on Γ_j on the upper time level corresponding to the spherical harmonics $Y_l^m(\theta, \varphi)$ (see formula (3.21)). We will substitute (5.12) into (5.6) to obtain a spectral representation of the extension operator along Γ_j . If we substitute the basis functions (5.11) into (5.7) and (5.8) then

$$\begin{aligned} \mathbf{E}x_{H_0}\boldsymbol{\psi}_{lm}^{(0,0)} &= \left[1 + \frac{\varrho^2}{2} \left(\frac{d_0^{n+1}}{c_\infty^2} + \frac{l(l+1)}{r^2} \right) - \frac{\varrho^3}{6} \left(\frac{2d_0^{n+1}}{c_\infty^2 r} + \frac{4l(l+1)}{r^3} \right) \right. \\ &\quad \left. + \frac{\varrho^4}{24} \left(d_0^{n+1} \left(\frac{8+2l(l+1)}{c_\infty^2 r^2} \right) + \frac{\tilde{d}_0^{n+1}}{c_\infty^4} + \frac{l^2(l+1)^2 + 18l(l+1)}{r^4} \right) \right] \boldsymbol{\psi}_{lm}^{(0,0)}, \end{aligned} \quad (5.13)$$

$$\begin{aligned} \mathbf{E}x_{H_0}\boldsymbol{\psi}_{lm}^{(1,0)} &= \left[\varrho - \frac{\varrho^2}{r} + \frac{\varrho^3}{6} \left(\frac{d_1^{n+1}}{c_\infty^4} + \frac{6+l(l+1)}{r^2} \right) \right. \\ &\quad \left. - \frac{\varrho^4}{24} \left(\frac{4d_1^{n+1}}{c_\infty^2 r} + \frac{8l(l+1)+24}{r^3} \right) \right] \boldsymbol{\psi}_{lm}^{(1,0)}, \end{aligned} \quad (5.14)$$

$$\begin{aligned} \mathbf{E}x_{H_1}\boldsymbol{\psi}_{lm}^{(0,1)} &= \left[1 + \frac{\varrho^2}{2} \left(\frac{d_0^{n+1}}{c^2} + \frac{l(l+1)}{r^2} \right) - \frac{\varrho^3}{6} \left(d_0^{n+1} \left(\frac{2}{c^2 r} + \frac{2}{c^3} \frac{\partial c}{\partial r} \right) + \frac{4l(l+1)}{r^3} \right) \right. \\ &\quad \left. + \frac{\varrho^4}{24} \left(d_0^{n+1} \left(\frac{8+l(l+1)}{c^2 r^2} + \frac{4}{c^3 r} \frac{\partial c}{\partial r} + \frac{6}{c^4} \left(\frac{\partial c}{\partial r} \right)^2 - \frac{2}{c^3} \frac{\partial^2 c}{\partial r^2} \right) + \frac{\tilde{d}_0^{n+1}}{c^4} \right. \right. \\ &\quad \left. \left. + \frac{l^2(l+1)^2 + 18l(l+1)}{r^4} \right) \right] \boldsymbol{\psi}_{lm}^{(0,1)} + \sum_{l'=0}^{L_0} \sum_{m'=-l'}^{l'} l'(l'+1) \left\langle \frac{1}{c^2} Y_l^m, Y_{l'}^{m'} \right\rangle \boldsymbol{\psi}_{l'm'}^{(0,1)}, \end{aligned} \quad (5.15)$$

$$\begin{aligned} \mathbf{E}x_{H_1}\boldsymbol{\psi}_{lm}^{(1,1)} &= \left[\varrho - \frac{\varrho^2}{r} + \frac{\varrho^3}{6} \left(\frac{d_1^{n+1}}{c^4} + \frac{6+l(l+1)}{r^2} \right) \right. \\ &\quad \left. - \frac{\varrho^4}{24} \left(d_1^{n+1} \left(\frac{4}{c^2 r} + \frac{4}{c^3} \frac{\partial c}{\partial r} \right) + \frac{8l(l+1)+24}{r^3} \right) \right] \boldsymbol{\psi}_{lm}^{(1,1)}, \end{aligned} \quad (5.16)$$

where we have used the formula

$$\left(\Delta_{\theta, \varphi} \left(\frac{1}{c^2} Y_l^m \right), 0 \right) = \sum_{l'=0}^{\infty} \sum_{m'=-l'}^{l'} \left\langle \frac{1}{c^2} Y_l^m, Y_{l'}^{m'} \right\rangle \boldsymbol{\psi}_{lm}^{(0,1)}.$$

Using the linearity of $\mathbf{E}x_{H_j}\boldsymbol{\zeta}_{\Gamma_j}^{n+1}$, the extension operator (5.6) along Γ_j can be written as

$$\mathbf{E}x_{\Gamma_j}\boldsymbol{\zeta}_{\Gamma_j}^{n+1} = \sum_{l=0}^{L_j} \sum_{m=-l}^l \left(c_{lm}^{(0,j,n+1)} \mathbf{E}x_{H_j}\boldsymbol{\psi}_{lm}^{(0,j)} + c_{lm}^{(1,j,n+1)} \mathbf{E}x_{H_j}\boldsymbol{\psi}_{lm}^{(1,j)} \right) + \mathbf{E}x_{I_j}^{n+1}. \quad (5.17)$$

Now that we have defined the extension operator along each individual Γ_j for $j = 0$ or $j = 1$, we can construct the extension operator from the full continuous boundary $\Gamma = \Gamma_0 \cup \Gamma_1$ to the full discrete boundary $\gamma = \gamma_0 \cup \gamma_1$:

$$\mathbf{E}x_{\Gamma}\boldsymbol{\zeta}_{\Gamma}^{n+1} = \left(\mathbf{E}x_{\Gamma_0}\boldsymbol{\zeta}_{\Gamma_0}^{n+1}, \mathbf{E}x_{\Gamma_1}\boldsymbol{\zeta}_{\Gamma_1}^{n+1} \right). \quad (5.18)$$

If we substitute (5.17) into (5.18), then the extension operator on Γ satisfies

$$\mathbf{E}x_{\Gamma}\boldsymbol{\zeta}_{\Gamma}^{n+1} = \sum_{j=0}^1 \left(\sum_{l=0}^{L_j} \sum_{m=-l}^l \left(c_{lm}^{(0,j,n+1)} \widetilde{\mathbf{E}x}_{H_j}\boldsymbol{\psi}_{lm}^{(0,j)} + c_{lm}^{(1,j,n+1)} \widetilde{\mathbf{E}x}_{H_j}\boldsymbol{\psi}_{lm}^{(1,j)} \right) + \widetilde{\mathbf{E}x}_{I_j}^{n+1} \right), \quad (5.19)$$

where $i = 0, 1, j = 0, 1$. The terms $\mathbf{E}x_{H_j}\boldsymbol{\psi}_{l,m}^{(i,j)}$ are defined in (5.13), (5.14), (5.15), and (5.16),

$$\widetilde{\mathbf{E}x}_{H_j}\boldsymbol{\psi}_{lm}^{(i,j)} = \begin{cases} \mathbf{E}x_{H_j}\boldsymbol{\psi}_{lm}^{(i,j)}, & \text{on } \gamma_j \\ 0, & \text{on } \gamma \setminus \gamma_j \end{cases}, \quad (5.20)$$

and

$$\widetilde{\mathbf{E}x}_{I_j}^{n+1} = \begin{cases} \mathbf{E}x_{I_j}^{n+1}, & \text{on } \gamma_j \\ 0, & \text{on } \gamma \setminus \gamma_j \end{cases}. \quad (5.21)$$

The inhomogeneous terms $\mathbf{E}x_{I_0}^{n+1}$ and $\mathbf{E}x_{I_1}^{n+1}$ are defined in (5.9) and (5.10) respectively. The spectral representation of $\mathbf{E}x_{I_0}^{n+1}$ and $\mathbf{E}x_{I_1}^{n+1}$ is similar to (4.25) or (3.27).

5.2.2 Inhomogeneous Boundary Equation with Projection

Recall from Theorem 3.2.1 that, the trace of the solution on the discrete boundary satisfies the inhomogenous BEP (3.7). If we substitute the extension $u_{\gamma}^{n+1} = \mathbf{E}x_{\Gamma}\boldsymbol{\zeta}_{\Gamma}^{n+1}$

given by (5.19) into (3.7), then we obtain the linear system

$$\begin{aligned} & \sum_{j=0}^1 \sum_{l=0}^{L_j} \sum_{m=-l}^l \left(c_{lm}^{(0,j,n+1)} (\mathbf{P}_\gamma - \mathbf{I}_\gamma) \widetilde{\mathbf{E}}\mathbf{x}_{H_j} \boldsymbol{\psi}_{lm}^{(0,j)} + c_{lm}^{(1,j,n+1)} (\mathbf{P}_\gamma - \mathbf{I}_\gamma) \widetilde{\mathbf{E}}\mathbf{x}_{H_j} \boldsymbol{\psi}_{lm}^{(1,j)} \right) \\ & = -\mathbf{Tr}_\gamma \mathbf{G}_h \tilde{f}_R^{n+1} - \sum_{j=0}^1 (\mathbf{P}_\gamma - \mathbf{I}_\gamma) \widetilde{\mathbf{E}}\mathbf{x}_{I_j}^{n+1}, \end{aligned} \quad (5.22)$$

which contains four sets of Fourier coefficients on the upper time level. Define the matrices

$$\mathbf{Q}_i^{(j)} = \left[(\mathbf{P}_\gamma - \mathbf{I}_\gamma) \widetilde{\mathbf{E}}\mathbf{x}_{H_j} \boldsymbol{\psi}_{0,0}^{(i,j)} \quad \cdots \quad (\mathbf{P}_\gamma - \mathbf{I}_\gamma) \widetilde{\mathbf{E}}\mathbf{x}_{H_j} \boldsymbol{\psi}_{L_j,L_j}^{(i,j)} \right] \in \mathbb{C}^{|\gamma| \times \sum_{j=0}^1 (1+L_j)^2}, \quad (5.23a)$$

$$\mathbf{q}_I^{n+1} = \sum_{j=0}^1 (\mathbf{P}_\gamma - \mathbf{I}_\gamma) \widetilde{\mathbf{E}}\mathbf{x}_{I_j}^{n+1} \in \mathbb{C}^{|\gamma|}, \quad (5.23b)$$

for $i = 0, 1$ and $j = 0, 1$, where $\widetilde{\mathbf{E}}\mathbf{x}_{H_j} \boldsymbol{\psi}_{l,m}^{(i,j)}$ are defined in (5.20), the difference projection \mathbf{P}_γ is given by Definition 3.2.4, and the RHS contributions $\widetilde{\mathbf{E}}\mathbf{x}_{I_j}^{n+1}$ are defined in (5.21). We can assemble the matrix $\mathbf{Q}_i^{(j)}$ by applying the operator $\mathbf{P}_\gamma - \mathbf{I}_\gamma$ to each of the $(1 + L_j)^2$ columns given by $\widetilde{\mathbf{E}}\mathbf{x}_{H_j} \boldsymbol{\psi}_{l,m}^{(i,j)}$ for $l = 0, \dots, L_j$, $m = -l, \dots, l$. To reduce the number of applications of \mathbf{P}_γ (which requires an application of the the solution operator \mathbf{G}_h) to nearly one half, we can use the relationship $Y_l^{-m} = (-1)^m \overline{Y_l^m}$ which implies that $\mathbf{P}_{\mathbb{N}^+} \boldsymbol{\psi}_{l,-m}^{(i,j)} = (-1)^m \overline{\mathbf{P}_{\mathbb{N}^+} \boldsymbol{\psi}_{l,m}^{(i,j)}}$, where the overline indicates complex conjugation. Using (5.23a) and (5.23b), we can rewrite the linear system (5.22) as follows

$$\sum_{j=0}^1 \mathbf{Q}_0^{(j)} \mathbf{c}_{0,j}^{n+1} + \mathbf{Q}_1^{(j)} \mathbf{c}_{1,j}^{n+1} = -\mathbf{Tr}_\gamma \mathbf{G}_h \tilde{f}_R^{n+1} - \mathbf{q}_I^{n+1}, \quad (5.24)$$

where the Fourier coefficients (see formula (3.21)) on the n^{th} time level are

$$\mathbf{c}_{i,j}^n = \left[c_{0,0}^{(i,j,n)} \quad c_{1,-1}^{(i,j,n)} \quad c_{1,0}^{(i,j,n)} \quad c_{1,1}^{(i,j,n)} \quad \cdots \quad c_{L_j,L_j}^{(i,j,n)} \right]. \quad (5.25)$$

The last remaining step is to substitute the boundary condition of the truncated exterior boundary value problem (5.2) on Γ . We will use the spectral form of the ABC specified on Γ_0 and the spectral form of the boundary condition on the scattering

surface $l_{\Gamma_1}(u) = \varphi_{\Gamma_1}$ (see formula (5.3)).

Let's assume that the p^{th} order non-reflecting boundary condition (NRBC(p)) (1.10a) - (1.10b) is imposed on Γ_0 . If we discretize NRBC(p) in time with the q^{th} order linear multistep method (backwards differentiation formula), replace the variables with their spectral representation, and exploit the orthogonality of the spherical harmonics with respect to the weighted inner product (B.1) then we arrive at the system of equations

$$\begin{aligned} -\sum_{i=1}^q \frac{a_i c_{0,0}^{(0,0,n+1-i)}}{1 + \tau c_{\infty} b_0 / R_0} &= c_{0,0}^{(0,0,n+1)} + \frac{\tau c_{\infty} b_0}{1 + \tau c_{\infty} b_0 / R_0} c_{0,0}^{(1,0,n+1)}, \quad (l, m) = (0, 0), \quad (5.26) \\ -\tilde{\mathbf{B}}_l^{-1} \left(\sum_{i=1}^q a_i \tilde{\mathbf{v}}_{lm}^{n+1-i} \right) &= \tilde{\mathbf{v}}_{lm}^{n+1} + \tau c_{\infty} b_0 c_{lm}^{(1,0,n+1)} \tilde{\mathbf{B}}_l^{-1} \tilde{\mathbf{e}}_1, \quad l = 1, \dots, L_0, |m| \leq l, \end{aligned} \quad (5.27)$$

where the tridiagonal matrix $\tilde{\mathbf{B}}_l$ is defined in (4.35), the auxiliary variables are as follows

$$\mathbf{v}_{lm}^n = [v_{lm}^{(1,n)}, v_{lm}^{(2,n)}, \dots, v_{lm}^{(p,n)}]^T \in \mathbb{C}^p,$$

the complex vector of Fourier coefficients is given by

$$\tilde{\mathbf{v}}_{lm}^n = [c_{l,m}^{(0,0,n)}, v_{lm}^{(1,n)}, v_{lm}^{(2,n)}, \dots, v_{lm}^{(p,n)}]^T \in \mathbb{C}^{p+1},$$

and $\tilde{\mathbf{e}}_1 \in \mathbb{R}^{p+1}$ is the unit canonical vector in the first position. For more details on the derivation, see our discussion of NRBC(p) in Section 4.2.2. Combining (5.26) and the first component of (5.27) for $(l, m) \neq (0, 0)$, we obtain a "Robin-like" boundary condition for the Fourier coefficients on Γ_0 :

$$\mathbf{c}_{0,0}^{n+1} + \mathbf{M}_{1,0} \mathbf{c}_{1,0}^{n+1} = \mathbf{c}_{\text{NRBC}(p),0}^{n+1}, \quad (5.28)$$

where $\mathbf{M}_{1,0}$ is a diagonal matrix and $\mathbf{c}_{\text{NRBC}(p),0}^{n+1}$ contains known coefficients from the previous time levels.

Now that we have derived the spectral form of the boundary condition on Γ_0 , let's do the same for Γ_1 . The spectral representation of the boundary condition $l_{\Gamma_1}(u) = \varphi_{\Gamma_1}$,

where l_{Γ_1} is given by (5.3), can be written as

$$a\mathbf{c}_{0,1}^{n+1} + b\mathbf{c}_{1,1}^{n+1} = \mathbf{c}_{\Gamma_1}^{n+1} = \left[\langle \varphi_{\Gamma_1}, Y_0^0 \rangle, \langle \varphi_{\Gamma_1}, Y_1^{-1} \rangle, \dots, \langle \varphi_{\Gamma_1}, Y_{L_1}^{L_1} \rangle \right]^T. \quad (5.29)$$

If a Dirichlet boundary condition is specified on Γ_1 ($(a, b) = (1, 0)$), then $\mathbf{c}_{0,1}^{n+1} = \mathbf{c}_{\Gamma_1}^{n+1}$. If a Neumann boundary condition is specified on Γ_1 ($(a, b) = (0, 1)$), then $\mathbf{c}_{1,1}^{n+1} = \mathbf{c}_{\Gamma_1}^{n+1}$. Otherwise, (5.29) can be used to eliminate one of the subsets of Fourier coefficients, $\mathbf{c}_{0,1}^{n+1}$ or $\mathbf{c}_{1,1}^{n+1}$. Substituting (5.28) and (5.29) into (5.24), we arrive at

$$\mathbf{Q}\mathbf{c} = \tilde{\mathbf{Q}}\tilde{\mathbf{c}} - \text{Tr}_\gamma \mathbf{G}_h \tilde{\mathbf{f}}_R^{n+1} - \mathbf{q}_I^{n+1}, \quad (5.30)$$

where $\mathbf{c} \in \mathbb{C}^{\sum_{j=0}^1 (1+L_j)^2}$ is a combined vector of unknown Fourier coefficients, $\tilde{\mathbf{c}} \in \mathbb{C}^{\sum_{j=0}^1 (1+L_j)^2}$ is a vector of known Fourier coefficients, and the matrices $\mathbf{Q}, \tilde{\mathbf{Q}} \in \mathbb{C}^{|\gamma| \times \sum_{j=0}^1 (1+L_j)^2}$ are the matrices which result from substituting the spectral representation into (5.24). Since the solutions to (5.2) are smooth, the spectral expansions converge rapidly. Therefore, $|\gamma| \gg \sum_{j=0}^1 (1+L_j)^2$. Hence, the overdetermined system (5.30) can be solved in the least squares sense using QR factorization. Note that, the matrices \mathbf{Q} and $\tilde{\mathbf{Q}}$ do not depend on time. Therefore, only one complex valued QR decomposition of \mathbf{Q} needs to be taken. Once the coefficients \mathbf{c} are obtained from solving (5.30) with QR factorization, we can use \mathbf{c} along with (5.28) and (5.27) to obtain the remaining set of Fourier coefficients on Γ_0 and the Fourier coefficients of the auxiliary variable on the spherical outer boundary. Similarly, if a Robin boundary condition is specified on Γ_1 , then \mathbf{c} along with (5.29) can be used to determine the remaining set of Fourier coefficients on Γ_1 . Once all the Fourier coefficients (5.25) on the upper time level have been determined, we can use the extension operator to compute the trace of the discrete solution on γ , i.e. $u_\gamma^{n+1} = \mathbf{Ex}_\Gamma \boldsymbol{\xi}_\Gamma^{n+1}$ (see formula (5.19)). Then, we substitute the trace of the solution on γ into the generalized Green's formula (3.8) and obtain the overall discrete solution to (5.4) on the upper time level.

5.3 Numerical Tests for the Scattering Problem

In this section, we present the results of numerical simulations that corroborate the design fourth order accuracy when solving the scattering problem (1.5) with the help

of the MDP. We will measure the error of our scheme using the infinity norm

$$\|u - u_h\|_\infty = \max_n \max_{(x_i, y_j, z_k) \in \mathbb{M}^+} |u(x_i, y_j, z_k, t^n) - u_h(x_i, y_j, z_k, t^n)|,$$

where u is a given smooth solution to the exterior boundary value problem (1.5) and u_h is the approximate solution to (1.5) on a uniform Cartesian grid with size h and time step τ . The rate of convergence is given by the quotient

$$\text{rate} = \log \left(\frac{\|u - u_{2h}\|_\infty}{\|u - u_h\|_\infty} \right) / \log(2).$$

The following test case will be used for simulations of the scattering problem (1.5).

Example 1 Consider the following initial boundary value problem for the wave equation on the spherical shell $\Omega = \{\mathbf{x} \mid 1.5 \geq \|\mathbf{x}\|_2 \geq 1.0\}$:

$$\begin{aligned} \frac{\partial^2 u}{\partial t^2} - \Delta u &= 0, & (\mathbf{x}, t) \in \Omega \times (0, T], \\ u(\mathbf{x}, 0) &= 0, & \mathbf{x} \in \Omega, \\ \frac{\partial u}{\partial t}(\mathbf{x}, 0) &= 0, & \mathbf{x} \in \Omega, \\ B_p(u) &= 0, & \|\mathbf{x}\| = 1.5, \\ u|_{\|\mathbf{x}\|=1} &= \varphi, \end{aligned} \tag{5.31}$$

The solution to (5.31) is taken as $u = u_{7,1.0}^{\text{Test}}$, see formula (A.3). The corresponding source term $F = F_{7,1.0}^{\text{Test}}$ is given by formula (A.5). It vanishes on the spherical shell Ω so that the wave equation is homogeneous. The test solution is generated by the wavelet $S(t) = 5(1 - 12t^2)e^{-6t^2}$ centered at the origin $(x_0, y_0, z_0) = (0, 0, 0)$ with the translation $t_0 = 3$. The Dirichlet data φ on the scattering surface $\|\mathbf{x}\| = 1$ are derived directly from $u = u_{7,1.0}^{\text{Test}}$. Since the test solution is radially symmetric and centered at the origin, the direction of propagation is orthogonal to the spherical artificial boundary. This is the best case scenario for the absorbing boundary condition $B_p(u) = 0$.

The error history curves for the test problem (5.31) are shown in Figure 5.1 (for the settings described in the caption). The fourth order grid convergence can be observed for the terminal time $T = \frac{15}{2}$. However, for longer simulation times the convergence may get disrupted. We attribute this to the possible imperfections of the

implementation, although the true reason still remains not known.

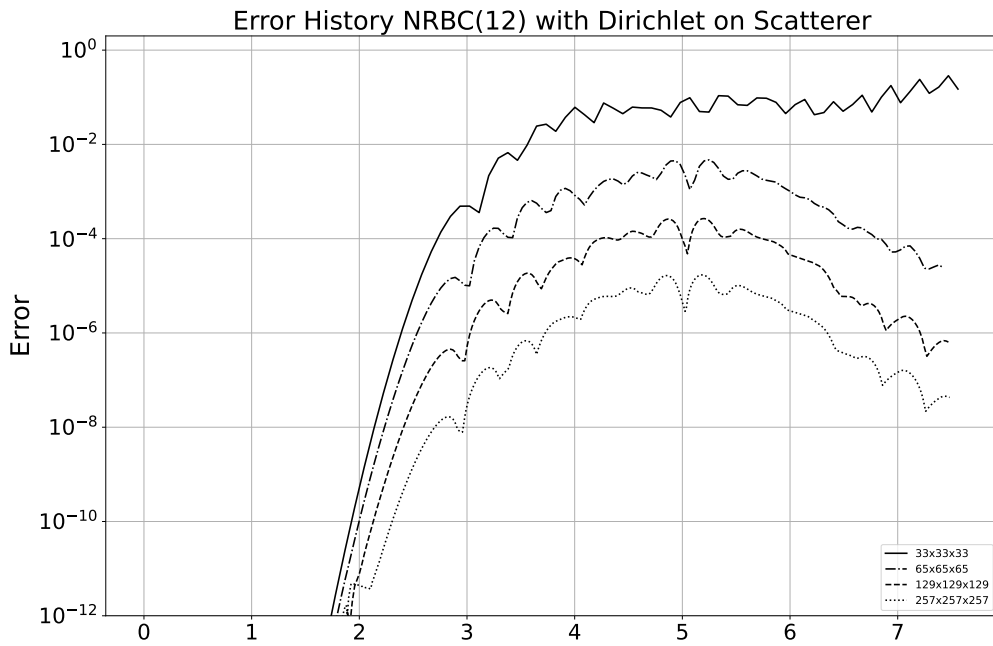


Figure 5.1: Error history for (5.31) where the computational domain is the spherical shell $\Omega = \{\mathbf{x} \mid 1.0 \leq \|\mathbf{x}\|_2 \leq 1.5\}$, the auxiliary domain $\Omega^0 = [-2.0, 2.0]^3$, the order of the spherical harmonics expansions $L_0 = L_1 = 18$, and the terminal time $T = \frac{15}{2}$. The overall error from the coarsest to the finest grid is $2.865e-01$, $4.691e-03$, $2.674e-04$, and $1.703e-05$.

Chapter 6

CONCLUSIONS

This dissertation presents several high order compact schemes for both interior and exterior boundary value problems for the three dimensional acoustic wave equation. In every scenario we discretize the acoustic wave equation in time using the θ -scheme. This produces a one parameter family of elliptic partial differential equations on the upper time level. We solve this elliptic partial differential equation using a combination of geometric multigrid and the method of difference potentials. In the case of exterior problems we terminate the unbounded domains using a high order artificial boundary condition.

In Chapter 2, we solve the acoustic wave equation on a cubic domain with homogeneous boundary conditions. This benchmark problem lays the foundation for our more complicated interior and exterior problems which all use the method of difference potentials. In Chapter 3, we consider the acoustic wave equation on a general domain Ω with a smooth boundary. Here we use the method of difference potentials with a cubic auxiliary domain which contains Ω . This lets us use the same uniformly discretized scheme derived in Chapter 2. For our numerical implementations we considered when Ω is a sphere since we know the spherical harmonics are good basis on the surface of the sphere. We demonstrate that if the speed of propagation is constant, radially symmetric, or varies in general and the given boundary condition is of Dirichlet, Neumann, or Robin type, then fourth order accuracy is achieved. In Chapter 4 we consider the acoustic wave equation when the domain is all of \mathbb{R}^3 and the speed is uniform outside outside of a sufficiently large ball. We consider two different approaches. The first approach is to terminate the unbounded domain with a spherical outer boundary using the artificial boundary condition attributed to

Hagstrom and Hariharan. We then use the method of difference potentials in the same capacity as Chapter 2. Our second to approach is to truncate the unbounded domain with a sponge layer on a cubic computational domain. Under suitable conditions both approaches produced fourth order accuracy overall.

In every problem described above, advancing the scheme amounts to solving an elliptic PDE fast using multigrid as the primary solver. If Ω is a cube with homogeneous boundary conditions we solve the elliptic PDE with multigrid directly. Otherwise we solve the elliptic PDE with the method of difference potentials which relies primarily on the same multigrid solver as the previous case with a cubic domain. As a consequence advancing the time marching scheme can be done in $\mathcal{O}(N \log N)$ floating point operations per time step. This is especially important because each problem takes place in three dimensional domains.

For future work we need to fix the long run stability issues we discovered in 5. We suspect the problem is an implementation issue due to boundary of the scattering consisting of two disjoint subsets. If we can fix this issue, that means we can solve interior BVP, exterior IVP on \mathbb{R}^3 , and exterior IBVP on the complement of some bounded domain all with the method of difference potentials despite using a uniformly discretized grid in every case.

Another direction we can take this research is to adapt our methodology to a wider class of wave equations in acoustics, electromagnetics, or seismology. For example we could consider the wave equation $\frac{\partial^2 u}{\partial t^2} - \nabla \cdot (c^2 \nabla u) = F$. We can approximate the term $\nabla \cdot (c^2 \nabla u)$ on a $3 \times 3 \times 3$ stencil using the same methodology as [16]. Another wave equation we could consider is the electromagnetic wave equation which derives from Maxwell's equation when the divergence of the magnetic field and electric field are both zero. The results of Chapters 2, 3, and 4 could immediately carry over, albeit to a system of wave equations. Finally, we could consider the elastic wave equation in inhomogeneous anisotropic media. The elastic wave equation would represent the largest deviation from our dissertation since the elastic wave equation is a system of coupled wave equations. However, we believe this would yield the largest returns since the elastic wave equation is a more realistic model in seismic wave propagation, scheme would be have a narrow bandwidth and could be solve fast, and have the capacity to handle variable coefficients.

Another direction we can take this research is to solve the interior IBVP with more general geometry. In our work we considered the sphere. We could extend the

results to other elementary shaped domains which admit a nice coordinate system and/or admits a nice orthogonal basis. To further push the geometric capabilities of our scheme, we can consider general domains parameterized with computer aided design. This approach has been successfully implemented in [80] for 3D acoustic scattering about a submarine shaped region with constant speed of propagation. If we can utilize the same methodology we could solve problems with variable coefficients. This would demonstrate that the method of difference potentials could compete with finite elements and finite volumes with regards to geometric flexibility.

The last direction we would consider is incorporating a perfectly matched layer into our scheme. Similar to our sponge layer, the perfectly matched layer modifies the acoustic wave equation inside the damping region, but coincides with the ordinary acoustic wave equation in the vacuum region. Unlike the sponge layer, the damping region contains additional auxiliary variables which must be kept track of in our scheme. Generally speaking a perfectly matched layer absorbs outgoing wave better than a sponge layer, but are harder to implement in practice. Our problem would be especially challenging since the scheme is implicit in nature. However, we believe we can use this perfectly matched layer and preserve the fast solver despite the complications. In the vacuum region we would use the same discretization described in Chapter 2. In the damping region we could discretize the modified acoustic wave equation in time using the θ -scheme and the auxiliary equations in time using a Padé based approach. This guarantees that the PML modified system produces fourth order accuracy in time using only three levels. In space we can discretize using a Chebyshev polynomial of sufficiently high order. To solve the resulting system we could use a combination of substructuring or domain decomposition with multigrid in the vacuum region. This hybrid solver can be used as a preconditioner to a Krylov subspace method. We believe this could produce a robust solver which performs similarly to our schemes shown in Chapters 2 - 4 in terms of floating point operations and convergence rate.

REFERENCES

- [1] Y. ADAM, *Highly accurate compact implicit methods and boundary conditions*, J. Comput. Phys., 24 (1977), pp. 10–22.
- [2] L. ADAMS AND J. M. ORTEGA, *A multi-color SOR method for parallel computation*, Tech. Rep. 82–9, Institute for Computer Applications in Science and Engineering (ICASE), NASA Langley research Center, Hampton, VA 23655, April 1982.
- [3] M. A. ANASTASIO, J. ZHANG, D. MODGIL, AND P. J. LA RIVIÈRE, *Application of inverse source concepts to photoacoustic tomography*, Inverse Problems, 23 (2007), pp. S21–S35.
- [4] E. ANDERSON, Z. BAI, C. BISCHOF, S. BLACKFORD, J. DEMMEL, J. DONGARRA, J. DU CROZ, A. GREENBAUM, S. HAMMARLING, A. MCKENNEY, AND D. SORENSEN, *LAPACK Users' Guide*, Society for Industrial and Applied Mathematics, Philadelphia, PA, third ed., 1999.
- [5] B. ARTMAN, I. PODLADTCHIKOV, AND B. WITTEN, *Source location using time-reverse imaging*, Geophysical Prospecting, 58 (2010), pp. 861–873.
- [6] F. ASSOUS AND M. LIN, *Solving an inverse acousto-elastic scattering problems by combining full-waveform re-datuming and time reversal*, J. Comput. Phys., 445 (2021), pp. Paper No. 110603, 16.
- [7] K. ATKINSON AND W. HAN, *Spherical harmonics and approximations on the unit sphere: an introduction*, vol. 2044 of Lecture Notes in Mathematics, Springer, Heidelberg, 2012.
- [8] I. M. BABUŠKA AND S. A. SAUTER, *Is the pollution effect of the FEM avoidable for the Helmholtz equation considering high wave numbers?*, SIAM J. Numer. Anal., 34 (1997), pp. 2392–2423.
- [9] A. BAYLISS, C. I. GOLDSTEIN, AND E. TURKEL, *An iterative method for the Helmholtz equation*, J. Comput. Phys., 49 (1983), pp. 443–457.
- [10] A. BAYLISS AND E. TURKEL, *Radiation boundary conditions for wave-like equations*, Comm. Pure Appl. Math., 33 (1980), pp. 707–725.
- [11] H. BEN-HADJ-ALI, S. OPERTO, AND J. VIRIEUX, *Velocity model building by 3D frequency-domain, full-waveform inversion of wide-aperture seismic data*, GEOPHYSICS, 73 (2008), pp. VE101–VE117.
- [12] A. BRANDT, *Rigorous quantitative analysis of multigrid. I. Constant coefficients two-level cycle with L_2 -norm*, SIAM J. Numer. Anal., 31 (1994), pp. 1695–1730.

- [13] S. C. BRENNER AND L. R. SCOTT, *The Mathematical Theory of Finite Element Methods*, vol. 15 of Texts in Applied Mathematics, Springer-Verlag, New York, second ed., 2002.
- [14] W. L. BRIGGS, V. E. HENSON, AND S. F. MCCORMICK, *A multigrid tutorial*, Society for Industrial and Applied Mathematics (SIAM), Philadelphia, PA, second ed., 2000.
- [15] D. S. BRITT, S. V. TSYNKOV, AND E. TURKEL, *A high-order numerical method for the Helmholtz equation with nonstandard boundary conditions*, SIAM J. Sci. Comput., 35 (2013), pp. A2255–A2292.
- [16] S. BRITT, S. TSYNKOV, AND E. TURKEL, *Numerical simulation of time-harmonic waves in inhomogeneous media using compact high order schemes*, Commun. Comput. Phys., 9 (2011), pp. 520–541.
- [17] S. BRITT, S. TSYNKOV, AND E. TURKEL, *Numerical solution of the wave equation with variable wave speed on nonconforming domains by high-order difference potentials*, J. Comput. Phys., 354 (2018), pp. 26–42.
- [18] S. BRITT, E. TURKEL, AND S. TSYNKOV, *A high order compact time/space finite difference scheme for the wave equation with variable speed of sound*, J. Sci. Comput., 76 (2018), pp. 777–811.
- [19] P. BURGHOLZER, G. J. MATT, M. HALTMEIER, AND G. PALTAUF, *Exact and approximative imaging methods for photoacoustic tomography using an arbitrary detection surface*, Phys. Rev. E, 75 (2007), p. 046706.
- [20] A.-P. CALDERÓN, *Boundary value problems for elliptic equations*, in *Outlines Joint Sympos. Partial Differential Equations (Novosibirsk, 1963)*, Acad. Sci. USSR Siberian Branch, Moscow, 1963, pp. 303–304.
- [21] A. C. CANGELLARIS AND D. B. WRIGHT, *Analysis of the numerical error caused by the stair-stepped approximation of a conducting boundary in FDTD simulations of electromagnetic phenomena*, IEEE Trans. Antennas and Propagation, 39 (1991), pp. 1518–1525.
- [22] C. CERJAN, D. KOSLOFF, R. KOSLOFF, AND M. RESHEF, *A nonreflecting boundary condition for discrete acoustic and elastic wave equations*, GEOPHYSICS, 50 (1985), pp. 705–708.
- [23] J. CHABASSIER AND S. IMPERIALE, *Introduction and study of fourth order theta schemes for linear wave equations*, J. Comput. Appl. Math., 245 (2013), pp. 194–212.
- [24] P. CHEN AND E.-J. LEE, *Full-3D seismic waveform inversion: Theory, software and practice*, Springer, 2015.

- [25] M. CHENEY, D. ISAACSON, AND J. C. NEWELL, *Electrical impedance tomography*, SIAM Rev., 41 (1999), pp. 85–101.
- [26] H. CHENG, L. GREENGARD, AND V. ROKHLIN, *A fast adaptive multipole algorithm in three dimensions*, J. Comput. Phys., 155 (1999), pp. 468–498.
- [27] P. C. CHU AND C. FAN, *A three-point combined compact difference scheme*, J. Comput. Phys., 140 (1998), pp. 370–399.
- [28] P. G. CIARLET, *The Finite Element Method for Elliptic Problems*, vol. 40 of Classics in Applied Mathematics, Society for Industrial and Applied Mathematics (SIAM), Philadelphia, PA, 2002. Reprint of the 1978 original [North-Holland, Amsterdam; MR0520174 (58 #25001)].
- [29] O. DORN AND Y. WU, *Shape reconstruction in seismic full waveform inversion using a level set approach and time reversal*, J. Comput. Phys., 427 (2021), pp. Paper No. 110059, 26.
- [30] B. DUCOMET, A. ZLOTNIK, AND A. ROMANOVA, *On a splitting higher-order scheme with discrete transparent boundary conditions for the Schrödinger equation in a semi-infinite parallelepiped*, Appl. Math. Comput., 255 (2015), pp. 196–206.
- [31] I. EPANOMERITAKIS, V. AKÇELIK, O. GHATTAS, AND J. BIELAK, *A newton-CG method for large-scale three-dimensional elastic full-waveform seismic inversion*, Inverse Problems, 24 (2008), p. 034015.
- [32] O. G. ERNST AND M. J. GANDER, *Why it is difficult to solve Helmholtz problems with classical iterative methods*, in Numerical analysis of multiscale problems, vol. 83 of Lect. Notes Comput. Sci. Eng., Springer, Heidelberg, 2012, pp. 325–363.
- [33] E. ERTURK, *Comparison of wide and compact fourth-order formulations of the Navier-Stokes equations*, Internat. J. Numer. Methods Fluids, 60 (2009), pp. 992–1010.
- [34] V. ESFAHANIAN, K. HEJRANFAR, AND H. MAHMOODI DARIAN, *Implementation of high-order compact finite-difference method to parabolized Navier-Stokes schemes*, Internat. J. Numer. Methods Fluids, 58 (2008), pp. 659–685.
- [35] R. ESKAR, P. HUANG, AND X. FENG, *A new high-order compact ADI finite difference scheme for solving 3D nonlinear Schrödinger equation*, Adv. Difference Equ., (2018), pp. Paper No. 286, 15.
- [36] C. FARHAT, I. HARARI, AND L. FRANCA, *The discontinuous enrichment method*, Computer Meth. in Appl. Mech. & Eng., 190 (2001), pp. 6455–6479.

- [37] C. FARHAT, R. TEZAUER, AND J. TOIVANEN, *A domain decomposition method for discontinuous Galerkin discretizations of Helmholtz problems with plane waves and Lagrange multipliers*, *International Journal for Numerical Methods in Engineering*, 78 (2009), pp. 1513–1531.
- [38] A. FICHTNER, B. L. N. KENNETT, H. IGEL, AND H.-P. BUNGE, *Full seismic waveform tomography for upper-mantle structure in the Australasian region using adjoint methods*, *Geophysical Journal International*, 179 (2009), pp. 1703–1725.
- [39] W. FONG AND E. DARVE, *The black-box fast multipole method*, *J. Comput. Phys.*, 228 (2009), pp. 8712–8725.
- [40] Y. FU, *Compact fourth-order finite difference schemes for Helmholtz equation with high wave numbers*, *J. Comput. Math.*, 26 (2008), pp. 98–111.
- [41] W. GAO, H. LI, Y. LIU, AND X. WEI, *A Padé compact high-order finite volume scheme for nonlinear Schrödinger equations*, *Appl. Numer. Math.*, 85 (2014), pp. 115–127.
- [42] B. GEBAUER AND O. SCHERZER, *Impedance-acoustic tomography*, *SIAM J. Appl. Math.*, 69 (2008), pp. 565–576.
- [43] D. GIVOLI, *Exact Representations on Artificial Interfaces and Applications in Mechanics*, *Applied Mechanics Reviews*, 52 (1999), pp. 333–349.
- [44] ———, *High-order local non-reflecting boundary conditions: a review*, *Wave Motion*, 39 (2004), pp. 319–326. *New computational methods for wave propagation.*
- [45] ———, *Computational absorbing boundaries*, in *Computational Acoustics of Noise Propagation in Fluids - Finite and Boundary Element Methods*, S. Marburg and B. Nolte, eds., Springer Berlin Heidelberg, Berlin, Heidelberg, 2008, pp. 145–166.
- [46] ———, *Time reversal as a computational tool in acoustics and elastodynamics*, *J. Comput. Acoust.*, 22 (2014), pp. 1430001, 40.
- [47] L. GREENGARD AND V. ROKHLIN, *A fast algorithm for particle simulations*, *J. Comput. Phys.*, 73 (1987), pp. 325–348.
- [48] W. HA, S.-G. KANG, AND C. SHIN, *3d laplace-domain waveform inversion using a low-frequency time-domain modeling algorithm*, *GEOPHYSICS*, 80 (2015), pp. R1–R13.
- [49] T. HAGSTROM AND S. I. HARIHARAN, *A formulation of asymptotic and exact boundary conditions using local operators*, *Appl. Numer. Math.*, 27 (1998), pp. 403–416. *Absorbing boundary conditions.*
- [50] I. HARARI AND E. TURKEL, *Accurate finite difference methods for time-harmonic wave propagation*, *J. Comput. Phys.*, 119 (1995), pp. 252–270.

- [51] J. S. HESTHAVEN AND T. WARBURTON, *Nodal discontinuous Galerkin methods*, vol. 54 of Texts in Applied Mathematics, Springer, New York, 2008. Algorithms, analysis, and applications.
- [52] S. P. HIRSHMAN, K. S. PERUMALLA, V. E. LYNCH, AND R. SANCHEZ, *BCYCLIC: a parallel block tridiagonal matrix cyclic solver*, J. Comput. Phys., 229 (2010), pp. 6392–6404.
- [53] R. HOLLAND, *Pitfalls of staircase meshing*, IEEE Trans. Electromagnetic Compatibility, 35 (1993), pp. 434–439.
- [54] S. HOLMES AND W. FEATHERSTONE, *A unified approach to the Clenshaw summation and the recursive computation of very high degree and order normalised associated Legendre functions*, Journal of Geodesy, 76 (2002), pp. 279–299.
- [55] S. HOSSEINVERDI AND H. F. FASEL, *An efficient, high-order method for solving Poisson equation for immersed boundaries: combination of compact difference and multiscale multigrid methods*, J. Comput. Phys., 374 (2018), pp. 912–940.
- [56] R. HUAN AND L. L. THOMPSON, *Accurate radiation boundary conditions for the time-dependent wave equation on unbounded domains*, International Journal for Numerical Methods in Engineering, 47 (2000), pp. 1569–1603.
- [57] F. IHLENBURG, *Finite Element Analysis of Acoustic Scattering*, vol. 132 of Applied Mathematical Sciences, Springer, 1998.
- [58] A. KAHANA, F. SMITH, E. TURKEL, AND S. TSYNKOV, *A high order compact time/space finite difference scheme for the 2D and 3D wave equation with a damping layer*, J. Comput. Phys., 460 (2022), p. Paper No. 111161.
- [59] E. KASHDAN AND B. GALANTI, *A new parallelization strategy for solving time-dependent 3D Maxwell equations using a high-order accurate compact implicit scheme*, International Journal of Numerical Modelling: Electronic Networks, Devices and Fields, 19 (2006), pp. 391–408.
- [60] K. KIMOTO, K. NAKAHATA, AND T. SAITOH, *An elastodynamic computational time-reversal method for shape reconstruction of traction-free scatterers*, Wave Motion, 72 (2017), pp. 23–40.
- [61] S. KOO, P. M. KARVE, AND L. F. KALLIVOKAS, *A comparison of time-reversal and inverse-source methods for the optimal delivery of wave energy to subsurface targets*, Wave Motion, 67 (2016), pp. 121–140.
- [62] ———, *A comparison of time-reversal and inverse-source methods for the optimal delivery of wave energy to subsurface targets*, Wave Motion, 67 (2016), pp. 121–140.

- [63] S. KREMERS, A. FICHTNER, G. B. BRIETZKE, H. IGEL, C. LARMAT, L. HUANG, AND M. KÄSER, *Exploring the potentials and limitations of the time-reversal imaging of finite seismic sources*, *Solid Earth*, 2 (2011), pp. 95–105.
- [64] S. K. LELE, *Compact finite difference schemes with spectral-like resolution*, *J. Comput. Phys.*, 103 (1992), pp. 16–42.
- [65] R. J. LEVEQUE AND Z. L. LI, *The immersed interface method for elliptic equations with discontinuous coefficients and singular sources*, *SIAM J. Numer. Anal.*, 31 (1994), pp. 1019–1044.
- [66] M. LI, T. TANG, AND B. FORNBERG, *A compact fourth-order finite difference scheme for the steady incompressible Navier-Stokes equations*, *Internat. J. Numer. Methods Fluids*, 20 (1995), pp. 1137–1151.
- [67] Z. LI AND K. ITO, *The Immersed Interface Method*, vol. 33 of *Frontiers in Applied Mathematics*, Society for Industrial and Applied Mathematics (SIAM), Philadelphia, PA, 2006.
- [68] H. LIANG, M. Z. LIU, AND W. LV, *Stability of θ -schemes in the numerical solution of a partial differential equation with piecewise continuous arguments*, *Appl. Math. Lett.*, 23 (2010), pp. 198–206.
- [69] Y. MA, L. KONG, J. HONG, AND Y. CAO, *High-order compact splitting multisymplectic method for the coupled nonlinear Schrödinger equations*, *Comput. Math. Appl.*, 61 (2011), pp. 319–333.
- [70] P.-G. MARTINSSON, *Fast multiscale methods for lattice equations*, PhD thesis, Texas Institute for Computational and Applied Mathematics, The University of Texas at Austin, Austin, TX, USA, 2002.
- [71] M. MEDVINSKY, S. TSYNKOV, AND E. TURKEL, *The method of difference potentials for the Helmholtz equation using compact high order schemes*, *J. Sci. Comput.*, 53 (2012), pp. 150–193.
- [72] ———, *High order numerical simulation of the transmission and scattering of waves using the method of difference potentials*, *J. Comput. Phys.*, 243 (2013), pp. 305–322.
- [73] L. MÉTIVIER, R. BROSSIER, Q. MÉRIGOT, E. OUDET, AND J. VIRIEUX, *An optimal transport approach for seismic tomography: application to 3d full waveform inversion*, *Inverse Problems*, 32 (2016), p. 115008.
- [74] M. MIRZANEJAD AND K. T. TRAN, *3D viscoelastic full waveform inversion of seismic waves for geotechnical site investigation*, *Soil Dynamics and Earthquake Engineering*, 122 (2019), pp. 67–78.

- [75] M. J. MOHLENKAMP, *A user's guide to spherical harmonics*, 2010.
- [76] K. PAN, D. HE, AND H. HU, *An extrapolation cascadic multigrid method combined with a fourth-order compact scheme for 3D Poisson equation*, *J. Sci. Comput.*, 70 (2017), pp. 1180–1203.
- [77] J. M. C. PEREIRA, M. H. KOBAYASHI, AND J. C. F. PEREIRA, *A fourth-order-accurate finite volume compact method for the incompressible Navier-Stokes solutions*, *J. Comput. Phys.*, 167 (2001), pp. 217–243.
- [78] C. S. PESKIN, *The immersed boundary method*, *Acta Numer.*, 11 (2002), pp. 479–517.
- [79] S. PETROPAVLOVSKY AND S. TSYNKOV, *Non-deteriorating time domain numerical algorithms for Maxwell's electrodynamics*, *J. Comput. Phys.*, 336 (2017), pp. 1–35.
- [80] S. PETROPAVLOVSKY, S. TSYNKOV, AND E. TURKEL, *3d time-dependent scattering about complex shapes using high order difference potentials*, *Journal of Computational Physics*, 471 (2022), p. 111632.
- [81] S. V. PETROPAVLOVSKY AND S. V. TSYNKOV, *A non-deteriorating algorithm for computational electromagnetism based on quasi-lacunae of Maxwell's equations*, *J. Comput. Phys.*, 231 (2012), pp. 558–585.
- [82] B. POURSARTIP, A. FATHI, AND J. L. TASSOULAS, *Large-scale simulation of seismic wave motion: A review*, *Soil Dynamics and Earthquake Engineering*, 129 (2020), p. 105909.
- [83] D. RABINOVICH, D. GIVOLI, J. BIELAK, AND E. TURKEL, *Scatterer identification in a 2D geophysical medium using an augmented computational time reversal method*, *International Journal for Numerical and Analytical Methods in Geomechanics*, 45 (2021), pp. 867–892.
- [84] D. RABINOVICH, E. TURKEL, AND D. GIVOLI, *An augmented time reversal method for source and scatterer identification*, *J. Comput. Phys.*, 375 (2018), pp. 99–119.
- [85] A. A. REZNIK, *Approximation of surface potentials of elliptic operators by difference potentials*, *Soviet Math. Dokl.*, 25 (1982), pp. 543–545.
- [86] —, *Approximation of surface potentials of elliptic operators by difference potentials*, *Dokl. Akad. Nauk SSSR*, 263 (1982), pp. 1318–1321. [in Russian].
- [87] V. S. RYABEN' KII, *Boundary equations with projections*, *Russian Mathematical Surveys*, 40 (1985), pp. 147–183.
- [88] —, *Method of difference potentials and its applications*, vol. 30 of Springer Series in Computational Mathematics, Springer-Verlag, Berlin, 2002. Translated from the 2001 Russian original by Nikolai K. Kulman.

- [89] Y. SAAD, *Iterative methods for sparse linear systems*, Society for Industrial and Applied Mathematics, Philadelphia, PA, second ed., 2003.
- [90] N. SCHAEFFER, *Efficient spherical harmonic transforms aimed at pseudospectral numerical simulations*, *Geochemistry, Geophysics, Geosystems*, 14 (2013), pp. 751–758.
- [91] O. SCHERZER, ed., *Handbook of mathematical methods in imaging. Vol. 1, 2, 3*, Springer, New York, second ed., 2015.
- [92] S. K. SEAL, K. S. PERUMALLA, AND S. P. HIRSHMAN, *Revisiting parallel cyclic reduction and parallel prefix-based algorithms for block tridiagonal systems of equations*, *Journal of Parallel and Distributed Computing*, 73 (2013), pp. 273–280.
- [93] R. SEELY, *Singular integrals and boundary problems*, *Am. J. Math.*, 88 (1966), pp. 781–809.
- [94] J. S. SHANG, *High-order compact-difference schemes for time-dependent Maxwell equations*, *J. Comput. Phys.*, 153 (1999), pp. 312–333.
- [95] I. SINGER AND E. TURKEL, *High-order finite difference methods for the Helmholtz equation*, *Comput. Methods Appl. Mech. Engrg.*, 163 (1998), pp. 343–358.
- [96] F. SMITH, S. TSYNKOV, AND E. TURKEL, *Compact high order accurate schemes for the three dimensional wave equation*, *J. Sci. Comput.*, 81 (2019), pp. 1181–1209.
- [97] J. SOCHACKI, R. KUBICHEK, J. GEORGE, W. R. FLETCHER, AND S. SMITHSON, *Absorbing boundary conditions and surface waves*, *GEOPHYSICS*, 52 (1987), pp. 60–71.
- [98] G. STRANG AND G. J. FIX, *An Analysis of the Finite Element Method*, Prentice Hall, Englewood Cliffs, NJ, 1973.
- [99] R. A. SWEET, *A cyclic reduction algorithm for solving block tridiagonal systems of arbitrary dimension*, *SIAM J. Numer. Anal.*, 14 (1977), pp. 706–720.
- [100] U. TROTTEBERG, C. W. OOSTERLEE, AND A. SCHÜLLER, *Multigrid*, Academic Press, Inc., San Diego, CA, 2001. With contributions by A. Brandt, P. Oswald and K. Stüben.
- [101] S. V. TSYNKOV, *Numerical solution of problems on unbounded domains. A review*, *Appl. Numer. Math.*, 27 (1998), pp. 465–532. Absorbing boundary conditions.
- [102] E. TURKEL, D. GORDON, R. GORDON, AND S. TSYNKOV, *Compact 2D and 3D sixth order schemes for the helmholtz equation with variable wave number*, *Journal of Computational Physics*, 232 (2013), pp. 272–287.
- [103] D. VIGH, J. KAPOOR, N. MOLDOVEANU, AND H. LI, *Breakthrough acquisition and technologies for subsalt imaging*, *GEOPHYSICS*, 76 (2011), pp. WB41–WB51.

- [104] J. WANG, W. ZHONG, AND J. ZHANG, *A general meshsize fourth-order compact difference discretization scheme for 3D Poisson equation*, *Appl. Math. Comput.*, 183 (2006), pp. 804–812.
- [105] M. WARNER, A. RATCLIFFE, T. NANGOO, J. MORGAN, A. UMPLEBY, N. SHAH, V. VINJE, I. ŠTEKL, L. GUASCH, C. WIN, G. CONROY, AND A. BERTRAND, *Anisotropic 3d full-waveform inversion*, *GEOPHYSICS*, 78 (2013), pp. R59–R80.
- [106] M. XU AND L. WANG, *Time-domain reconstruction for thermoacoustic tomography in a spherical geometry*, *IEEE Transactions on Medical Imaging*, 21 (2002), pp. 814–822.
- [107] M. XU, Y. XU, AND L. WANG, *Time-domain reconstruction algorithms and numerical simulations for thermoacoustic tomography in various geometries*, *IEEE Transactions on Biomedical Engineering*, 50 (2003), pp. 1086–1099.
- [108] Y. XU, D. FENG, AND L. WANG, *Exact frequency-domain reconstruction for thermoacoustic tomography. i. planar geometry*, *IEEE Transactions on Medical Imaging*, 21 (2002), pp. 823–828.
- [109] Y. XU, M. XU, AND L. WANG, *Exact frequency-domain reconstruction for thermoacoustic tomography. ii. cylindrical geometry*, *IEEE Transactions on Medical Imaging*, 21 (2002), pp. 829–833.
- [110] A. YEFET AND P. G. PETROPOULOS, *A staggered fourth-order accurate explicit finite differences scheme for the time-domain Maxwell's equations*, *J. Comput. Phys.*, 168 (2001), pp. 286–315.
- [111] L. YING, G. BIROS, AND D. ZORIN, *A kernel-independent adaptive fast multipole algorithm in two and three dimensions*, *J. Comput. Phys.*, 196 (2004), pp. 591–626.
- [112] P. X. YU AND Z. F. TIAN, *A high-order compact scheme for the pure streamfunction (vector potential) formulation of the 3D steady incompressible Navier-Stokes equations*, *J. Comput. Phys.*, 382 (2019), pp. 65–85.
- [113] C. ZHANG AND R. J. LEVEQUE, *The immersed interface method for acoustic wave equations with discontinuous coefficients*, *Wave Motion*, 25 (1997), pp. 237–263.
- [114] J. ZHANG, L. GE, AND J. KOUATCHOU, *A two colorable fourth-order compact difference scheme and parallel iterative solution of the 3D convection diffusion equation*, *Math. Comput. Simulation*, 54 (2000), pp. 65–80.
- [115] X. ZHONG, *A new high-order immersed interface method for solving elliptic equations with imbedded interface of discontinuity*, *J. Comput. Phys.*, 225 (2007), pp. 1066–1099.

- [116] H.-W. ZHOU, H. HU, Z. ZOU, Y. WO, AND O. YOUN, *Reverse time migration: A prospect of seismic imaging methodology*, *Earth-Science Reviews*, 179 (2018), pp. 207–227.
- [117] Y. ZHOU, H. LIANG, AND J. CAI, *Efficient schemes for Maxwell's equations with PEC boundary condition*, *Optik*, 174 (2018), pp. 339–346.
- [118] A. ZLOTNIK AND O. KIRIEVA, *On compact 4th order finite-difference schemes for the wave equation*, 2021.
- [119] A. ZLOTNIK AND R. ČIEGIS, *On properties of compact 4th order finite-difference schemes for the variable coefficient wave equation*, 2021.
- [120] R. ÉDOUARD PLESSIX, *Three-dimensional frequency-domain full-waveform inversion with an iterative solver*, *GEOPHYSICS*, 74 (2009), pp. WCC149–WCC157.

APPENDICES

Appendix A

Generating Test Problems

Consider the wave equation with point source

$$\frac{\partial^2 u}{\partial t^2} - c^2 \Delta u = \delta_x(x - x_0) \delta_y(y - y_0) \delta_z(z - z_0) S(t), \quad (x, y, z, t) \in \mathbb{R}^3 \times (0, \infty), \quad (\text{A.1})$$

where the wave speed is constant, the initial conditions are zero, $\delta_{\xi}(\xi)$ is the one dimension Dirac delta function, $(x_0, y_0, z_0) \in \mathbb{R}^3$ is the center of the source, and S is a smooth real valued function supported on $(0, \infty)$ or a smooth rapidly decaying function on \mathbb{R} . The analytic solution to (A.1) is given by

$$u(x, y, z, t) = \frac{S(t - t_0 - r/c)}{4\pi r} \quad \text{with} \quad r = \sqrt{(x - x_0)^2 + (y - y_0)^2 + (z - z_0)^2}, \quad (\text{A.2})$$

which is clearly singular at $(x, y, z) = (x_0, y_0, z_0)$. We would like to generate a smooth analogue to the above by employing the same strategy as [79, Section 8.2]. We will modify the solution of (A.2) to suppress the singular behavior at (x_0, y_0, z_0) , but recover (A.2) outside of a sufficiently large neighborhood of (x_0, y_0, z_0) . Consider a general solution of the form

$$u_{m,\varepsilon}^{\text{Test}}(x, y, z, t) = \frac{\phi_m(r/\varepsilon) S(t - t_0 - r/c)}{4\pi r}, \quad (\text{A.3})$$

where the smooth step function

$$\phi_m(x) = \begin{cases} 0 & \text{if } x \leq 0 \\ x^{m+1} \sum_{k=0}^m \binom{m+k}{m} \binom{2m+1}{m-k} (-x)^k & \text{if } 0 < x < 1 \\ 1 & \text{if } x \geq 1 \end{cases}, \quad (\text{A.4})$$

which satisfies $\frac{d^l \phi_m}{dx^l}(0^+) = 0 = \frac{d^l \phi_m}{dx^l}(1^-)$ for $l = 1, \dots, m$. As a consequence the acoustic wave equation generated by (A.3) produces the test problem

$$\begin{aligned} \frac{\partial^2 u_{m,\varepsilon}^{\text{Test}}}{\partial t^2} - c^2 \Delta u_{m,\varepsilon}^{\text{Test}} &= F_{m,\varepsilon}^{\text{Test}}(x, y, z, t), \quad (x, y, z, t) \in \mathbb{R}^3 \times (0, \infty), \\ u_{m,\varepsilon}^{\text{Test}}(x, y, z, 0) &= \frac{\phi_m(r/\varepsilon) S(-t_0 - r/c)}{4\pi r}, \quad (x, y, z) \in \mathbb{R}^3, \\ \frac{\partial u_{m,\varepsilon}^{\text{Test}}}{\partial t}(x, y, z, 0) &= \frac{\phi_m(r/\varepsilon) S'(-t_0 - r/c)}{4\pi r}, \quad (x, y, z) \in \mathbb{R}^3, \end{aligned}$$

where the source term

$$F_{m,\varepsilon}^{\text{Test}}(x, y, z, t) \triangleq \frac{c \phi_m'(r/\varepsilon) S'(t - t_0 - r/c)}{2\pi \varepsilon r} - \frac{c^2 \phi_m''(r/\varepsilon) S(t - t_0 - r/c)}{4\pi \varepsilon^2 r}, \quad (\text{A.5})$$

is compactly supported in space on the ball of radius ε centered at $(x_0, y_0, z_0) \in \mathbb{R}^3$ and t_0 is chosen sufficiently large enough that the initial data is zero (up to machine precision).

We also want to generate a solution which is similar to (A.3) where the speed is allowed to vary with position. Suppose there exists a bounded connected set $Y \subset \mathbb{R}^3$ where the speed c is allowed to vary smoothly in Y , but there exists $c_\infty > 0$ such that $c(\mathbf{x}) = c_\infty$ whenever $\mathbf{x} \notin Y$. Given the point $(x_0, y_0, z_0) \in \mathbb{R}^3$, consider the general test solution

$$u_{m,\varepsilon}^{\text{Test}}(x, y, z, t) = \frac{\phi_m(r/\varepsilon) S(t - t_0 - r/c_\infty)}{4\pi r}. \quad (\text{A.6})$$

where the radial distance $r = \sqrt{(x - x_0)^2 + (y - y_0)^2 + (z - z_0)^2}$ and the smooth step function is defined in (A.4). If we substitute the test solution (A.6) into the LHS of the

wave equation (1.4) produces the source term

$$\begin{aligned}
 F_{m,\varepsilon}^{\text{Test}}(x, y, z, t) &= \frac{c^2 \phi'(r/\varepsilon) S'(t - t_0 - r/c_\infty)}{2\pi c_\infty \varepsilon r} - \frac{c^2 \phi''(r/\varepsilon) S(t - t_0 - r/c_\infty)}{4\pi \varepsilon^2 r} \\
 &\quad + \frac{\phi(r/\varepsilon) S''(t - t_0 - r/c_\infty)}{4\pi r} \left(1 - \frac{c^2}{c_\infty^2}\right). \tag{A.7}
 \end{aligned}$$

Note that the first two terms of (A.7) vanish outside the ball of radius $\varepsilon > 0$ centered at (x_0, y_0, z_0) since the smooth step function is constant in this region and the third term vanishes on the complement of Y . Assuming the function S is rapidly decaying or compactly supported $[0, \infty)$, we will choose the translation t_0 sufficiently large enough that the test solution (A.6) and source term (A.7) satisfies the exterior problem (1.4) up to machine precision and the domain Ω is sufficiently large enough to strictly contain the union of the ball of radius $\varepsilon > 0$ centered at (x_0, y_0, z_0) and Y .

Appendix B

Spherical Harmonics

We will use the spherical harmonics as the basis of the trace $\left(u|_{\Gamma}, \frac{\partial u}{\partial n}|_{\Gamma}\right)$. In Appendix B.1 we summarize the most pertinent properties when applying the spherical harmonics to the extension operator Section 3.2.4. In Appendix B.2 we show how to numerically evaluate the spherical harmonics using the associated Jacobi polynomials. In Appendix B.3 we will show how to evaluate the Fourier coefficients associated with the spherical harmonics using a quadrature rule.

B.1 Properties Spherical Harmonics

The following properties of the spherical harmonics are the most pertinent to the MDP:

- ◇ The spherical harmonics are orthonormal with respect to the weighted inner product

$$\left\langle Y_l^m, Y_{l'}^{m'} \right\rangle = \int_0^{2\pi} \int_0^\pi Y_l^m(\theta, \varphi) \overline{Y_{l'}^{m'}(\theta, \varphi)} \sin(\theta) d\theta d\varphi = \delta_{l,l'} \delta_{m,m'}. \quad (\text{B.1})$$

- ◇ The spherical harmonics are dense in $L^2(\mathbb{S}^2)$ and $C(\mathbb{S}^2)$.
- ◇ Let $S_L(f) \triangleq \sum_{l=0}^L \sum_{m=-l}^l \langle f, Y_l^m \rangle Y_l^m$. If there exists an integer k and $\mu \in (0, 1]$ such that $f \in C^{k,\mu}(\mathbb{S}^2)$ and $k + \mu > 1/2$, there exists $c > 0$ such that $\|f - S_L(f)\|_\infty \leq \frac{c}{L^{k+\mu-1/2}}$.

◇ The spherical harmonics are eigenfunctions of the Beltrami operator, i.e.

$$\Delta_{\theta,\varphi} Y_l^m(\theta, \varphi) = -l(l+1)Y_l^m(\theta, \varphi) \quad \text{on } \mathbb{S}^2.$$

For a complete description of spherical harmonics see the textbook [7].

B.2 Generating the Spherical Harmonics

The spherical harmonics written explicitly

$$Y_l^m(\theta, \varphi) = P_l^{|m|}(\cos(\theta))e^{im\varphi}, \quad 0 \leq \theta \leq \pi, \quad 0 \leq \varphi \leq 2\pi,$$

where the associated Legendre Functions satisfy

$$P_l^m(\cos(\theta)) = \sin^m(\theta)J_{l-m}^{(m,m)}(\cos(\theta)),$$

and the normalized associated Jacobi polynomials are computed recursively using the three term recurrence

$$\begin{aligned} J_{-1}^{(m,m)}(x) &= 0, \\ J_0^{(m,m)}(x) &= \sqrt{\frac{1}{2}} \prod_{j=1}^m \sqrt{1 + \frac{1}{2j}}, \\ J_l^{(m,m)}(x) &= 2xa_{ml}J_{l-1}^{(m,m)}(x) - b_{ml}J_{l-2}^{(m,m)}(x), \end{aligned}$$

and the coefficients are given by

$$\begin{aligned} a_{ml} &= \sqrt{\left(1 + \frac{m-1/2}{l}\right) \left(1 - \frac{m-1/2}{l+2m}\right)}, \\ b_{ml} &= \sqrt{\left(1 + \frac{4}{2(m+l)-3}\right) \left(1 - \frac{1}{l}\right) \left(1 - \frac{1}{l+2m}\right)}. \end{aligned}$$

According to [75, Chapter 3.2] the above recurrence formula is poorly conditioned for large values of m . However, we deliberately ignored this warning. Since we utilize a FOCS, we are assuming that our solution is at least six times continuously differentiable in space. The third property of Appendix B.1 guarantees rapid convergence. Since

our numerical experiments never exceeded $m = 30$ we avoid the poor conditioning altogether. For alternatives to evaluating the normalized Legendre functions see [54].

B.3 Fast Spherical Harmonics Transform

The following method describes how to compute the Fourier coefficients of the given function f on the sphere of radius R centered at the origin. In other words how to compute $\langle f, Y_l^m \rangle$ efficiently. By definition

$$\langle f, Y_l^m \rangle = \int_0^{2\pi} \int_0^\pi f(R \cos \varphi \sin \theta, R \sin \varphi \sin \theta, R \cos \theta) P_l^{|m|}(\cos(\theta)) \sin \theta e^{-im\varphi} d\theta d\varphi.$$

By Fubini's Theorem and change of variables

$$\langle f, Y_l^m \rangle = \int_{-1}^1 f_m(\cos^{-1}(z)) P_l^m(z) dz, \quad (\text{B.2})$$

where the quantity

$$f_m(\theta) = \int_0^{2\pi} f\left(R \cos \varphi \sin \theta, R \sin \varphi \sin \theta, R \cos \theta\right) e^{-im\varphi} d\varphi. \quad (\text{B.3})$$

We compute (B.3) using the Fast Fourier Transform with $2L + 1$ uniformly distributed points. We compute (B.2) using using a $2L + 1$ point Gauss-Legendre quadrature rule. We use the Glaser-Liu-Rokhlin method written by John Burkardt in Fortran 90 distributed under the GNU LGPL license to compute the nodes and weights of the Gauss-Legendre quadrature. If the reader wishes to further optimize the fast spherical harmonic transform see [90, Section 3.1].

Appendix C

Initiate Scheme

Assume the acoustic wave equation satisfies

$$\begin{aligned}\frac{\partial^2 u}{\partial t^2} - c^2(\mathbf{x})\Delta u &= F, & (\mathbf{x}, t) \in \Omega \times (0, T], \\ u(\mathbf{x}, 0) &= \varphi_0(\mathbf{x}), & \mathbf{x} \in \Omega, \\ \frac{\partial u}{\partial t}(\mathbf{x}, 0) &= \varphi_1(\mathbf{x}), & \mathbf{x} \in \Omega.\end{aligned}$$

By Taylor series expansion

$$u^n = u^0 + n\tau \frac{\partial u^0}{\partial t} + \frac{(n\tau)^2}{2} \frac{\partial^2 u^0}{\partial t^2} + \frac{(n\tau)^3}{6} \frac{\partial^3 u^0}{\partial t^3} + \frac{(n\tau)^4}{24} \frac{\partial^4 u^0}{\partial t^4} + \frac{(n\tau)^5}{120} \frac{\partial^5 u^0}{\partial t^5} + \mathcal{O}((n\tau)^6), \quad (\text{C.1})$$

where the time derivatives

$$\begin{aligned}
u^0 &= \varphi_0, \\
\frac{\partial u^0}{\partial t} &= \varphi_1, \\
\frac{\partial^2 u^0}{\partial t^2} &= c^2 \Delta \varphi_0 + F^0, \\
\frac{\partial^3 u^0}{\partial t^3} &= c^2 \Delta \varphi_1 + \frac{\partial F^0}{\partial t}, \\
\frac{\partial^4 u^0}{\partial t^4} &= c^2 \Delta (c^2 \Delta \varphi_0 + F^0) + \frac{\partial^2 F^0}{\partial t^2}, \\
\frac{\partial^5 u^0}{\partial t^5} &= c^2 \Delta \left(c^2 \Delta \varphi_1 + \frac{\partial F^0}{\partial t} \right) + \frac{\partial^3 F^0}{\partial t^3}.
\end{aligned}$$

Similarly, if Ω is a ball, then Taylor series expansion of the normal derivative implies

$$\frac{\partial u^n}{\partial r} = \frac{\partial u^0}{\partial r} + n\tau \frac{\partial^2 u^0}{\partial t \partial r} + \frac{(n\tau)^2}{2} \frac{\partial^3 u^0}{\partial t^2 \partial r} + \frac{(n\tau)^3}{6} \frac{\partial^4 u^0}{\partial t^3 \partial r} + \frac{(n\tau)^4}{24} \frac{\partial^5 u^0}{\partial t^4 \partial r} + \mathcal{O}((n\tau)^5), \quad (\text{C.3})$$

where the time derivatives

$$\begin{aligned}
\frac{\partial u^0}{\partial r} &= \frac{\partial \varphi_0}{\partial r}, \\
\frac{\partial^2 u^0}{\partial t \partial r} &= \frac{\partial \varphi_1}{\partial r}, \\
\frac{\partial^3 u^0}{\partial t^2 \partial r} &= 2c \frac{\partial c}{\partial r} \Delta \varphi_0 + c^2 \Delta \frac{\partial \varphi_0}{\partial r} + \frac{\partial F^0}{\partial r}, \\
\frac{\partial^4 u^0}{\partial t^3 \partial r} &= 2c \frac{\partial c}{\partial r} \Delta \varphi_1 + c^2 \Delta \frac{\partial \varphi_1}{\partial r} + \frac{\partial^2 F^0}{\partial t \partial r}, \\
\frac{\partial^5 u^0}{\partial t^4 \partial r} &= c^2 \Delta \left(c^2 \Delta \frac{\partial \varphi_0}{\partial r} + \frac{\partial F^0}{\partial r} \right) + \frac{\partial^3 F^0}{\partial t^2 \partial r}.
\end{aligned}$$

Next suppose that $\tilde{\mathbf{x}} \in \gamma_{\text{out}}$ and $\mathbf{x} \in \gamma_{\text{proj}}$ is the orthogonal projection of $\tilde{\mathbf{x}}$ onto Γ . If $\varrho = |\tilde{\mathbf{x}} - \mathbf{x}|$, then the multivariable Taylor's Theorem

$$\begin{aligned}
u^n(\tilde{\mathbf{x}}) = & \left(\varphi_0 + \varrho \frac{\partial \varphi_0}{\partial r} + n\tau \partial \varphi_1 + \frac{\varrho^2}{2} \frac{\partial^2 \varphi_0}{\partial r^2} + \varrho(n\tau) \frac{\partial \varphi_1}{\partial r} + \frac{(n\tau)^2}{2} (c^2 \Delta \varphi_0 + F^0) \right. \\
& + \frac{\varrho^3}{6} \frac{\partial^3 \varphi_0}{\partial r^3} + \frac{\varrho^2(n\tau)}{2} \frac{\partial^2 \varphi_1}{\partial r^2} + \frac{\varrho(n\tau)^2}{2} \left[2c \frac{\partial c}{\partial r} \Delta \varphi_0 + c^2 \Delta \frac{\partial \varphi_0}{\partial r} + \frac{\partial F^0}{\partial r} \right] \\
& + \frac{(n\tau)^3}{6} \left[c^2 \Delta \varphi_1 + \frac{\partial F^0}{\partial t} \right] + \frac{\varrho^4}{24} \frac{\partial^4 \varphi_0}{\partial r^4} + \frac{\varrho^3(n\tau)}{6} \frac{\partial^3 \varphi_1}{\partial r^3} \\
& + \frac{\varrho^2(n\tau)^2}{4} \left[2 \left(c \frac{\partial^2 c}{\partial r^2} + \left(\frac{\partial c}{\partial r} \right)^2 \right) \Delta \varphi_0 + 4c \frac{\partial c}{\partial r} \Delta \frac{\partial \varphi_0}{\partial r} + c^2 \Delta \frac{\partial^2 c}{\partial r^2} + \frac{\partial^2 F^0}{\partial r^2} \right] \\
& + \frac{\varrho(n\tau)^3}{6} \left[2c \frac{\partial c}{\partial r} \Delta \varphi_1 + c^2 \Delta \frac{\partial \varphi_1}{\partial r} + \frac{\partial^2 F^0}{\partial t \partial r} \right] + \frac{(n\tau)^4}{24} \left[c^2 \Delta (c^2 \Delta \varphi_0 + F^0) + \frac{\partial^2 F^0}{\partial t^2} \right] \Big|_{\mathbf{x}} \\
& + \mathcal{O}(\varrho^5 + (n\tau)^5), \tag{C.5}
\end{aligned}$$

where the high order time derivatives are defined above.